MICROWAVE SUPERCONDUCTIVITY OF Nb_3Sn

A Thesis

Presented to the Faculty of the Graduate School

of Cornell University

in Partial Fulfillment for the Degree of

Doctor of Philosophy

by

James Bradley Stimmell

August 1978

MICROWAVE SUPERCONDUCTIVITY OF Nb_3Sn

James Bradley Stimmell, Ph.D.
Cornell University, 1978

Nb_3Sn superconducting resonant cavities have been fabricated using two different techniques: the first consisting of ionplating thin Sn layers onto Nb subtrates and then firing in vacuum at approximately 1000°C, and the second consisting of the vapor diffusion technique developed by Rinderer, Saur and Wurm [Z. Phys. 174, 105-422 (1963)].

Measurements of the superconducting surface resistance and breakdown field at 8.6 GHz are reported, and the structure and composition of the Nb_3Sn layers are analyzed using optical micrscopy of anodized specimens and Secondary-Ion-Mass-Spectroscopy (SIMS). Growth rates of vapor diffused samples are measured.

Results indicate that surfaces produced by vapor diffusion have superior r.f. properties, yielding surface resistances of 1 $\mu\Omega$ and breakdown fields of 380 gauss at 4.2°K. Results depend critically upon control of the Sn condensation rate, and the correspondence between condensation rate, microstructure and r.f. performance is discussed.

Biographical Sketch

Mr. Stimmell was born in Chambersburg, Pennsylvania, in February of 1950. He grew up in California and attended Stanford University, where he became involved with the Superconducting Linear Accelerator program. Upon completing his undergraduate education, he came to Cornell and again became associated with R.F. Superconductivity.

He presently lives in Fremont, California, with his wife Kathy and is employed by Ford Aerospace and Communications Corp., where he retains a personal and professional interest in applications of superconductivity.

This work is dedicated to Mason Yearian, who was convinced that I wasn't worthless, and Sidney Drell, who convinced me that I wasn't worthless.

Acknowledgements

The author wishes to acknowledge the contributions of the scientific and technical staff of the Laboratory of Nuclear Studies and, in particular, those of the CRF group.

The author also wishes to express his gratitude to his wife, Kathleen, and to his fellow students and friends: to Andy, Brent, Chris, David, Elizabeth, John, Junko, Marilyn, Michael, Nathan, Pia, Ray, Roger, Serge, Tom, and Velma for their comradeship and solidarity, which made the difficult realities of a graduate student's existence much easier to face.

Table of Contents

Table of Contents (continued)

List of Tables

List of Figures

List of Figures (continued)

List of Figures (continued)

List of Figures (continued)

List of Bibliographies

I. SUMMARY

In order to develop a workable method for fabricating Nb_3Sn accelerating structures, single cell accelerating cavities with Nb_3Sn interior surfaces have been prepared, using two distinct methods.

With the first method, Nb cavities were plated with 8-10 μm of Sn and then heated to 1000°-1050°C. With the second method, Nb cavities were exposed to Sn vapor at 1000°-1050°C.

In addition, a hybrid technique was tried, in which a Nb cavity was plated with a thin (0.8 μm) layer of Sn and then exposed to Sn vapor in the same manner as the cavities prepared by the second method.

R.F. measurements, optical photomicrographs and concentration-vs.-depth profile measurements (obtained using Secondary-Ion-Mass-Spectroscopy) were made for both types of surfaces. Growth-rate measurements of the surfaces produced by the second method were also obtained.

Results indicate that cavities produced by reaction from unsaturated Sn vapor have the higher quality factors (Q), higher maximum accelerating fields, and show less Q-degradation at high field levels.

Surfaces reacted from unsaturated Sn vapor also show smoother surface textures and have SIMS profiles which suggest the existence of a homogeneous Nb_3Sn phase over a depth of

several microns, whereas plated-and-fired surfaces have rough crystalline textures and SIMS profiles showing no region of uniform composition.

II. INTRODUCTION: MOTIVATION FOR THE STUDY OF R.F. SUPERCONDUCTIVITY FOR ACCELERATOR APPLICATIONS

The construction of particle accelerators of ever increasing energy has necessitated the development of r.f. accelerating systems capable of producing large accelerating fields at frequencies in the gigahertz range.

The desirability of high field capability is obvious in the case of a linear accelerator, since an accelerator of given energy must have a length inversely proportional to the accelerating field. High accelerating fields are also necessary in synchrotrons, for more subtle reasons. Stability of the longitudinal oscillations of particle bunches requires that the r.f. system be capable of supplying an energy gain per turn substantially in excess of the average radiative losses. In addition, the design of the strong-focusing magnetic lattice is considerably more complicated if long field-free regions are required for r.f. structure.

With conventional r.f. structures, considerable power is required to obtain even moderately high fields. This power is necessary to offset ohmic losses in the walls of the accelerating structure, and is related to the accelerating field through the shunt impedance R_{sh} of the accelerating structure:

$$P_{diss} = E_{acc}^2 / R_{sh} \ (W/m) \qquad (1)$$

where

P_{diss} = power/unit length dissipated in the structure,

E_{acc} = effective accelerating field (V/m), and

R_{sh} = shunt impedance per unit length (ohms/m).

If a particle beam of current I_b is also present, with phase α relative to the accelerating field, the total power is

$$P_{tot} = E_{acc}^2/R_{sh} + E_{acc} I_b \cos\alpha \quad \text{(Watts/m)} \qquad (2)$$

The shunt impedance is thus a principal figure of merit for an accelerating structure. Its value depends upon the geometry of the structure and is inversely proportional to the surface resistance of the interior walls. For normal conductors at frequencies below the anomalous region, the surface resistance is given by:

$$R_s = (\pi u_o f \rho)^{1/2}$$

where ρ is the bulk resistivity and f is the operating frequency. For copper cavities at room temperature, one obtains surface resistances of 8×10^{-3} ohms, 1.4×10^{-2} ohms and 2.4×10^{-2} ohms at 1, 2.8 and 8.4 GHz, respectively.

As an example, the SLAC structure, fabricated from copper and operating at 2.8 GHz, has a shunt impedance of 55 megohm/m.[1] To sustain a field of 10 MV/m in this structure would require a power input of 1.8 MW/m, or a total power input of about 5500 MW for the entire 10,000 ft. structure. At these power levels continuous operation is impossible, since even if such a CW power source were available, the heat generated by ohmic dissipation would limit the

structure to pulsed operation.

The situation cannot be substantially improved by clever structure geometry, especially if ease of fabrication is important. A very substantial improvement may be obtained, however, if the structure is made superconducting. Niobium structures have achieved surface resistances as low as 10^{-9} ohms. Assuming that the SLAC structure could be fabricated from such material, the total power requirement (excluding beam loading) for a 10 MV/m field would be reduced to below 5.5 kW. In addition to reducing enormously the capital cost and operating expense of the r.f. power source, such a structure would be capable of continuous, rather than pulsed, operation, thus allowing multiple coincidence experiments of a type not presently feasible at facilities such as SLAC.

Desirable Properties for R.F. Superconductors

For superconducting structures the shunt impedance and accelerating field are limited by the surface resistance R_s and breakdown field H_c^{ac}, respectively, of the superconductor. We consider here the properties a superconductor should have to allow low R_s and high H_c^{ac}.

Surface Resistance

The surface resistance of a superconductor is defined by the relation

$$P_d = 1/2\ H^2/R_s \qquad (4)$$

where P_d = power dissipated/unit area (W/cm^2),

H = tangential surface r.f. magnetic field, and

R_s = surface resistance (ohms "per square").

Qualitatively, R_s is non-zero because not all of the electrons in the superconductor are in the superconducting state at non-zero temperatures. The a.c. magnetic fields inside the superconductor induce a.c. electric fields, and in the presence of these fields the normal state electrons dissipate energy as in normal conductors.

Experimentally, R_s is found to have the form

$$R_s = (R_o hf^2/kT)\exp(-T_c/T) + R_{res} \qquad (5)$$

as shown in Figure 1.

The first term represents the BCS surface resistance and is understood on theoretical grounds. The frequency and temperature dependence follow from the BCS theory and indicate that materials with a high transition temperature are to be preferred. The constant R_o depends in a complicated way upon the material parameters. This arises in part from the distribution of shielding currents within the superconductor and in part from the manner in which energy is absorbed by the normal state electrons. Halbritter[2] has calculated the dependence of R_o upon mean free path l_o and superconducting coherence length ξ_f and claims that R_o can have a minimum for $l_o \sim \xi_f$, and increases for longer l_o. This suggests that tailoring of l_o might yield low R_o. Past

work with Nb[2] and Nb_3Sn[3], however, indicates that for these materials $l_o < \xi_f$ already, and this is likely to be the case for high T_c compounds in general.[4] One should therefore seek to maximize l_o by minimizing the concentration of impurities, lattice defects and compositional inhomogeneities.

The residual resistance R_{res} is not completely understood. It has been suggested, however, that a low density of grain boundaries might contribute to low R_{res}.[5] Theories of the residual resistance have also been proposed involving generation of surface phonons[6,7] and energy exchange to localized oxide states.[8] Experimental results from several laboratories show "best values" of R_{res} for Nb which are independent of frequency and fall in the range from $1\text{-}3\times10^{-9}$ ohms.[12] At low temperatures, R_s is therefore dominated by the residual resistance.

To achieve low surface resistances, then, one desires a superconductor with high T_c and relatively long mean free path to minimize the BCS resistance, and a low grain boundary density to minimize the residual resistance.

Breakdown Field

Although the very high shunt impedances obtainable with superconducting structures remove r.f. power limitations as an obstacle to obtaining high fields, a given superconducting structure will still have a limiting breakdown field,

operation above which will cause the structure to revert to the normal-conducting state.

Any discussion of the breakdown field must carefully distinguish between the intrinsic limits imposed by the superconducting material and other limits imposed by thermal or electronic phenomena involving the structure as a whole.

In particular, the existence of regenerative multipactor often limits low frequency structures to fields much lower than those obtainable with smaller, higher frequency structures. This has been demonstrated at Cornell University, where work with 2.8 GHz and 8.6 GHz Nb structures of essentially identical geometry has produced much higher fields at the higher frequency.[9]

Assuming that the structure is "perfectly" designed, the magnetic breakdown field of the superconductor then sets a limit on the accelerating field. The accelerating field is proportional to the peak surface magnetic field occurring in the structure, and if this surface field exceeds a critical value H_c^{ac}, it becomes energetically favorable for a macroscopic region of the surface to revert to the normal state. The higher a.c. losses of this normal region then cause a thermal runaway, which drives the surrounding material into the normal state.

The following table summarizes the best values of H_c^{ac} achieved at other laboratories, and it may be seen that the

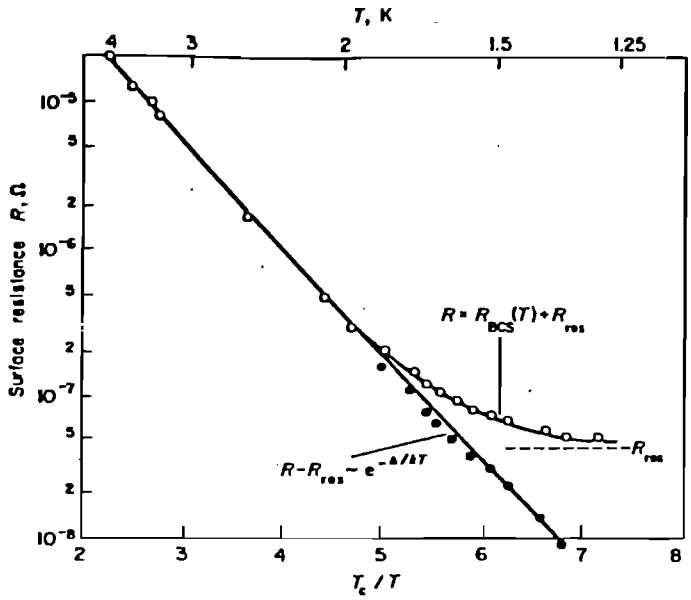

Figure II-1. Surface resistance of niobium at 9.5 GHz as a function of the temperature (from ref. 12)

Frequency band	Frequency, GHz	Mode	Surface treatment	B_c^{ac}, mT	$Q_0(B_c^{ac})$	Institute
X	9.5	TE_{011}	EP-anod	159	1×10^{10}	FL-Siemens
X	9.5	TM_{010}	EP-anod	149	3×10^{9}	FL-Siemens
X	8.6	TM_{010}	CP-deg	108	8×10^{9}	HEPL, Stanford
X	10.5	TE_{011}	CP-deg	96	1×10^{10}	SLAC, Stanford
S	3.7	TE_{011}	EP-deg	81	1×10^{11}	IEKP, Karlsruhe
S	2.8	TM_{010}	EP-anod-deg	65	1×10^{9}	HEPL, Stanford
S	2.8	HEM_{11}	anod-deg	85	2×10^{9}	IEKP, Karlsruhe
L	1.3	TM_{010}	CP-anod-deg	35	1×10^{9}	HEPL, Stanford
	0.09	Helix	EP-anod	120	2×10^{8}	IEKP, Karlsruhe
	0.09	Helix	deg-EP-anod	120	1×10^{8}	Argonne Nat Lab

EP — electro-polished, anod — anodically oxidized, CP — chemically polished, deg — degassed in uhv

Figure II-2. Critical rf flux densities B_c^{ac} and Q_0 values at B_c^{ac} of niobium cavities (from ref. 12)

highest fields have been obtained at the higher X-band frequencies.

It is customary to speak of three distinct "critical fields" for type II superconductors such as Nb and Nb_3Sn. At applied fields below the "first critical field" H_{c1}, magnetic flux is excluded completely from the interior of the superconductor, which is said to be in the "Meissner state". Between H_{c1} and the "upper critical field" H_{c2}, magnetic flux lines penetrate the superconductor, forming a fluxoid lattice. The density of fluxoids increases until, at H_{c2}, the entire superconductor, with the possible exception of a thin surface layer, reverts to the normal state. The "thermodynamic critical field" H_c is then defined as the field level at which the diamagnetic energy $H^2/8\pi$ necessary to completely exclude a field H from the interior of the superconductor is equal to the free energy difference between the normal and superconducting states. For type I superconductors, $H_c = H_{c1}$, while for both type I and type II superconductors, $H_c^2/8\pi$ is equal to the "area" $\int \vec{M} \cdot d\vec{H}$ under the magnetization curve of $\vec{M}$ vs. $\vec{H}$. H_c is a useful measure of the "strength" of a superconductor, and H_c^2 is proportional to the superconducting energy gap.

Although it is clear that r.f. superconductors operate in the Meissner state, it has been shown that H_c^{ac} may exceed H_{c1}.[10] It seems likely that a situation analogous to

superheating exists, in which the time necessary for a fluxoid to nucleate and penetrate to the interior of a superconductor is greater than that fraction of the r.f. cycle during which the r.f. field exceeds H_{c1}. Moreover the existence of a surface barrier, inhibiting fluxoid entry even at low frequencies, has been shown both theoretically and experimentally for hard superconductors such as Nb_3Sn.[11] If the surface of the superconductor is smooth and uniform, thus providing no nucleation sites for fluxoid entry, the external field must be raised to a "superheating field" $H_s \sim H_c$ to overcome this barrier. If H_c^{ac} is in fact related to this "superheating field", then a large thermodynamic critical field is desired for accelerator applications.

It should be emphasized that superheating fields approaching H_c cannot be expected unless a defect-free surface is obtained. Rough surfaces or voids, by producing nucleation sites for fluxoid formation, enable flux entry at field levels well below H_c, or even below H_{c1} if the roughness is sufficient to cause geometric enhancement of the magnetic field. In addition, a high degree of compositional uniformity is necessary to prevent "weak spots" with locally depressed energy gap, and thus low H_c.

To enable high breakdown fields, then, one desires a superconductor with a large thermodynamic critical field

H_c, and which can be produced with a smooth, uniform surface. A secondary consideration is that the thermal conductivity be sufficient to carry away the superconducting losses without raising the surface temperature excessively. This requirement is less stringent if the material can be deposited as a thin film upon a substrate having good thermal conductivity.

Refrigeration Efficiency

A final consideration regarding transition temperature involves the thermodynamic efficiency of the accelerator refrigeration system, since the r.f. losses are dissipated at low temperatures. The efficiency of an ideal refrigerator decreases linearly with operating temperature, and the efficiency of a practical refrigerator may be expected to decrease much more rapidly as operating temperature decreases. Nb accelerator structures presently under construction operate at 1.5°-1.8°K, imposing stringent demands upon the refrigerator design. Assuming operation of a Nb_3Sn structure at the same reduced temperature T/T_c raises the operating temperature to 3-3.6°K, and it is likely that such a structure could be operated in boiling helium (4.2°), simplifying refrigeration problems considerably and providing higher overall efficiency.

Conclusions

A superconductor, to be suitable for accelerator applications, should have a high transition temperature T_c

to reduce BCS surface resistance and to provide higher refrigeration efficiency, and a high thermodynamic critical field H_c to enable large accelerating fields. These two demands are fortunately not incompatible, since both T_c and H_c are related to the superconducting energy gap $\Delta(0)$, and high T_c materials usually have high H_c values as well.

In addition, the superconductor must be capable of being fabricated as a thin film with good uniformity and smooth surface finish on a substrate having good thermal conductivity.

Properties of A-15 Compounds

The highest transition temperatures observed to date are those of the A15 compounds. This family includes V_3Ga (15.5°), V_3Si (17.1°), Nb_3Sn (18.3°), Nb_3Al (18.9°), Nb_3Ga (20.3°), and Nb_3Ge (23°) as well as ternary compounds such as $Nb_3(Al_{0.2}Ge_{0.8})$ (20.3°).

All of these compounds are of the form A_3B and have the A15 crystal structure shown in Figure 3. The B atoms occupy the corners and center of a body-centered-cubic structure. The A atoms form orthogonal chains which bisect the faces of the BCC unit cells. The spacing of the A atoms in these chains is less than in the pure A crystal.[4]

Atomic size is the principal factor in determining whether two otherwise suitable elements will form an A15 structure; in particular the ratio of atomic radii r_A/r_B must be between 0.84 and 1.12.[4] As a result, the A and B

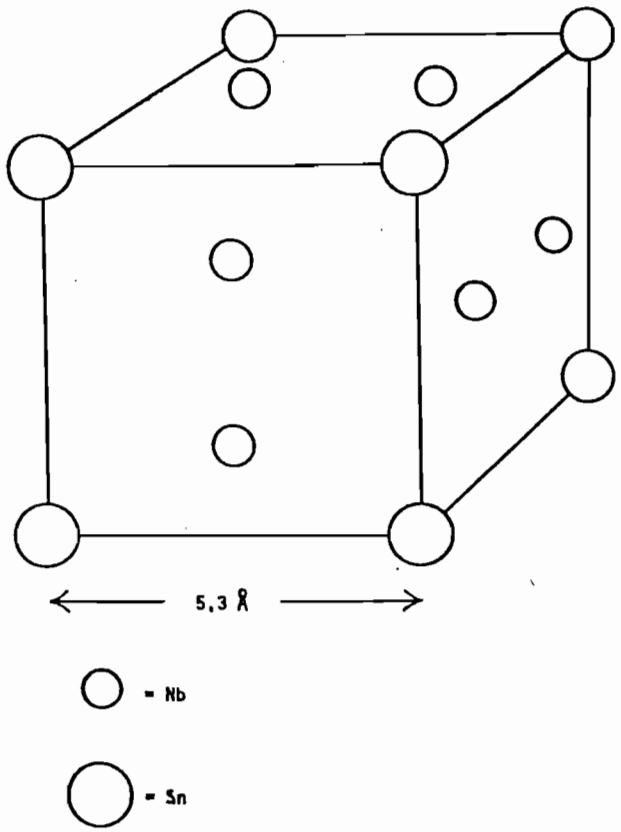

Figure II-3. A-15 crystal structure

atoms are to a certain extent interchangeable; A atoms may sit on B sites and vice versa, the tendency towards such disorder increasing with temperature.

Despite the exact stoichiometry suggested by the A_3B formula, all A15 compounds exist over a range of stoichiometry. Some compounds, in fact, do not exist as homogeneous A15 phases at the 3:1 ratio but are two-phase mixtures at this composition. The existence of a range of stoichiometry for the A15 phase is of great importance for the fabrication of homogeneous A15 layers since, in the absence of such a range, local deviations from exact stoichiometry would form "islands" of some different phase.

Structural Factors Influencing T_c

The structural factors most likely to influence the superconducting properties of a given A15 compound are the degree of long-range order and the stoichiometry.

Long-Range Order

As mentioned earlier, the locations of A and B atoms are to a certain extent interchangeable, due in part to their nearly equal atomic radii. Although the lowest energy configuration is that in which all atoms occupy correct sites, at high temperatures the increased entropy of the less ordered states resulting from interchange of A and B atoms offsets this, and the equilibrium configuration may be disordered. The degree of order in a solid may be measured

using diffraction techniques, and correlations between long range order and T_c have been observed for a number of A15 compounds.[4]

Stoichiometry

We consider two mechanisms by which T_c might vary with stoichiometry. First, since perfect long range order is possible only at exact 3:1 stoichiometry, deviations from ideal composition can lower T_c through the mechanism just discussed.

The second mechanism likely to link stoichiometry with T_c is the valence electron to atom ratio e/a. According to the Matthias rules[13], T_c depends strongly upon e/a, with sharp peaks at e/a = 4.75 or 6. Since stoichiometric variations affect e/a, they would be expected to influence T_c. Oxygen inclusions or other impurities, by removing electrons from the conduction band, might have a similar effect.

The majority of A15 compounds show a T_c which peaks at 3:1 stoichiometry and long range order parameter S = 1, corresponding to a highly ordered, stoichiometric state.[14,15]

Stability of A15 Phases

An additional consideration of importance to r.f. applications of A15 superconductors is the thermodynamic stability of the A15 phase. If homogeneous A15 layers are required for good r.f. performance, then the A15 phase must be sufficiently stable to prevent the precipitation of other

phases.

Since most of the existing experimental work on A15 compounds has been motivated by their potential for d.c. applications, interest has focused on maximizing the d.c. critical current density J_c and the upper critical field H_{c2}. Neither is particularly devastated by inhomogeneity, and J_c may in many cases be increased if the density of pinning sites is increased, either by precipitation of non-A15 phases, radiation induced disorder, or cold work.

It is therefore quite possible that materials with properties very desirable for d.c. applications may be entirely unsuited to r.f. applications.

The most likely obstacle to formation of homogeneous A15 layers is the precipitation of B-rich phases near the desired 3:1 stoichiometry.[4] As mentioned earlier, many A15 compounds do not exist as homogeneous A15 phases at 3:1 stoichiometry, but are mixtures of the A15 phase and some other phase. Others, although they have a homogeneity boundary in their phase diagram allowing 3:1 homogeneity at high temperatures, will precipitate B-rich phases upon cooling.

In either of these cases, attainment of a homogeneous A15 phase at low temperatures requires the "freezing in" of a non-equilibrium state. Compounds which do not exhibit homogeneity at 3:1 stoichiometry may be produced by

non-equilibrium processes such as co-sputtering, and considerable success has been realized with Nb_3Ge using this method. Compounds which are homogeneous only at high temperatures must be cooled quickly enough to prevent precipitation of unwanted phases.

Preparation Methods for A15 Compounds

We suggested earlier that a homogeneous superconductor with a high transition temperature is desirable for good r.f. performance. We now consider how such a material might be produced and formed into a useable structure.

Present Nb accelerating structures are formed either by machining from bulk material or by stamping or drawing sheet material. In most cases electron beam (EB) welding is used to join pieces together, and the interior is then electropolished to produce surfaces free of stresses, plastic deformation, and surface imperfections.

It is unlikely that A15 compounds can be used in this manner, principally because of the brittleness exhibited by the A15 structure. In addition, the relatively poor thermal conductivities of A15 compounds would limit the high field capabilities of the resulting structures, even if they could be fabricated. These two factors suggest that the A15 material should be produced as a thin layer on the interior of an already formed structure. Such a layer need be only microns thick, since the r.f. fields extend but a few penetration depths into the superconductor.

Methods Presently Used to Prepare A15 Compounds

A15 compounds have already been prepared using a number of techniques. These include heat treatment of compacted powders, sputtering, chemical vapor deposition, and diffusion reactions. We discuss these methods very briefly, and consider their suitability for accelerator structures.

Sintered Powders

A considerable amount of work has been done on Nb_3Sn prepared by sintering powders. With this technique, the constituents are finely powdered, sieved, mixed thoroughly and compressed. During heat treatment, the constituents interdiffuse and react. This method has great merit for material studies since the constituent proportions and reaction temperature can be varied independently.

The technique has three possible disadvantages, however. It yields a microstructure with a high density of fissures and voids[16], and the large surface area of the powdered constituents results in a large oxygen content.[17] It would also be very difficult to coat the interior of a preformed structure using this method.

Sputtering

Considerable success has been achieved with sputtering techniques, particularly in the case of difficult compounds such as Nb_3Ge. Typically, two constituents are sputtered simultaneously onto a temperature-controlled substrate.

The stoichiometry at each point depends upon the relative distances to the two sputtering targets and therefore varies considerably across the substrate. This continuous variation of stoichiometry is exploited in materials studies, since at least one part of the substrate must have correct stoichiometry. It might, however, be difficult to cover an entire accelerating structure with a homogeneous, stoichiometric layer, particularly if the allowed stoichiometric range for A15 phase formation is small. In addition, it would be difficult to coat the inside of a one-piece structure, since a plasma discharge must then be maintained inside an essentially closed metallic structure.

An alternative to co-sputtering as described above is sputtering from a single target of the correct stoichiometry, which could be fabricated using the sintered powder technique. This requires, of course, that both the sintering and the sputtering techniques be mastered.

Offsetting the disadvantages of sputtering is the fact that stoichiometry, substrate temperature, deposition rate and deposition thickness may be independently varied.

Chemical Vapor Deposition (CVD)

Chemical vapor deposition has been used to prepare a number of A15 compounds, and many other materials as well. In CVD processes, gaseous compounds containing the desired constituents are passed over a substrate, usually at elevated

temperature. Chemical reduction of these compounds results in deposition of the desired elements onto the substrate, with stoichiometry controlled for the most part by the relative partial pressures of the gases.

As an example, the process developed by RCA Corporation[18] for production of Nb_3Sn superconducting tapes uses the reaction

$$3NbCl_4 + SnCl_2 \rightarrow Nb_3Sn + 14HCl$$

to deposit Nb_3Sn onto metal tapes at a temperature of about 1000°C. The Nb and Sn chlorides are produced by flowing Cl_2 over hot Nb and Sn in separate chlorination chambers, and the stoichiometry is controlled by regulating the flow of Cl_2 through these chambers.

This process, and another CVD process developed by Westinghouse Laboratories for Nb_3Ge[19] are possible candidates for production of superconducting r.f. structures. Three possible difficulties suggest themselves:

1) Since deposition rate and the structure of the deposit depend upon temperature and reagent concentrations, a very uniform temperature distribution and flow of reagent gases must be insured over the entire substrate surface. This might be difficult with complex substrate geometries.

2) The reaction byproducts (H_2, Cl_2 and HCl in the Nb_3Sn process described) might be incorporated as impurities in

the A15 layer.

3) Some evidence exists to indicate considerable lattice disorder in vapor-deposited A15 layers.[20]

In addition, the equipment required for CVD is somewhat elaborate and the byproducts are toxic and corrosive.

Diffusion Reactions

The diffusion reactions we will consider are those in which a substrate of constituent A (most often Nb) is immersed in either the liquid or gas phase of the second constituent B (Sn, Al, Ge, ...). Constituent B diffuses into the substrate and reacts, forming the desired A_3B phase. The reaction occurs at the A-A_3B interface, beneath the growing A_3B layer.

Since the process need not depend upon a plasma discharge, interior surfaces may be coated uniformly. In addition, the process is simpler and the equipment less sophisticated than is the case with sputtering.

Offsetting these advantages is the fact that deposition rate, substrate temperature, and deposit thickness are interrelated in a complicated way through the strong temperature dependence of the diffusion coefficients and vapor pressure.

In addition, the stoichiometry varies with depth, since diffusion of the B element can proceed only along a concentration gradient. The success of the diffusion reaction

method is therefore likely to depend in detail upon the properties of the constituents chosen and upon the phase diagram of the resulting intermetallic system.

Choice of Method

Because of the microstructure problems of the sintered powder technique and the contamination, coverage and long range order considerations of CVD, the most attractive methods are sputtering and diffusing reaction.

The diffusion reaction technique has two principal advantages over sputtering: it is simpler and cheaper to implement, and it lends itself naturally to coating the interior of an accelerator structure. With the sputtering technique, complete coverage would almost certainly require that the structure be split longitudinally and coated in half-sections. If the properties of the A15 compound chosen are suitable, then, diffusion reaction should be an easier process. Otherwise, the greater control of deposition parameters afforded by the sputtering process might be necessary.

Choice of an A15 Compound

Our choice of diffusion reaction as a production method requires that an A15 compound with equilibrium properties suitable to this method be chosen. Of the six binary compounds listed earlier, the last two (Nb_3Ga, Nb_3Ge) do not exist as stable bulk materials at 3:1

stoichiometry, while stoichiometric Nb_3Al exists only at temperatures high enough to cause excessive atomic disorder.[4] Production of these three materials at correct stoichiometry depends upon non-equilibrium processes, such as sputtering, where the desired concentration can be dictated.

Since diffusion reactions provide no such means of dictating composition, a compound must be chosen which is stable as a "bulk" material (at least several μm thick) at 3:1 stoichiometry. Of the three candidates remaining (V_3Ga, V_3Si, Nb_3Sn), Nb_3Sn has the highest transition temperature. This, combined with the considerable experience already established with Nb structures, makes it the most attractive candidate for superconducting accelerator structures. Figure 4 below shows the equilibrium phase diagram of Nb_3Sn, as given in ref. 17.

Five phases exist in the Nb-Sn system: Nb, Nb_3Sn, Nb_6Sn_5, $NbSn_2$ and Sn. It can be seen from the phase diagram that Nb_3Sn exists as a homogeneous single phase between composition limits of approximately 18 and 28 atomic percent Sn, and that this single-phase region extends down to room temperature. The Sn-rich phases Nb_6Sn_5 and $NbSn_2$ form at higher Sn concentrations and have rather complicated crystal structures. Neither phase is stable above 950°C, however, so that their formation can be prevented by choosing higher

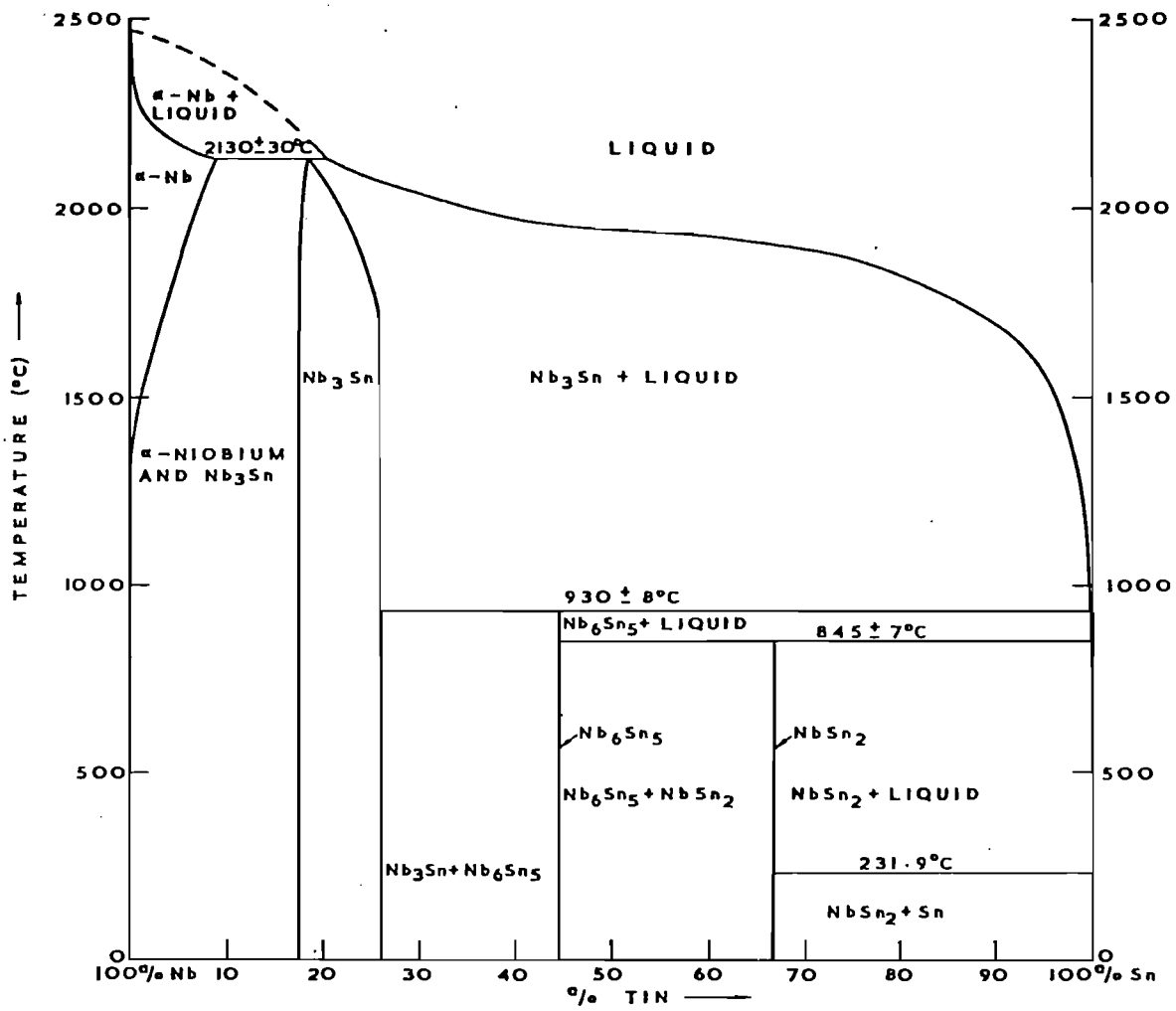

Figure II-4. Equilibrium phase diagram of the Nb-Sn system

reaction temperatures. This fact, plus the rather generous stoichiometric range for the A15 phase Nb_3Sn, suggest that Nb_3Sn is a good choice for diffusion reaction.

Methodology

Having decided upon Nb_3Sn as an attractive material for accelerating structures, an experimental program was undertaken to fabricate Nb_3Sn structures using two different diffusion reaction techniques.

The first technique chosen differs considerably from the technique previously reported by Kneisel[3] and by Martens et al.[21] in which Nb surfaces were exposed to Sn vapor. Instead, the Nb substrate material was plated with a 7-10 μm thick layer of Sn, and the Nb-Sn composite was then reacted at a temperature of about 1000°C. Four r.f. cavities and numerous strip-samples were produced using this technique.

As a control, and also to provide more information about the Nb_3Sn formation process, a second group of cavities and strip-samples was produced, duplicating closely the technique of Martens et al., which had been shown to produce excellent results.

In addition, one cavity and two strip-samples were produced using a third, hybrid technique in which Nb substrates were plated with 0.8 μm of Sn and exposed to Sn vapor.

Detailed microwave measurements were made of all three

cavity types, including determination of surface resistance, energy gap Δ, maximum accelerating field, and change in superconducting penetration depth $\Delta\lambda(T)$. The differences in r.f. performance were then correlated with other physical measurements made on the cavity surfaces or on similarly prepared strip-samples. These measurements included optical microscopy, Secondary-Ion-Mass Spectroscopy (SIMS) concentration profiles, and growth-rate measurements.

References for Chapter II

1. The Stanford Two-Mile Accelerator, R. B. Neal, ed. (W. A. Benjamin, Inc., New York, 1968).

2. Halbritter, J., Z. Physik 266, 209-217 (1974).

3. Kneisel, P., Stoltz, O., and Halbritter, J., "Nb_3Sn for Superconducting RF Cavities", International Cryogenic Materials Conference, Queens University, Kingston, Ontario, Canada (1975).

4. Dew-Hughes, D., "Superconducting A15 Compounds", Brookhaven National Laboratory, April 1975.

5. Halbritter, J., personal communication, August 1975.

6. Halbritter, J., J. Appl. Phys. 42, 82 (1971).

7. Passow, C., Phys. Rev. Lett. 28, 427 (1972).

8. Halbritter, J., Phys. Lett. 49A, 379 (1974).

9. Banner, M., and Padamsee, H. Unpublished results, Laboratory of Nuclear Studies, Cornell Univ., Ithaca, N.Y. (1975-76).

10. Schnitzke, K., Martens, H., Hillenbrand, B., Diepers, H., Phys. Lett. 45A, 393 (1973).

11. Bussiere, J. F., "Evidence for the Surface Barrier in a Hi-K Superconductor", Brookhaven National Laboratory, 1975.

12. Pfister, H., "Superconducting Cavities", Cryogenics (Jan. 1976).

13. Matthias, B. T., Prog. Low Temp. Phys., C. J. Gorter, ed. (North-Holland, Amsterdam, 1957), Vol. II, p. 138.

14. Blaugher, R. D., Hein, R. A., Cox, J. E., and Waterstrat, R. M., J. Low Temp. Phys. 1, 531 (1969).

15. Van Vucht, J. H. N., Bruning, H.A.C.M., Donkersloot, H. C., and Gomes de Mesquita, A. H., Phillips Res. Reports 19 (1964).

16. Enstrom, R., Courtney, T., Pearsall, G., and Wulff, J., Current and Field Dependence of Superconductivity on Microstructure in the Niobium-Tin System", Metallurgy of Advanced Electronic Materials, G. E. Brock, ed. Wiley, New York, 1963).

17. Charlesworth, J. P., Macphail, I., and Madsen, P. E., J. Materials Sciences 5, 580-603 (1970).

18. Hanak, J. J., Strater, K., and Culler, G. W., "Preparation and Properties of Vapor-Deposited Niobium Stannide", RCA Review, Sept. 1964.

19. Roland, G. W., and Braginski, A. I., "Chemical Vapor Deposition of Nb_3Ge", Intnl. Cryogen. Matl. Conf., Kingston, Ontario (1975).

20. Intermetallic Compounds (John Wiley & Sons, New York, 1969).

21. Hillenbrand, B., Martens, H., Pfister, H., Schnitzke, K. and Uzel, Y., "Superconducting Nb_3Sn Cavities with High Microwave Qualities", 1976 Applied Superconductivity Conference, Stanford Univ., August 1976.

III. EXPERIMENTAL PROCEDURES

1. Preparation of Nb_3Sn Coatings

A. Plated Cavities and Strip-Samples

"Ionplated" cavities and strip-samples were produced by plating Sn onto Nb substrates and then heating in vacuum to form a Nb_3Sn layer.

The plating process chosen, known as ion plating, is a vacuum metalization technique originally developed by D. Mattox[1] of Sandia Laboratories and subsequently refined by others.[2,3] The process is reputed to provide excellent adhesion and good coverage of complex geometries, including the ability to plate the interiors of cavities and waveguide assemblies. The substrate to be plated is placed in an Argon atmosphere at approximately 50 μm pressure, and is maintained at a negative potential. The resulting plasma discharge sputter-cleans the substrate surface. The material to be plated is then evaporated into the discharge and is deposited as the substrate is continuously sputter-cleaned.

It was originally thought that most of the plated material was deposited as ions, with considerable impact energy, thus promoting good adhesion. A large degree of ionization of the plated material was also thought to be responsible for the throwing power (ability to "plate around corners") of this process, which is considerably greater than that of regular evaporation. Subsequent studies[4], however, have

indicated that a very small percentage of the plated material is ionized. The improved adhesion might then be due to the continuous sputter-cleaning of the substrate during deposition, while the short mean free path in the Argon atmosphere improves throwing power. It has also been suggested[5] that high surface mobility, resulting from the Argon bombardment, enhances formation of continuous layers and influences the structure of ion plated materials.

Motivation for Ion Plating

It has been shown[6] that Nb surfaces form a tenacious oxide after even very brief exposure to air. It seemed possible that this oxide might inhibit the growth of a uniform Nb_3Sn layer, and might result in an impure surface region with poor r.f. properties. By using a process such as ion plating, a Nb-Sn interface may be obtained which is free of oxygen contamination.

Ion plating also has the ability to produce relatively thick (10 μm) coatings. Such thicknesses are difficult to achieve by sputtering.

All of the ion plating was performed by Millis Research of Millis, Mass. Both resistive and electron-beam evaporation of Sn were tried, with electron-beam evaporation producing shinier and more adherent layers.

Reaction Procedure

Plated samples were reacted in one of two high-vacuum

tube furnaces, constructed as described in Figure 1 and Appendix A. The hot regions of both furnaces were constructed of Nb to avoid contamination of the samples. This was important because samples were not sealed in ampullas but were pumped continuously during firings. Pressure, measured with an ionization gauge at the cold end of the furnace, was a few $x10^{-6}$ mm during firing and 2-4 $x10^{-8}$ mm after firing.

Two heating rates were tried. "Slow-fired" samples were inserted into a cold furnace and brought to reaction temperature in 40-60 minutes. "Fast-fired" samples were inserted into a preheated furnace and reached reaction temperature in 2-5 minutes.

Reaction temperatures of 950°C, 1000°C, 1050°C, and 1150°C, measured with a thermocouple inside the sample holder, were used, the latter two temperatures representing the operating limits of the large and small furnaces, respectively.

Reaction times were adjusted to achieve complete removal, by simultaneous reaction and evaporation, of unreacted Sn from the substrate surfaces, and ranged from 30 to 600 minutes. Timing was begun when the sample temperature rose to within 25°C of the chosen reaction temperature, and ended when the samples were withdrawn from the furnace.

Samples cooled by evaporation and typically reached 550°C within 5 minutes, and 300°C within 20 minutes.

An unanticipated problem encountered during production of plated-and-fired samples was the agglomeration of the Sn into droplets during the early stages of the firing cycle. Two techniques were tried to prevent this agglomeration. The first involved roughening the sample surfaces by abrading them with assorted sizes of abrasive grit. This technique was unsuccessful. The second technique, which was successful, consisted of sputtering a thin (approx. 0.1 μm) layer of Nb over the plated Sn, and then firing as usual. These Nb overlayers were applied by John Warlaumont of the Cornell Materials Science Center, and by Bud Addis of the Cornell Department of Materials Science. In both cases, special high purity sputtering equipment and techniques, developed for fabrication of thin-film superconducting devices, were employed.

B. Vapor Diffused Cavities and Strip-Samples

Vapor diffused surfaces were produced by slightly modifying the larger furnace to include a source of Sn vapor as shown in Figure 2. A round stamped Nb cup was fitted to the movable "sled" sample holder, forming an approx. 10 mm deep depression into which Sn shot was placed. A .005" Nb foil cover was fitted to the cup to prevent spillage of the shot, and a carefully chosen number of small holes were drilled in the foil cover to permit controlled access of Sn vapor to the substrate.

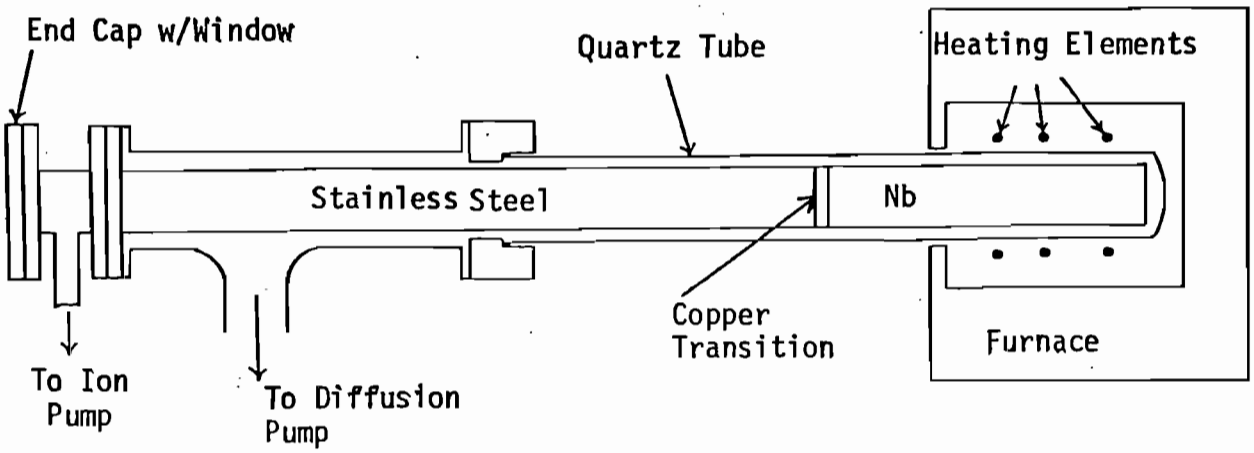

Figure III-1. Furnace Construction

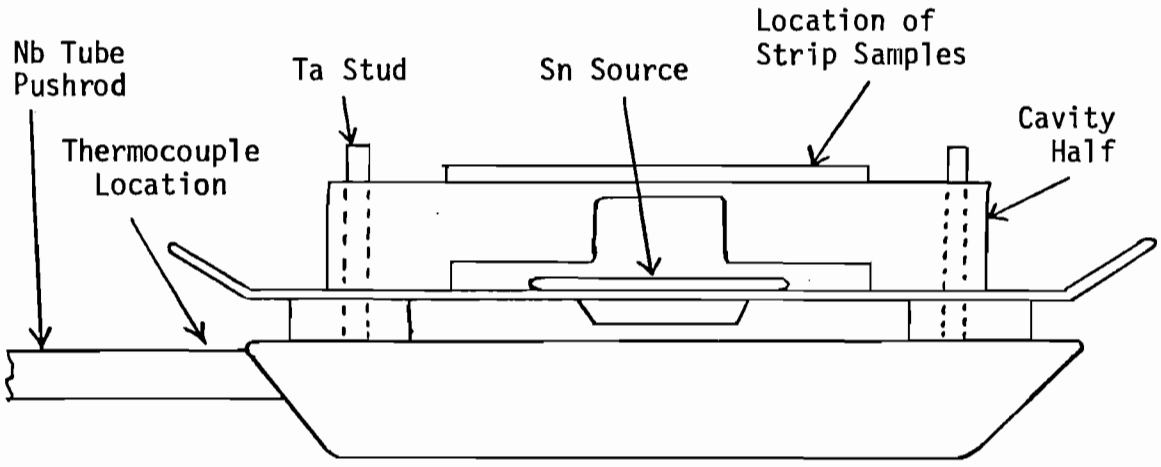

Figure III-2. Details of "sled" sample holder

The characteristics of vapor-diffused surfaces were found to depend critically upon the relative positions of substrate and source, and upon the amount of Sn vapor released from the source. Cavity halves were placed face down over the Sn source and held fixed with tantalum pegs. The cavity half thus served to contain the Sn vapor, and the amount of vapor released from the source could be controlled by varying the size and number of holes in the foil cover. In addition to the cavity halves, a number of flat strip-samples were produced so that Nb_3Sn growth rates could be measured. In order to duplicate the reaction environment in which cavity halves were fired, a sample holder was made by milling a 3/8"x3/4" slot in the cup of a used waveguide cavity half. Strip samples, when attached to the back of the cavity half, occupied the same position as the bottom of an unaltered cup. Since large surface r.f. magnetic fields occur at the cup bottom, this is a region sensitive for cavity performance.

Pre-Anodization of Vapor-Diffused Surfaces

As will be discussed further in the following sections, most of the vapor-diffused samples were anodized in 50% NH_4OH to a terminating voltage of 100V just before insertion into the furnace. This anodic coating served as a barrier to prevent formation of Sn-rich phases during the start of the firing cycle while the substrate was at low temperatures.

Details of the firing cycle are also discussed in the following chapter.

C. Preparation of "Pre-Nucleated" Cavities and Strip-Samples

One cavity and two sample strips were produced by a "hybrid" process, in which substrates were ionplated with approx. 0.5 μm of Sn and then fired in the same manner as the vapor-diffused samples. Equipment and procedure were identical to those used for vapor-diffused samples, with the exception of the pre-anodization, which was omitted.

D. Removal of Residual Sn After Firing

A number of cavities and strip-samples had shiny "Sn" spots remaining after the completion of the firing cycle. These spots resisted removal with HNO_3 or HCl. Two empirical methods were used to remove these spots. The first consisted of immersion in an aqueous solution of $FeCl_3$ (75-105 gm/l), $CuSO_4$ (135-160 gm/l) and acetic acid (170-260 cc/l) at a temperature of about 50°C, with ultrasonic agitation. The second consisted of alternate immersions in HNO_3 and HF, both used at room temperature with ultrasonic agitation. The second method was preferred because of the absence of organic or metallic contaminants.

2. Cavity Design, Construction and Preparation

All r.f. tests were made using caviities of the "muffin tin" variety as described in Figure 3. This configuration

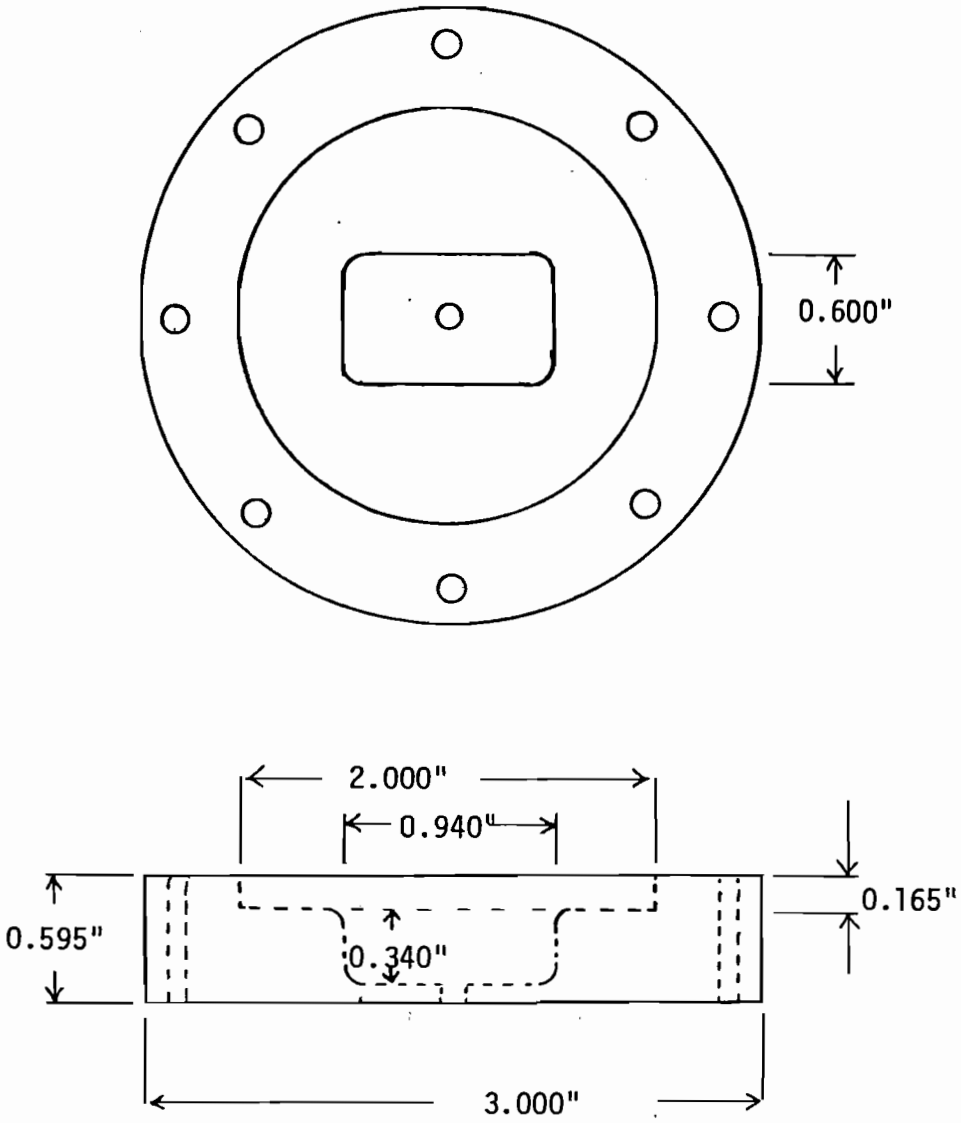

Figure III-3. Waveguide-coupled half-cavity

was developed for synchrotron applications, and consists of two rectangular cavity halves separated by a mid-plane gap or "cutoff zone". The field intensity falls rapidly in the cutoff zone, yielding a low field region at the circumference. This low field midplane region is necessary for synchrotron applications so that synchrotron radiation, emitted circumferentially along the beam path, will not strike high field cavity surfaces.

For test purposes, single cell cavities were used which separated into two open halves, allowing convenient access to all interior surfaces.

Two types of cavities, having identical interior dimensions but different coupling mechanisms, were used. Waveguide-coupled (WG) cavities consisted of two disc-shaped halves of solid Nb as shown in Figure 3, with the rectangular cavity cups and circular cutoff zones machined using a numerically controlled milling machine. The two mating halves are sealed with an indium gasket at the midplane, and fixed two-port coupling to rectangular waveguide feeds is provided for by small circular apertures at the bottom center of each cup.

Probe-coupled cavities (Figure 4) consist of two identical "halves" which are mounted with indium gaskets to a machined Nb "belly band". Adjustable, 1-port coupling is provided by a movable coaxial probe at the top center of the

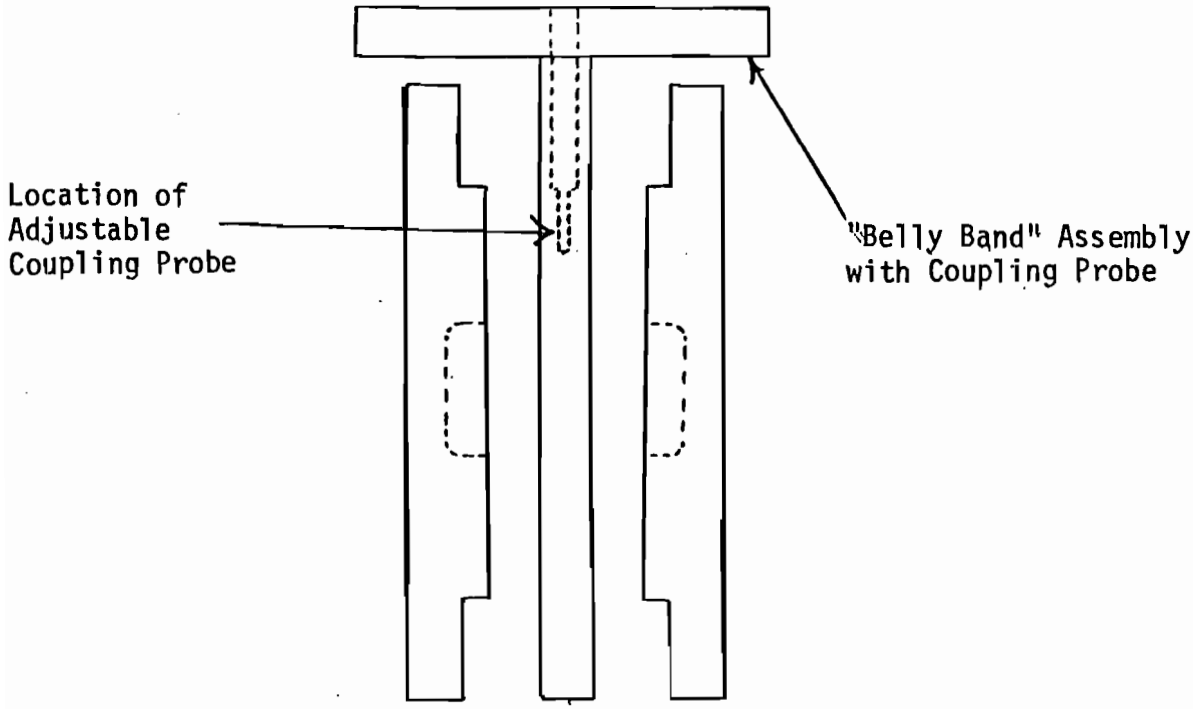

Probe-Coupled

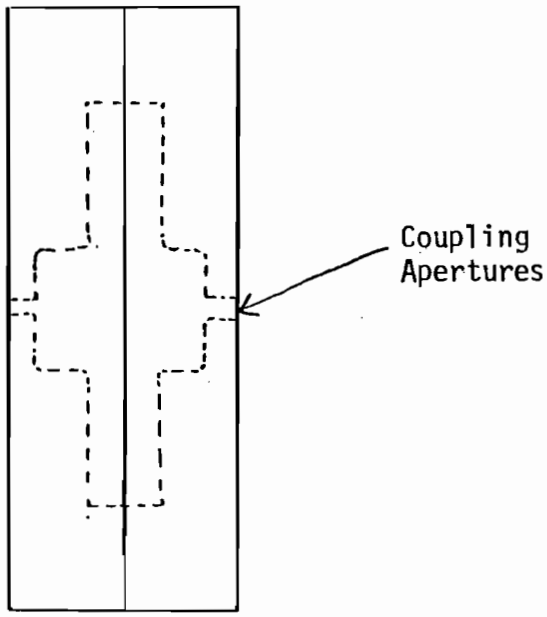

Waveguide-Coupled

Figure III-4. Cavity assembly configurations

belly band. All but one of the probe-coupled cavities were sheet metal cavities similar to those described in ref. 7. Rectangular cups, stamped from 1/32" (0.8 mm) Nb sheet, were electron-beam welded into supporting discs of 1/4" Nb to form each cavity half. The remaining probe-coupled cavity and all of the waveguide-coupled cavities were machined from solid Nb.

Prior to coating with Nb_3Sn, all cavities were given the treatment normally used in this laboratory to prepare Nb cavities. This treatment includes solvent degreasing with ultrasonic agitation to remove machining residues, followed by electropolishing with oscillating current as described in ref. 8. In a few cases mechanical polishing with abrasive grit preceded electropolishing. Prior to receiving Nb_3Sn coatings, most of these cavities had been r.f. tested as part of a parallel development program for Nb X-band cavities. These cavities were UHV degassed at 1800-1950°C.

Pre-Test Assembly Procedure

Preparation for r.f. tests were done using techniques already established for Nb cavities. Cavity halves were given 1-3 cycles of oxipolishing, each cycle consisting of anodization in 50% NH_4OH at a current density of 10 mA/cm^2, removal of the anodic film in 48% HF with ultrasonic agitation, and neutralization in 6% H_2O_2 with ultrasonic agitation, with distilled water rinses after each step. Cavity halves were kept immersed in electronic grade methanol following

oxipolishing, and the interior surfaces were kept wet with methanol during the assembly process. All containers used for oxipolishing or cavity storage were teflon, linear polyethelene or pyrex glass. Aluminum foil covers were used during cavity storage to exclude dust. Cavities were assembled under a filtered laminar flow hood. Indium gaskets were preformed to correct size using a teflon former, and assembly was done quickly to prevent drying of the cavity interior surfaces. Cavities were filled with methanol as soon as the cavity halves were joined together. 8-32 brass threaded rods were used to hold the cavity halves together and had sufficient elasticity to take up the creep of the indium gaskets. After all threads were tightened, the methanol was drained out of the cavity through the coupling hole(s). The cavities were then repeatedly refilled with methanol, shaken and drained to flush out any dust particles which might have entered during assembly, attached immediately following the final flush cycle to the pumping station and evacuated using a mechanical pump and liquid nitrogen cold trap. Once the residual methanol had been pumped out, the mechanical pump was disconnected and the cavity was further evacuated, using a sorbtion pump followed by an ion pump, to less than 10^{-8} mm, pressure being measured at the ion pump.

3. Measurement Procedures

A. T_c Measurements of Strip-Samples

Transition temperatures of all strip-samples were made using a mutual inductance technique as shown in Figure 5. The flat samples were clamped between two rectangular coils, each having approximately 2000 turns of fine wire. A germanium resistance thermometer was bolted to the lower end of the sample and four-terminal resistance measurements were made. The entire assembly was enclosed in a 4" diameter OFHC (oxygen-free-high conductivity) copper pot with OFHC copper top and bottom flanges. A non-inductive Constantan heater winding encircled the copper pot, which was hung from the top plate of a helium dewar by a 1" diameter stainless tube.

In use, the pot was partially evacuated and back-filled with Helium gas, and then inserted into the dewar and suspended over boiling helium. A carbon resistance heater immersed in the helium bath was used to increase the helium boiloff rate, when necessary, to cool the pot.

The superconducting transition is detected as a change in the mutual inductance of the two coils. A low frequency (100-400 Hz) sinusoidal signal is applied to one coil. When the sample is in the normal state, a considerable amount of magnetic flux penetrates through the sample and induces a signal in the second coil. When the sample becomes superconducting, no flux penetrates the sample, and the induced

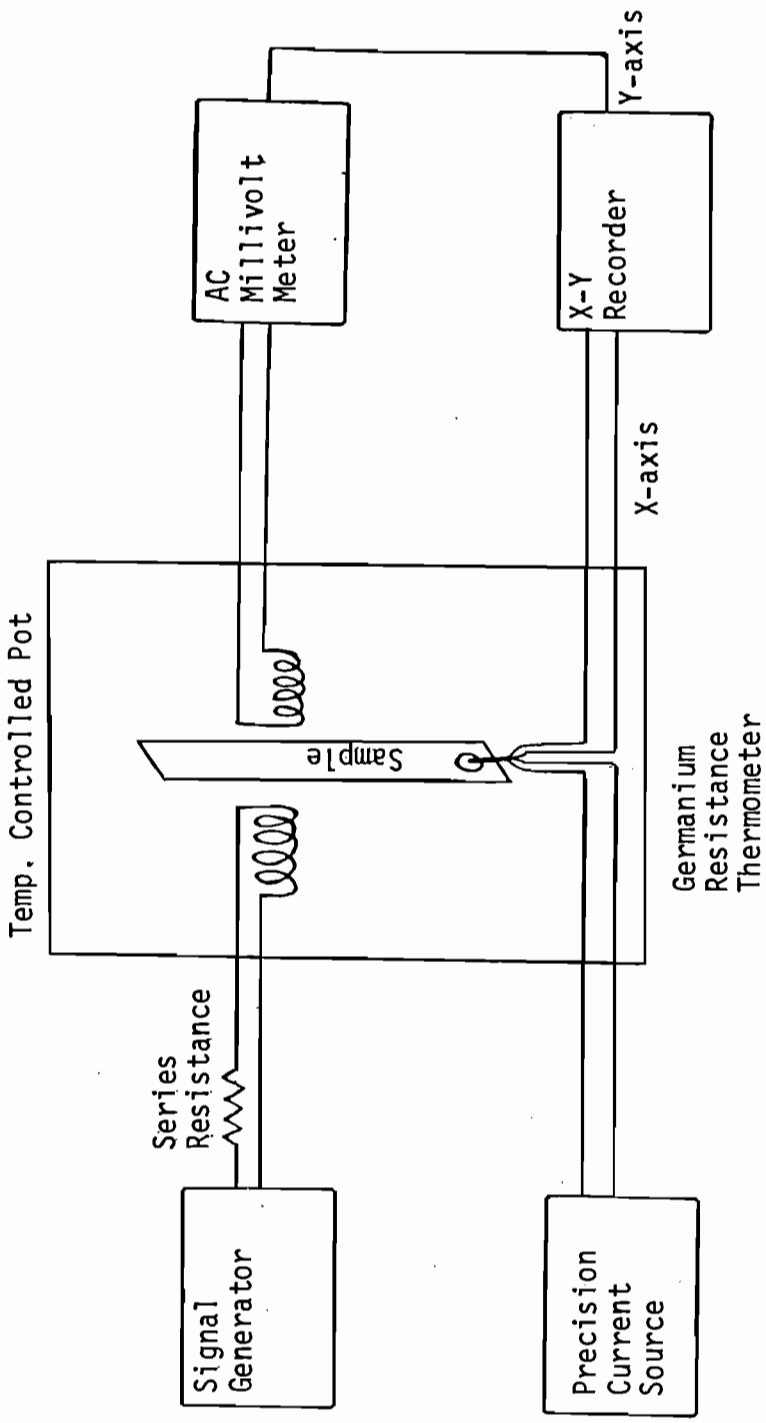

Figure III-5. Instrumentation for T_c measurement of strip-samples

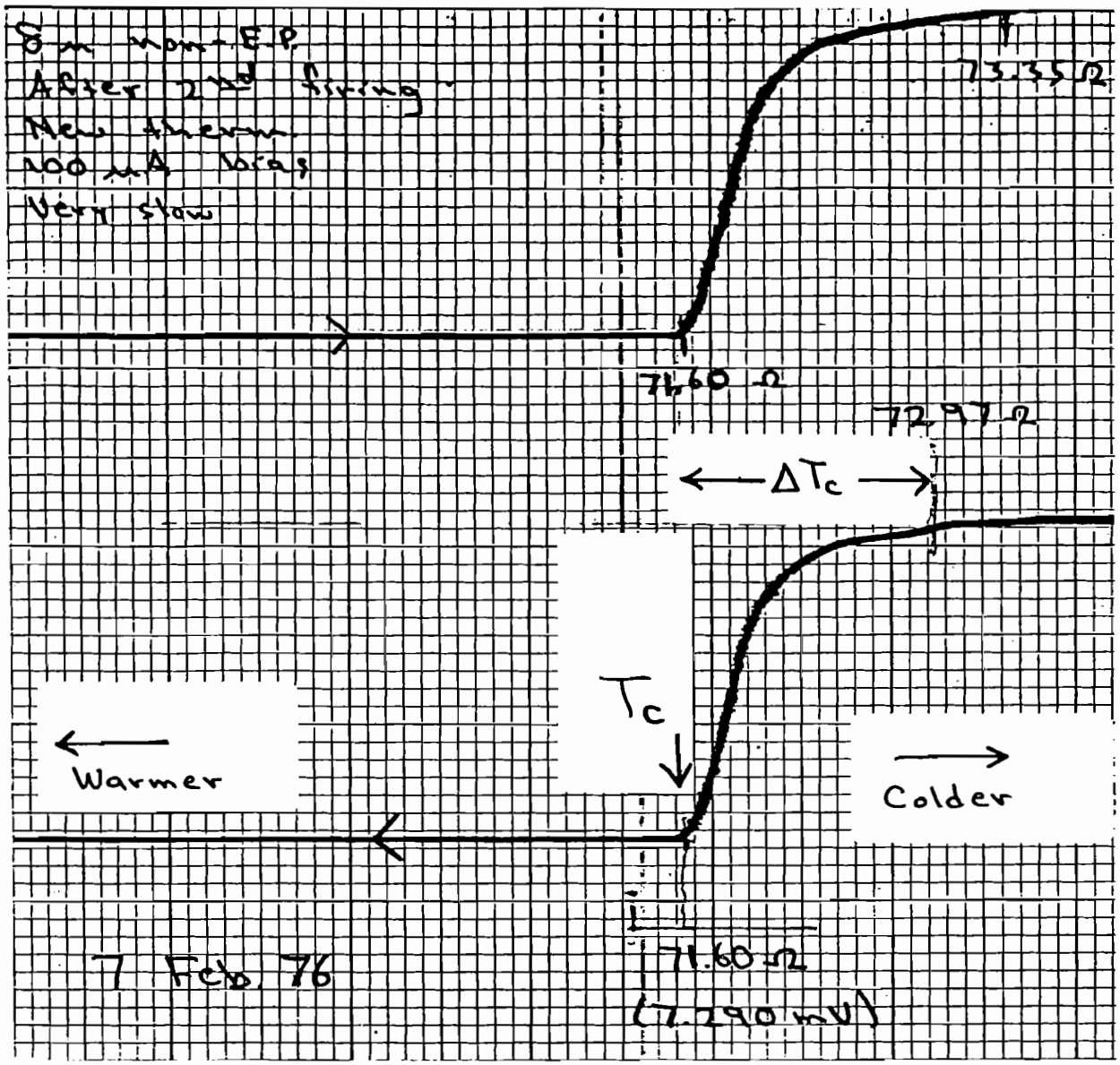

Figure III-6. Typical T_c plot showing definition of T_c and ΔT_c

signal falls to a much lower value. A series resistor at room temperature insures that changes in coil resistance with temperature will not change the amplitude of the signal applied to the sample. The induced signal is measured with an a.c. millivoltmeter, and a d.c. output from the meter is used to drive the y axis of an x-y recorder. Sample temperature is measured by feeding a bias current from a precision current source to the germanium resistance thermometer. The resulting voltage (1-10 mV) is applied to the x axis of the x-y recorder. The x axis is calibrated by substituting a precision decade resistance box for the thermometer, thereby cancelling errors in the bias current magnitude.

A sample plot is shown in Figure 6, showing T_c and ΔT_c determinations. Two traces are usually taken; one obtained by cooling through the transition and a second by warming. T_c and ΔT_c values of the two traces must agree.

B. Cavity R.F. Measurements

1. Low Temperatures ($T < 4.2°K$)

Low temperature measurements sought to determine cavity Q at low and high fields, and also to determine the breakdown field level.

Q measurements of waveguide-coupled cavities were made using the pulse decay technique as illustrated in Figure 7. A traveling-wave-tube amplifier (TWT) and voltage-controlled oscillator are locked at the cavity resonant frequency by a

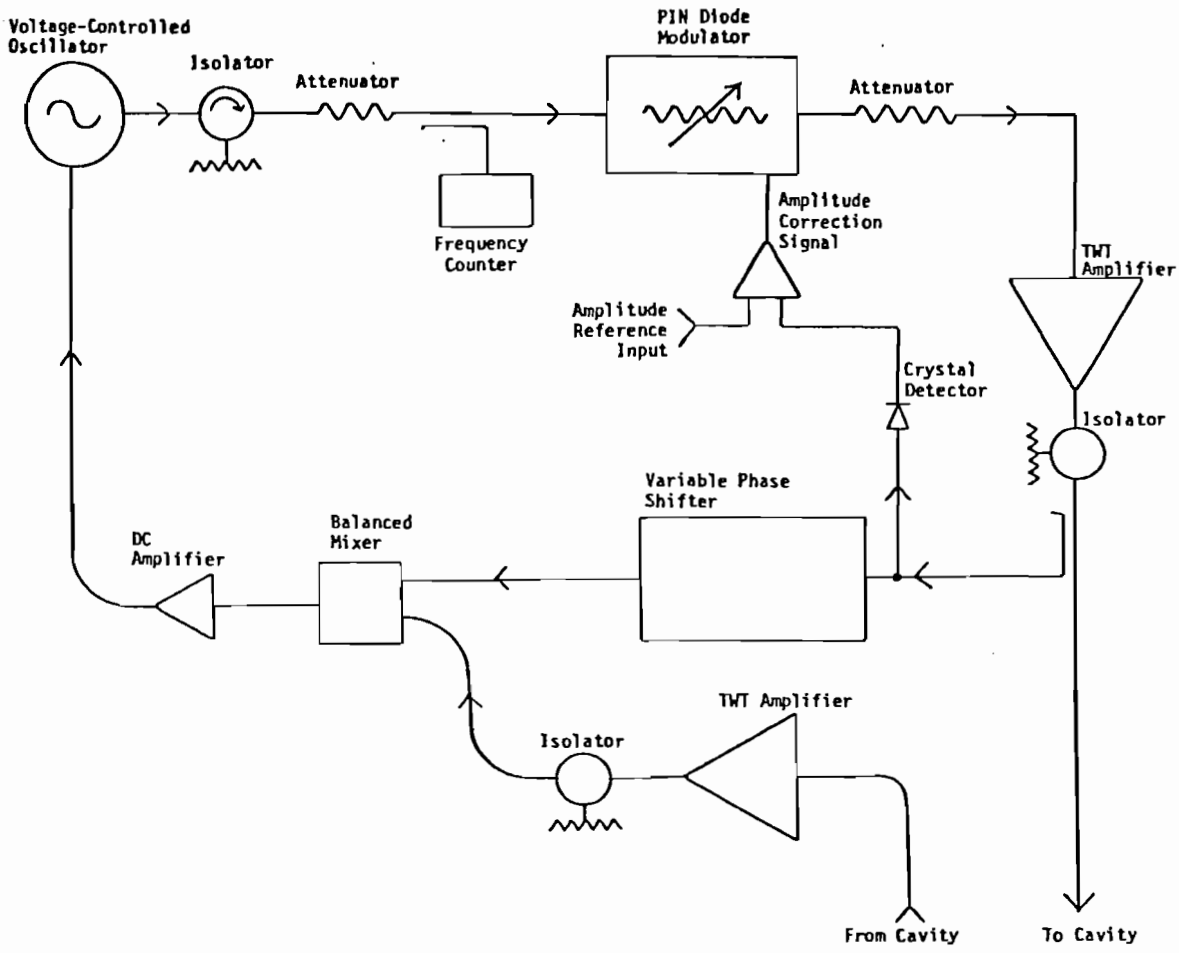

Figure III-7. R.F. measurement equipment diagram

phase sensitive feedback system. A short pulse of power is applied to the cavity and then suddenly cut off. The power P_t emitted from the cavity output port is measured with a crystal detector and displayed on an oscilloscope, and the loaded time constant is measured as the time required for the signal to fall to 1/e of its original value.

The coupling factors β_1 and β_2 are derived from measurements of the incident power P_i, reflected power P_r, emitted power P_e and transmitted power P_t as described in a later section of this chapter. The quantities P_i, P_r, P_e and P_t are obtained by measuring the crystal detector signal levels during various parts of the applied signal pulse, as illustrated in Figure 8.

To insure the accuracy of breakdown field measurements, the crystal detectors were calibrated with a microwave power meter. Calibration was done by replacing the cavity with a short waveguide section and substituting the power meter for the detector to be calibrated. In this manner the effects of waveguide losses and directional coupler coupling factors were included.

Measurements of probe-coupled cavities were considerably simpler since only one coupling factor is involved, and tests can be made at critical coupling ($\beta = 1$, $P_r = 0$, $P_e = P_i$). Calibration was done by detuning the cavity, which then approximates a lossless short-circuit, and measuring both

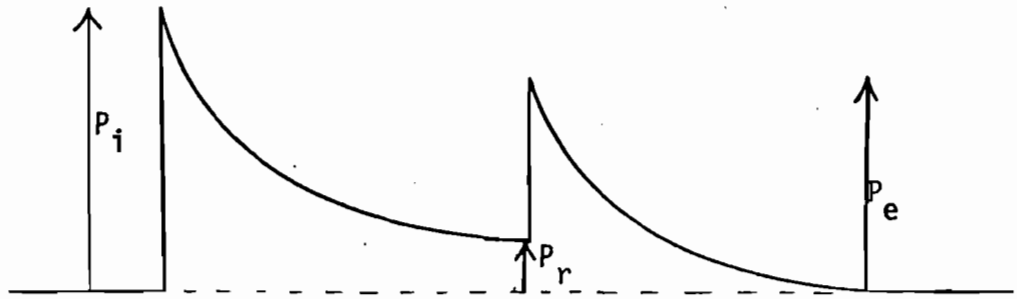

Reflected Power Waveform

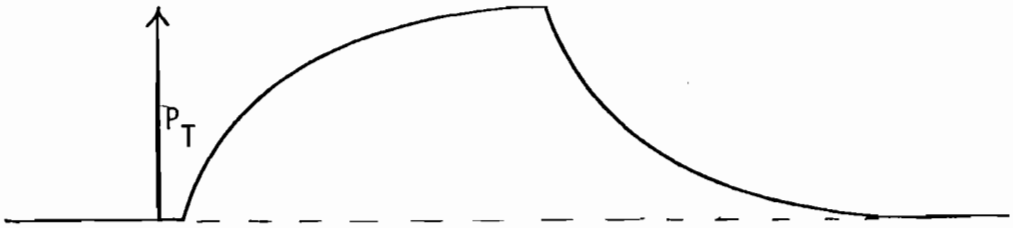

Transmitted Power Waveform

Figure III-8. Definitions of P_i, P_r, P_e, and P_T

incident power P_i and return loss with a power meter. This calibration was repeated every time a measurement of breakdown field was made.

Temperature determination at temperatures below 4.2° was accomplished by measuring the helium bath vapor pressure with a mechanical gauge.

2. High Temperatures ($T > 4.2°$)

High temperature measurements consisted of determining cavity Q and resonant frequency f_o as functions of temperature, and in some cases also included direct measurement of transition temperature T_c.

Temperature Control of Cavities

Cavity temperature control was achieved using techniques similar to those used for strip-sample T_c measurements.

For waveguide coupled cavities, a "cold clamp" is clamped around the cavity after the cavity has been assembled and evacuated. The "cold clamp" consists of a 4"x4"x1" block of OFHC copper which is clamped (Figure 9) tightly onto the cavity and surrounds it at the circumference. The high thermal conductivity of the copper insures that no significant temperature differences exist across the cavity. A second, smaller OFHC copper block is bolted to the bottom and contains two 100Ω heater resistors and a "heat leak". The heat leak consists of a 3/4" diameter copper rod approximately 5" long, which extends downward from the cold clamp

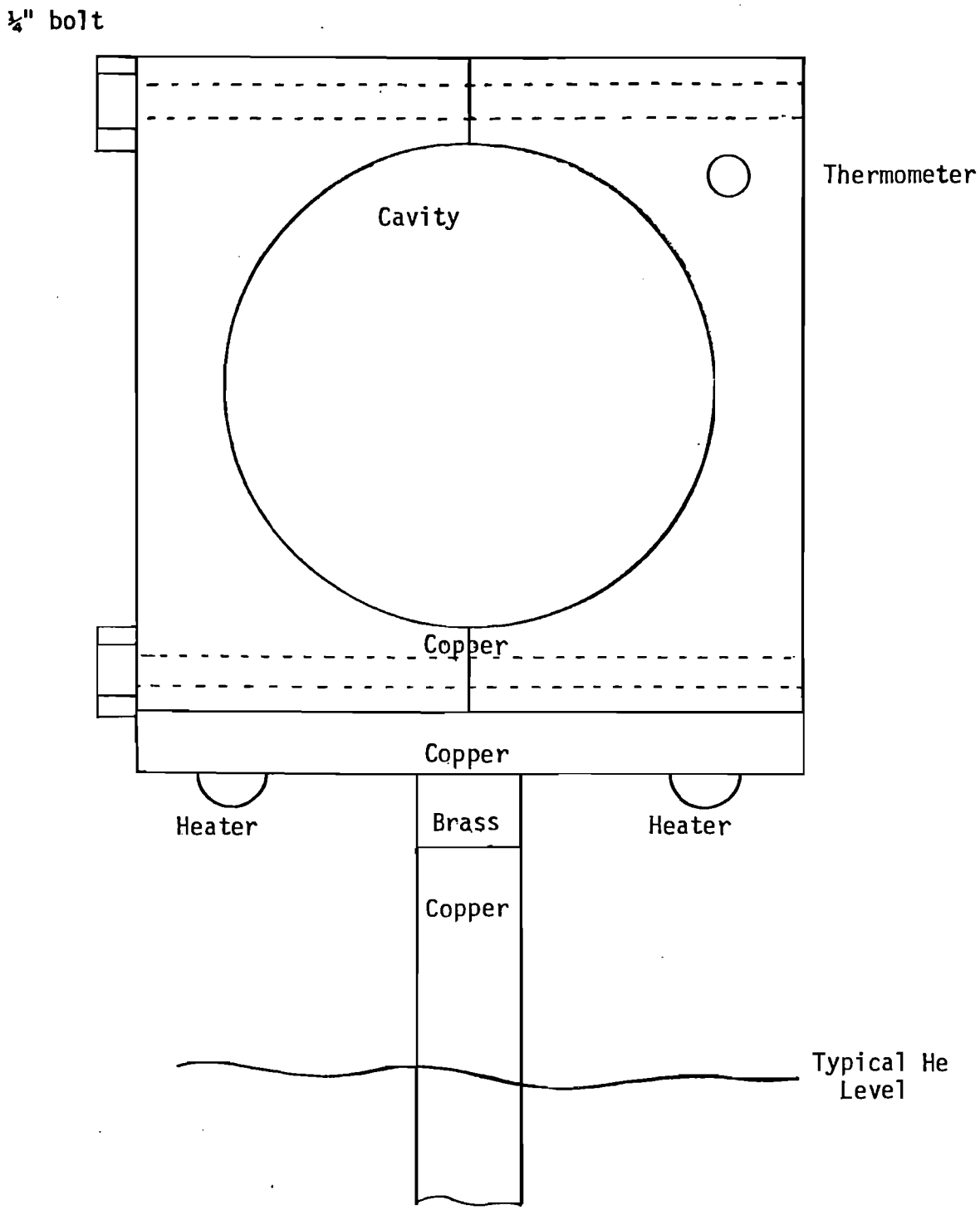

Figure III-9. "Cold clamp" used for temperature control of waveguide coupled cavities

and is immersed in liquid He at its lower end. At the top of this rod is a 3/4" diameter x 3/4" long brass "thermal resistor" which connects the copper rod to the "cold clamp". Since the brass has a much higher thermal resistivity than copper, most of the temperature drop between the LHe bath and the cold clamp occurs across the brass "resistor" and the quantity of heat leaked to the bath is relatively independent of the liquid helium level.

Probe-coupled cavities were controlled using the same heater/heat-leak assembly, but because of the absence of waveguide flanges on these cavities, a simpler cold clamp consisting of two 4"x4"x1/4" OFHC copper plates was used. These plates were clamped on opposite sides of the cavity and had a network of 1/4" holes to allow liquid helium to reach the cup regions during low temperature high field tests.

R.F. Measurements: $Q(T)$, $f_o(T)$

Q and f_o were measured as the cavity was slowly warmed from 4.2° to a peak temperature of 16°-18°. For temperatures between 4.2° and about 12°, measurement techniques were identical to those used for low temperature measurements; cavity time constants, with coupling adjusted to $\beta = 1$, were used for probe-coupled cavities, and time constant measurements, together with measurements of (P_i, P_r, P_e, P_t) were used for waveguide-coupled cavities. Once Q had been determined at a particular temperature, the cavity was run CW for

a moment and the resonant frequency f_o was measured with a frequency counter. The cavity was then warmed to the next desired temperature point and the process was repeated.

At higher temperatures, special techniques were used because of the greatly reduced Q-values obtained in this region.

With probe-coupled cavities, the coupling was left fixed at that setting providing critical coupling at some temperature $T_0 \sim 10°\text{-}12°$, since it was felt that further insertion of the coaxial coupling probe might alter the cavity resonant frequency sufficiently to cause errors in $f_o(T)$ determination. Q-values at higher temperatures were determined by measuring the reflected power ratio P_r/P_i, calculating the coupling factor β, and using the relation

$$Q(T_2) = [\beta(T_2)/\beta(T_0)]\cdot Q(T_0)$$

With waveguide-coupled cavities, the transmitted power P_t provides the phase reference necessary to lock the VCO-TWT combination at the cavity resonant frequency. Since the ratio P_t/P_i becomes very small at high temperatures, pulsed operation was usually not possible. The cavity was therefore run CW and Q calculated from the ratio P_t/P_i, as discussed in Appendix B.

T_c Determination by Swept Frequency Measurement

With probe-coupled cavities, T_c could be determined to within perhaps $\pm 0.2°K$ using a simple swept frequency

technique. The phase locking mechanism was disconnected and a triangle-wave fm signal, centered at the cavity resonant frequency, was applied to the cavity. The reflected power was monitored with a crystal detector and the magnitude of the resonance dip (in mV) was measured as a function of temperature. As cavity temperature was raised slowly to T_c, the resonance dip decreased in magnitude, reaching a constant value for $T \geq T_c$, since the normal state surface resistance is virtually independent of temperature at temperatures slightly above T_c. T_c could thus be taken as the temperature at which the resonance dip first reached this limiting value.

4. Morphological and Composition Examinations

A. Optical Microscopy

The surface textures of the Nb_3Sn samples produced by the two methods investigated varied considerably, from smooth, specular finishes through rough, irregular contours, to crystal clumps of over 1 mm in size. Even samples produced using the same method sometimes showed marked morphological differences depending upon the particular reaction parameters. In addition to revealing these morphological details, optical microscopic examination can be used to determine the presence and topographical distribution of the various phases of the Nb-Sn system if the anodization scheme generally attributed to Picklesimer[9] is employed.

With this addition, microscopic examination becomes a rather powerful analytical tool.

Several authors have reported specific anodization techniques[10-13] for identification of Nb-Sn phases, and a detailed discussion of technique may be found in Appendix C. All of these techniques involve anodization of the sample in an electrolyte to a specified terminating voltage. The thickness of the resulting anodic oxide film depends upon both the terminating voltage and the chemistry of the underlying material. Each phase of the Nb-Sn system thus forms a different thickness of oxide, and the differences in the resulting interference colors may be used to identify the phases. Since the oxipolishing technique generally used to prepare Nb and Nb_3Sn cavities for testing includes just such an anodization process, this method of phase identification is very convenient.

Examination of flat samples (sample strips and flat regions of cavity surfaces) was done with a Zeiss binocular microscope using bright field lighting, 16x objective and 10x eyepieces. Photographs were made with a Zeiss 35mm camera back providing 80x magnification (with 16x objective). Kodak "Photomicrography Color Film 2483" was used and excellent reproduction of the anodization colors was observed.

Large samples (whole cavity halves) were photographed with a Nikon F2 35mm camera with 55mm close-up lens. Kodak

"Vericolor II Professional Film, 5025 Type S" was used, with illumination furnished by two 3400°K photoflood lamps, and an "80B" color correction filter was used over the camera lens.

B. Secondary-Ion-Mass-Spectroscopy (SIMS) Composition Profiles

In addition to optical examinations, composition vs. depth profiles were made using Secondary-Ion-Mass-Spectroscopy (SIMS). With this process one can obtain concentration vs. depth profiles for selected elements in solid materials. The shape of the Sn profile and the depth to which Sn penetrates the Nb substrate provide clues to the mechanism of Nb_3Sn formation.

Description of SIMS Technique

A CAMECA IMS 300 ion microscope was used in this work. An oxygen ion beam with approximately 5.5 keV energy and current of approximately 500 nA was focused onto a spot approximately 30μx30μ and swept repetitively side to side (rastered) to cover a square approximately 280μ on a side. As the ion beam strikes the sample surface, material is sputtered away, and a small fraction of the sputtered atoms are ionized. A focusing mass spectrometer counts sputtered ions having a particular e/m ratio, and the ion count rate is observed as the primary beam sputters deeper into the sample. With proper adjustment of machine parameters, the sputtering rate is constant in time, and a plot of ion count

rate versus time is proportional to the concentration versus depth of the element selected. Details of the process may be found in references 14 and 15. Depth calibration is usually obtained by measuring total sputtering depth with a "Talystep" stylus depth indicator. Vertical (concentration) axis scaling is considerably more difficult, since both sputtering rate and ion yield vary as element selection, sample microstructure or sample chemistry are changed. Quantitative concentration measurements and stoichiometry determination are not readily obtained with SIMS. During any given run, however, sputtering rate and ion yield remain essentially constant, and this was confirmed by the fact that, when operating parameters were correct, flat Nb profiles were observed in the Sn-free interiors of the samples. Some discretion must be used very near the surface, as the first 1000Å or so sometimes show a very high count rate. We therefore consider as significant only that region of a profile beyond a depth of 2000Å, and suspected surface effects are disregarded.

5. Data Analysis Procedures

A. Surface Resistance Determination

The surface resistance R_s of a material and the unloaded Q of a cavity fabricated from that material are related through the geometry factor Γ of the cavity:

$$R_s = \Gamma/Q_o$$

The geometry factor of the single-cell muffin-tin cavity

is 233Ω in the TM_{010} mode as determined from measurements of an OFHC copper cavity model.

The unloaded Q of the cavity may be determined from the loaded time constant τ_L and the coupling factors β_1, β_2:

$$Q_o = 2\pi\omega_o\tau_L(1 + \beta_1 + \beta_2)$$

For probe coupled cavities, $\beta_2 = 0$, and the input coupling is adjusted to give $\beta_1 = 1$ (critical coupling). For waveguide-coupled cavities, with two fixed coupling ports, the coupling factors are calculated from the incident power P_i, reflected power P_r, emitted power P_e and transmitted power P_t as follows:

$$\beta_1 = \frac{1 + \sqrt{P_r/P_i}}{2 - (1 + \sqrt{P_r/P_i})/(1 + P_T/P_e)} \qquad \beta_2 = \frac{P_t}{P_e}\cdot\beta_1 \quad \beta_1 > 1$$

$$\beta_1 = \frac{(1 + \sqrt{P_r/P_e})^2}{1 - P_t/P_i - P_r/P_i} \qquad \beta_2 = \frac{P_t/P_i}{1 - P_t/P_i - P_r/P_i} \quad \beta_1 < 1$$

The resonant frequency ω_o was measured by running the cavity CW and reading the phase-locked VCO frequency with a frequency meter.

B. E_{acc} and H_c^{acc} Determination

Given the Q and power absorbed by the cavity, the peak magnetic field may be calculated. By making these measurements at power levels just below breakdown, H_c^{acc} is determined, provided that the breakdown occurred at the peak field location.

For accelerator applications it is more useful to quote E_{acc}, the effective accelerating field of the cavity. This is the actual energy gained by a synchronous electron passing through the cavity, and is substantially lower than the peak electric field occurring within the cavity. E_{acc} is related to Q and power input through the shunt impedance Z, and we have

$$P_{abs} = (E_{acc}^2/Z) \times d$$

or

$$E_{acc} = (P_{abs} Z/d)^{1/2}$$

where d is the length of the accelerating structure.

For this cavity geometry the shunt impedance has been found to be, at 2.8 GHz,

$$Z/Q_o = 3140 \text{ ohm/m} \qquad (2.8 \text{ GHz})$$

and since, for a given structure geometry, Z/Q_o scales linearly with frequency,

$$Z/Q_o = 9420 \text{ ohm/m} \qquad (8.4 \text{ GHz})$$

This, together with a cavity length along the beam axis of 1.52 cm, gives us

$$E_{acc}(\text{MV/m}) = 0.25(P_{abs}(\text{mW})\tau_L(\text{ms}))^{1/2}$$

For probe-coupled cavities with $\beta_1 = 1$, all of the incident power is absorbed, and $P_{abs} = P_i$. For two port cavities, we have

$$P_{abs} = \frac{4\beta_1}{(1 + \beta_1 + \beta_2)^2}$$

as discussed in Appendix B, and

$$E_{acc}(MV/m) = 0.41 \left[\frac{\beta_1}{(1 + \beta_1 + \beta_2)} P_i(mW)\tau_L(ms)\right]^{1/2}$$

The ratio of peak surface magnetic field to accelerating field for this cavity geometry has been measured and found to be

$$H_{max}(gauss) = 54\ E_{acc}\ (MV/m)$$

C. Superconducting Penetration Depth $\Delta\lambda(T)$

A measurable quantity which is not of fundamental importance for accelerator applications but is useful for diagnostic purposes is the change in penetration depth $\Delta\lambda(T)$ with temperature.

All superconductors, when operating in the Meissner state, exclude magnetic flux from their interiors, but allow some penetration of flux at their surfaces. It is in these surface regions that shielding currents flow, and flux penetration to a depth d is proportional to $\exp(-d/\lambda)$, where λ is the penetration depth. The temperature dependence of λ can be fit very well by the empirical relation[16]

$$\lambda(T) = \lambda_o[1 - (T/T_c)^4]^{-\frac{1}{2}} \equiv \lambda_o \cdot Y \qquad (1)$$

where T_c is the transition temperature and λ_o depends upon the particular superconductor in question. At low temperatures, λ approaches the fixed value λ_o, while near T_c, λ increases very quickly, diverging at $T = T_c$ and allowing complete d.c. flux penetration, with a.c. flux penetration limited by the normal conducting "skin depth".

Measurements of $\Delta\lambda(T)$ are useful for three reasons:

(1) The value λ_o can be related to the mean free path ℓ_o through the BCS theory[17] and is therefore a useful diagnostic. Low values of λ_o should correspond to moderately large values of ℓ_o and low surface resistances.

(2) Selection of a value of T_c which gives the best fit of $\Delta\lambda(T)$ data to Eq. (1) is the most accurate means of establishing T_c's for cavities, since the rapid degradation of Q_o at high temperatures makes direct measurement of T_c difficult and unreliable. This technique also yields the T_c of the Nb_3Sn surface, which might differ from that of the material below the surface. An example of T_c determination is shown in Figure 10.

The data of a single run is plotted vs. four assumed values of T_c. It can be seen that too low a value of T_c gives a downward curvature to the data, while too high a value gives an upward curvature. Determination of T_c by this technique agreed well with swept frequency measurements which were also done on several cavities.

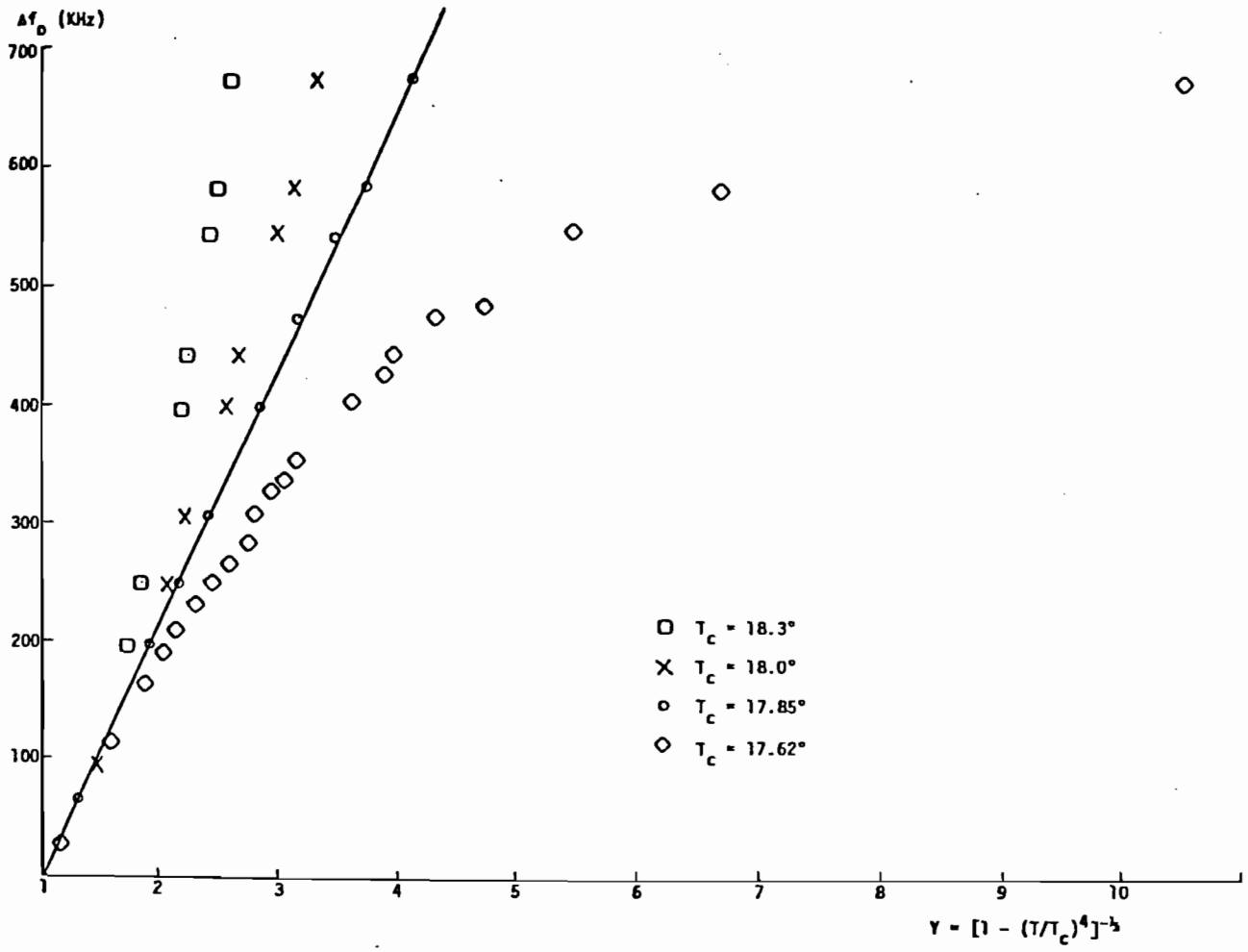

Figure III-10. Determination of T_c and λ_o from $f_o(T)$ measurement

(3) λ_o measurements can also be of some help in diagnosing cavities having high surface resistances. Changes in λ_o reflect "global" effects, i.e. some change in surface properties which extends over a considerable fraction of the cavity surface. Changes in Q_o are more sensitive to local effects, since one very small "bad spot" can drastically reduce cavity Q_o. A low Q_o together with a small λ_o thus suggests a single bad spot, possibly due to cavity contamination, while low Q_o and large λ_o suggest a global effect such as depletion of the Nb_3Sn layer or non-stoichiometry.

Experimental Determination of λ_o

If a plot of $\lambda(T) - \lambda(0)$ vs. $y = [1 - (T/T_c)^4]^{-\frac{1}{2}}$ is available, the slope of this plot $d\lambda/dy$ is λ_o.

Such a plot may be obtained by making careful measurements of the change in resonant frequency of a superconducting cavity as temperature is raised to near T_c. As the penetration depth increases from λ to $\lambda + d\lambda$, the cavity walls in effect move back a distance $d\lambda$, enlarging the cavity and lowering its resonant frequency. The sensitivity of the "muffin-tin" cavity geometry to such perturbations had already been measured for the purpose of developing a frequency tuning technique (differential electropolishing), and the relationship between a change in penetration depth and the resulting frequency change was found to be

$$d\lambda = (1.27)\ \frac{\Delta f_o}{f_o} \quad (cm)$$

Data are obtained by measuring the resonant frequency of the cavity as it is slowly warmed from about 12°K to the highest temperature at which the cavity can be operated. Two special precautions must be taken:

(1) Frequency deviations due to pressure variations must be eliminated. This precludes operation in liquid helium below 4.2°K, as the reduction in vapor pressure necessary to achieve these temperatures will alter the resonant frequency through mechanical deformation of the cavity walls. This is not a problem for Nb_3Sn cavities since all necessary measurements can be made in gaseous helium at atmospheric pressure.

(2) In cavities with variable coupling, one must insure that movement of the coupling probe does not change the resonant frequency, since considerable probe insertion is necessary to maintain unity coupling at high temperatures. With the probe coupled cavities tested, measurements of Q_o at temperatures above about 16°K were made by leaving the coupling fixed and calculating the coupling factor. This allowed simultaneous frequency and Q measurements to be made without extreme probe insertions.

Expected frequency shifts due to thermal expansion of the Nb substrate were estimated from the data of ref. 18 and found to be negligible compared to the shifts observed.

D. $R_s(T)$ Measurements and Analysis

According to BCS theory, the superconducting surface resistance R_s has the form

$$R_s = (R_o\omega^2/T)\exp(-\Delta/kT) + R_{res} \qquad (2)$$

A semilog plot of $T(R_s - R_{res})$ should therefore yield a straight line with slope Δ/k.

Such a plot can be made in conjunction with a $\Delta\lambda(T)$ measurement and yields useful information:

1) The ratio Δ/kT_c can be derived from the slope. This ratio yields information about the phonon spectrum which, for Nb based superconductors, is not readily measured using other techniques.
2) The presence of exposed Nb, due to incomplete coverage by a new Nb_3Sn layer or depletion, through oxipolishing or other chemical means, of an old layer, is revealed by structure near 9°K in a plot of $R_s(T)$.
3) Inhomogeneities in the Nb_3Sn, resulting in variations in T_c, can be revealed by structure at higher temperatures.

In order to fit Eq. (2), the residual resistance R_{res} must be subtracted from the measured surface resistance. This

is most easily done by determining R_s at 1.5°K or lower, where the value is dominated by the residual resistance. In some cases this was not possible, since the "cold clamp" used for temperature regulation at higher temperatures often precluded operation below 4.2°K. In these cases, all of which showed some rounding of the $TR_s(T)$ line at 4.2°K, a best fit R_{res} was chosen to yield a straight $TR_s(T)$ plot.

With probe coupled cavities a further correction was investigated to account for the presence of the Nb belly band, since these cavities almost always showed 9° structure. A plot was made of the form

$$R_s(T) = R_s^{Nb,Sn}(T) + \alpha R_s^{Nb}(T_c^{Nb},T) + R_{res} \qquad (3)$$

where α represents the effective area of the exposed Nb belly band and values of R_s^{Nb} were taken from the work of Lyneis[18]:

The plots were prepared as follows:

a) Using the normal state resistivity of Nb, a value of α was chosen which gave a fit to Eq. (3) in the region $9.2° < T < \sim 12°$.

b) A value of T_c^{Nb} was then selected to yield a smooth fit for $9.2° > T > 7°$ with the given value of α. Because of the singular behavior of R_s^{Nb} near T_c^{Nb}, selection of α alone could not yield a smooth fit.

c) Using these values (α, T_c^{Nb}), a plot of (3) is made.

d) R_{res} is then subtracted as usual.

The contribution of the belly band at temperatures below about 6° was found in all cases to be insignificant. Fitted values of the constant α did, however, vary considerably from run to run. This variation arises from the existence of "ring modes", or excitations of the hollow ring formed by the belly band and cavity halves. The degree of coupling between these ring modes and the accelerating mode is very sensitive to slight misalignment during cavity assembly. The presence of structure in $R_s(T)$ near 9° for probe coupled cavities was therefore not a reliable indicator of depleted Nb_3Sn unless the structure was very pronounced. The belly band corrections did allow an easier determination of the slope Δ/kT_c, however.

Figure 11 shows a plot of $TR_s(T)$ for a probe coupled cavity. The three curves show measured data without corrections, after belly band corrections, and after residual resistance subtraction.

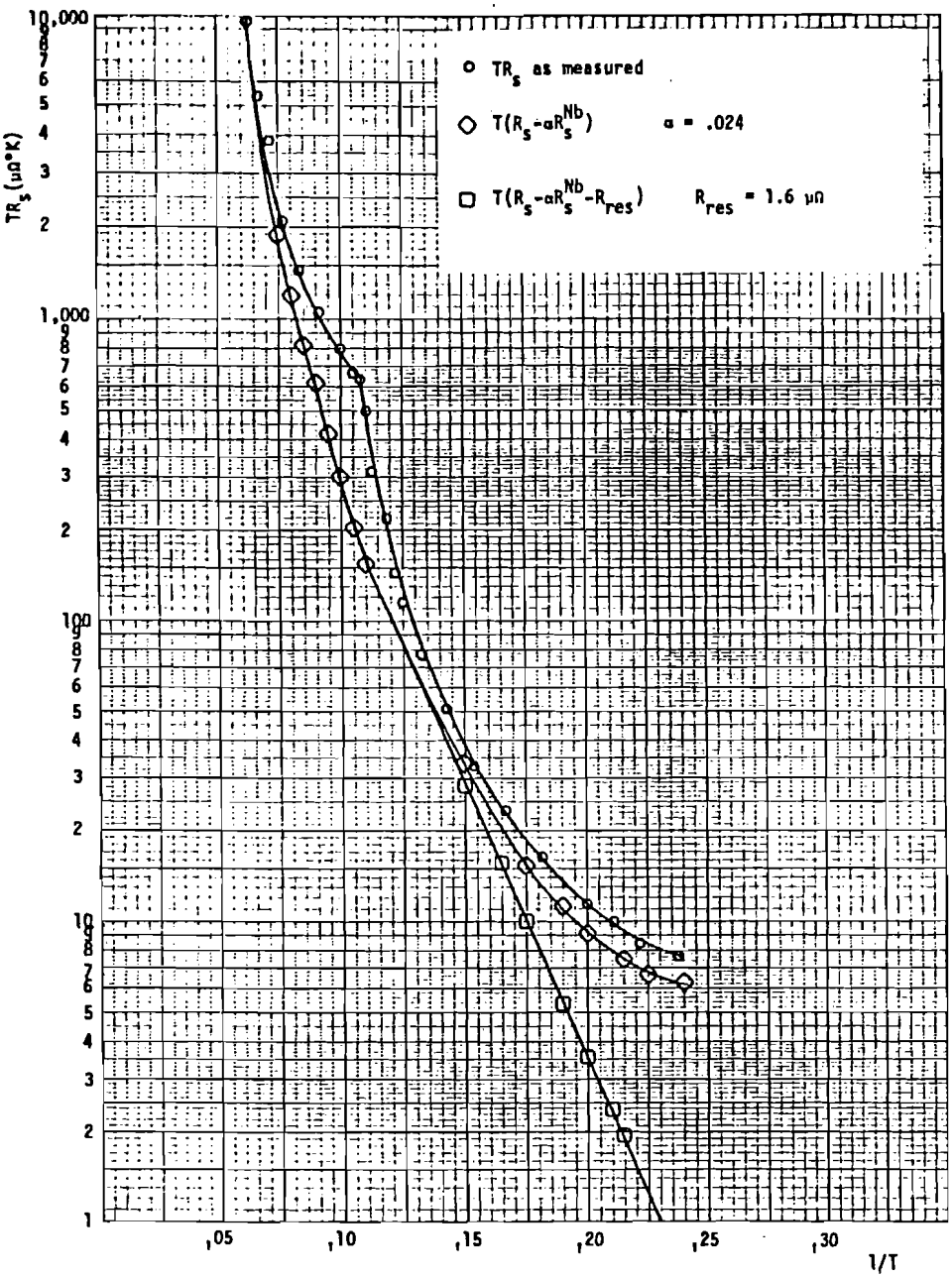

Figure III-11. TR_S plot showing "belly band" correction and residual resistance subtraction

References for Chapter III

1. Mattox, D. M., Sandia Laboratories Report SC-DR-281-63 (1963).

2. Hale, G. J., White, G. W., and Meyer, D. E., Electronic Packaging and Production, May 1975, pp. 39-45.

3. Meyer, D. E., Electronic Packaging and Production, October 1976.

4. Teer, D. G., 1977 International Conference on Metallurgical Coatings, San Francisco, March 28-April 1, 1977.

5. Barbee, T. W., Jr., 1977, International Conference on Metallurgical Coatings, San Francisco, March 28-April 1, 1977.

6. Hahn, H., and Halama, H. J., "AES Depth Profile Measurements of Niobium for Superconducting Cavities", Brookhaven National Laboratory. (Unnumbered report)

7. Padamsee, H., 1976 Applied Superconductivity Conference, Stanford University, August 1976.

8. Diepers, H., Schmidt, O., Martens, H., and Sun, F. S., "A New Method of Electropolishing Niobium", Phys. Lett. 37A, 139 (1971).

9. Picklesimer, M. L., "Anodizing as a Metallographic Technique for Zirconium Base Alloys", ORNL-2296, Metallurgy and Ceramics TID-4500 (13th Ed.), Oak Ridge National Laboratory.

10. Macphail, I., "A Metallographic Technique for Niobium-Tin Alloys", U.K. Atomic Energy Authority Research Group Report AERE-R5421, Harwell, Berkshire, 1967.

11. Enstrom, R., Courtney, T., Pearsall, G., and Wulff, J., "Current and Field Dependence of Superconductivity on Microstructure in the Niobium-Tin System", Metallurgy of Advanced Electronic Materials, G. E. Brock, ed. (Wiley, New York, 1963).

12. Wyman, L. I., Cuthill, J. R., Moore, G. A., Park, J. J., and Yakowitz, H., "Intermediate Phases in Superconducting

Niobium-Tin Alloys", J. Res. of the NBS--A. Physics and Chemistry 66A, No. 4, July-August 1962.

13. Hillenbrand, B., Martens, H., Pfister, H., Schnitzke, K., and Uzel, Y., "Superconducting Nb_3Sn Cavities with High Microwave Qualities", 1976 Applied Superconductvity Conference, Stanford University, August 1976.

14. Evans, C. A., Anal. Chem. 44, 67 (1972).

15. Morrison, G. H., and Slodzian, G., Anal. Chem. 47, 933A (1975).

16. Park, R. D., Superconductivity (M. Dekker, New York, 1969).

17. Kneisel, P., Stoltz, O., and Halbritter, J., "Nb_3Sn for Superconducting R.F. Cavities", Intnl. Cryogenic Materials Conf., Queens Univ., Kingston, Ontario, 1975.

18. Lyneis, C. M., "Experimental Studies of the Microwave Properties of 8.6 GHz Superconducting Niobium, Niobium-Tantalum and Tantalum Cavities", Ph.D. thesis, Stanford University, 1974.

IV. RESULTS

1. Plated Strip-Samples

Experimental work was begun with the production of ion-plated strip-samples. This preliminary work with relatively inexpensive samples facilitated determination of appropriate reaction times and temperatures, and uncovered several unanticipated technical problems requiring attention before cavity fabrication could commence.

Initial reaction temperature was set at 950°C, just above the stability limit of the tin-rich phases Nb_6Sn_5 and $NbSn_2$.

Two thicknesses of plated Sn were used: 5 μm and 8 μm. Reaction times were calculated as the time necessary to remove all of the surface Sn by simultaneous diffusion and evaporation. These calculated times were 60 minutes for 5 μm layers and 83 minutes for 8 μm layers.

Table IV-1 describes the results of the plated sample-strips.

Table IV-1. Ion-Plated Strip-Samples

Sample	Preparation	Warmup Rate	Temp./Time	$T_c/\Delta T_c$	Comments
2-1	Not electropolished 8 μm Sn	Fast	950°/83 min	17.5°/.187°	Matte finish, no lumps
2-1	Refired	Fast	950°/83 min	17.5°/.187°	Anodized color uniform blue-purple
2-2	Electropolished 8 μm Sn	Fast	950°/83 min	17.1°/.200°	Tin lumps remaining
2-3	Electropolished 8 μm Sn	Slow	950°/83 min	17.1°/.500°	T_c shows 2 distinct slopes Tin platelets cover sample
2-4	Electropolished 8 μm Sn	Slow	950°/83 min	15.8°/broad	Lumpy Sn after firing
2-4	Refired	Slow	950°/60 min	Same	
2-6	Electropolished 8 μm Sn	Fast	1150°/83 min	17.8°/2.2°	
3-1	Electropolished Sputter cl 7 μm Sn	Fast	960°/83 min	17.5°/.150°	Lumpy Sn after firing
3-2	Same	Fast	1050°/83 min	17.5°/--	Flat, crystalline Sn platelets after firing
3-3	Same	Fast	1150°/83 min	17.5°/	Sn evaporated, leaving "leopard spots". Oxipolishing 1.5 doesn't change T_c or ΔT_c

Table IV-1 (continued)

Sample	Preparation	Warmup Rate	Temp./Time	$T_c/\Delta T_c$	Comments
3-4	Same	Fast	Same	17.85°/.085°	SIMS analyzed
3-4	Same	--	750°/20 hr	17.7°/.085°	Annealed
3-6	Same and 1000 Å sputtered Nb	Fast	1050°/83 min	17.7°/.190°	No lumps, much smoother finish Excess Sn and dissolved Nb on surface. Removing 0.8 μm leaves T_c, ΔT_c unchanged
4-1	Electropolished 0.4 μ plated Sn	Fast	1000°/30 min	17.8°/.5°	Tiny leopard spots
5-1,5-2 5-3	Electropolished, "Textured" 8 μ ionplated Sn	Fast	1000°/83 min	--	Textured by tumbling or abrading with various grit sizes. All had Sn lumps.
"Addis"	Electropolished 7 μ plated Sn, 1000 Å sputt. Nb	Fast	1050°/120 min	18.0°/.100°	No lumps or leopard spots
4-2	Electropolished, 0.4 μ , ionplated Sn, 1000 Å sputt. Nb	Fast	1000°/30 min	17.8°/.65°	No lumps but coverage looks irregular

Discussion

The first strip-samples to be fired revealed an unanticipated problem with the plate-and-fire technique. Upon heating, the tin formed into droplets as deep as 1-2 mm, leaving between these droplets a much thinner layer of tin. During the firing cycle, the tin in the interspot regions diffused into the niobium substrate as planned, and as the transition temperatures of this strip and of other strips exhibiting this behavior were between 17° and 18°, these regions, at least, were forming ordered Nb_3Sn.

The droplets appeared to have dissolved an appreciable amount of Nb. This was indicated by two facts:

1) The solidified droplets resisted removal in HNO_3 and HCl, both of which attack pure tin.
2) Anodization of the strips revealed a blue tinge to the spots. (For details of the anodization technique, see Appendix C.)

The droplets proved very difficult to remove, yielding only to alternating application of HNO_3 and HF, or to an aqueous tin-stripping bath consisting of $FeCl_3$ (75-105 gm/l), $CuSO_4$ (135-160 gm/l) and acetic acid (170-260 cc/l). After stripping with the latter formula and anodizing, one sample showed distinct rings of orange and blue under the droplets, suggesting a multi-phase composition. By raising the reaction temperature, the excess Sn in these droplets could

be evaporated, leaving rough "leopard spots" or "measles" where the droplets had been. Anodization of these samples indicated single-phase Nb_3Sn, despite their coarse surface texture.

All of the ion plated samples showed this droplet formation, with the exception of one strip which had not been electropolished prior to plating and had the matte finish characteristic of rolled sheet metal. Presumably this increased surface roughness enhanced wetting of the substrate and allowed it to diffuse in without forming droplets. A series of electropolished strips with surfaces abrasively roughened with various grit sizes all showed droplet formation, however, and since previous work with niobium indicated that electropolished or similar stress-free surfaces were necessary for good r.f. performance, attempts to enhance wetting by roughening the substrate surface were not pursued further.

Finally, a technique was developed which prevented segregation of tin into droplets. An ion plated strip identical to the others was sputtered with approxiately 1000Å of Nb and then fast fired 83 minutes at 1050°C. The resulting strip had a matte finish, with excess tin uniformly distributed over the surface. After stripping the excess tin, the transition temperature was 17.7°, and the anodized color suggested uniform Nb_3Sn. Two other Nb-sputtered samples

were later fired and were also free from tin agglomeration.

Two warmup rates were used. "Slow fired" samples were put into an initially cold furnace and heated to 950° C in 40-60 minutes. Two strips fired this way showed relatively low transition temperatures and broad transition widths, as indicated in the table. Refiring one such strip (2-4) did not affect T_c or ΔT_c, thus indicating that insufficient reaction time was not a factor. It seems likely that formation of Sn-rich phases occurred during the slow warmup, and that these phases then formed diffusion barriers which inhibited complete formation of Nb_3Sn once operating temperature was attained.[1]

"Fast fired" samples were inserted into a preheated furnace and reached operating temperature in 2-5 minutes. This procedure resulted in higher T_c's and narrower transition widths, and was used for the rest of the samples.

The T_c results show little correlation between reaction temperature and T_c or ΔT_c within the 950°-1150° range.

2. Ion-Plated Cavity Results

Following the completion of this strip-sample study, work was begun on testable cavities using the plate-and-fire technique. Both waveguide-coupled and probe-coupled cavities, as described in Chapter III, were used for r.f. testing of plated-and-fired surfaces.

The ion-plating process used was the same as that used

for the strip samples. Two cavities, one waveguide coupled and one probe coupled, were given 0.1 μm sputtered Nb coatings over the ion plated Sn, as discussed in Chapter III.

A new, larger furnace was built to fire cavity halves, using the same construction techniques and materials as were used for the smaller furnace used to fire the earlier strip-samples. The larger furnace was, however, limited to a maximum safe operating temperature of about 1050°, about 150° lower than that of the small furnace. Since the 1150° reaction temperature used for some of the strip-samples had not resulted in a significant improvement in $T_c/\Delta T_c$ but had been employed to enable complete evaporation of unreacted Sn, a standard reaction temperature of 1050°C was chosen and reaction time was increased as necessary to eliminate residual Sn.

The testing program for each cavity consisted of a series of r.f. tests, with a 0.1 μm-0.3 μm layer of Nb_3Sn removed by oxipolishing after each test. This cycle continued until visual inspection or deteriorating r.f. performance indicated significant depletion of the Nb_3Sn layer.

Results are indicated in the Tables IV-2 and IV-3

Table IV-2. Ion-Plated Cavity Preparation Details

Cavity #		Prev. Nb Perf.[d] Q_o	E_{acc}(MV/m)	Plating Details	Reaction[a] Parameters Time	Temp.	Comments
#1WG	WG, solid Nb	$1x10^9$	8.5	10 μm Sn	10 hr[b] 10 hr	1000° 1000°	Large leopard spots, no residual Sn
#1SM	Probe coupled sheet metal cups	$3x10^9$	15	7 μm Sn	3 hr 5 hr	1050° 1050°	Slight resid. Sn removed w/HCl 2 mm leopard spots cover both halves
#2WG	WG, solid Nb	$7x10^8$	3.5	8 μm Sn + 0.1 Nb	3 hr 3 hr	1050° 1050°	Smooth matte finish, no residual Sn[c]
SPC	Probe coupled solid Nb			7 μm Sn + 0.1 μm Nb	3 hr 3 hr	1050° 1050°	Smooth matte finish. Prominent Nb grains. No residual Sn.

Notes:
a 2 halves per cavity; each half fired separately.
b First half fired 3 hrs. and examined. Residual Sn still present, so refired an additional 7 hrs.
c See text for further description.
d Best Q_o and E_{acc} achieved for those cavities which were tested as Nb cavities prior to coating with Nb_3Sn.

Table IV-3. Ion-Plated Cavities: R.F. Test Results

Cavity No.	Pre-test Preparation	R.F. Results Q_0 (4.2°)	Q_0 (<2°)	E_{acc} (4.2°)	E_{acc} (<2°)	T_c	λ_o (Å)	Comments
#1 WG	Oxipolished (O.P.)	1.5×10^7	2.1×10^7	--	--	--	--	
	O.P. 2x50V	8.6×10^7	8.6×10^7	--	--	--	--	
	Warmed and recooled	1.25×10^8	--	--	--	--	--	
	Oxipolished	9.2×10^7	--	--	.2-2 MV/m	17.3°	~2000	Structure at 8.2° in $R_s(T)$
	Oxipolished	4.7×10^7	--	--	--	--	--	Cavity heating even at low field levels $R_s(T)$ structure at 8.9°, 13.9°
	Oxipolished	6×10^7	--	--	--	17.85°	3210	
#1 SM	O.P. 50 V	1×10^7	--	--	--	--	--	
	O.P. 100 V (Total 150 V)	2×10^7				~17.5°	--	Heating even at low field $R_s(T)$ structure at 9.2°, 4.95°
	O.P. 100 V (Total 250 V)	3.3×10^7	4.1×10^7	3.8	--	--	--	Heating limits E_{acc}
	O.P. 2x100 V (Total 350 V)	5.8×10^7	2×10^8	3.2	3.8	--	--	Heating limits E_{acc}
	O.P. 2x100 V (Total 550 V)	6.2×10^7	1.2×10^8	4.6	5.0	--	--	
	Outgassed (boiled) Annealed 20 hrs 750°C	1.2×10^8	2.2×10^8	4.5	5.2	--	--	$R_s(T)$ structure at 9°, 3.5°
	O.P. 75 V	6.1×10^7	1.1×10^8	--	--	--	--	$Q < 6\times10^6$ at 1.5 MV/m
#2 WG	O.P. 2x100 V	5.5×10^7	8×10^7	1.9	1.9	--	--	Fast, repetitive breakdown
	O.P. 100 V (Total 300 V)	8.5×10^7	1.1×10^8	2.0	2.0	--	--	Fast, repetitive breakdown
	O.P. 100 V (Total 400 V)	6.1×10^7	7.6×10^7	2.1	2.1	--	--	Cavity possibly contaminated
	O.P. 2x100 V, boiled	1.6×10^8	2.6×10^8	2.1	2.1	17.8°	3070	No $R_s(T)$ structure
	O.P. 2x100 V (Total 800 V)	1.2×10^8	1.5×10^8	--	--	--	--	Same periodic breakdown
SPC	O.P. 2x100 V	--	--	--	--	--	--	Equip. failure, no data degrades quickly with field
	O.P. 2x100 V	2.1×10^8	--	2.7	--	--	--	No heating lumps $R_s(T)$ structure at 9°
	O.P. 3x50 V	2.1×10^8	2.5×10^8	2	2	--	--	Massive Q-drg at high field but CW operation at 2 MV/m possible

Discussion of Ionplated Cavity Results

Cavity Appearance: Surface finish of the ionplated cavities fell into two classifications. The "plain" ionplated cavities #1WG and #1SM had rough, spotted surfaces as described earlier in the discussion of strip-sample results. Cavities #2WG and SPC, which were given additional 0.1 μm sputtered Nb coatings, had uniform matte finishes over most of their interiors. Cavity #2WG (Figure 1) showed, in addition, several shiny regions which had the smooth surface finish of the original electropolished Nb rather than the somewhat rougher, non-reflective finish of the remainder of the cavity. Although these spots bore a superficial resemblance to unreacted Sn, subsequent anodization indicated that they were single-phase Nb_3Sn.

Nature of R.F. Results

The most striking characteristic of the ionplated cavities was the rapid decrease in Q with increasing field level. As an example, the Q of cavity SPC during one test was 2.1×10^8 at a field of 0.22 MV/m. Q decreased to 1.9×10^8 at 0.27 MV/m, 1.4×10^8 at 0.45 MV/m, 1.14×10^8 at 0.64 MV/m and decreased steadily to 6.6×10^6 at 2.7 MV/m.

With probe-coupled cavities, Q-degradation rather than magnetic breakdown, was the factor limiting high field

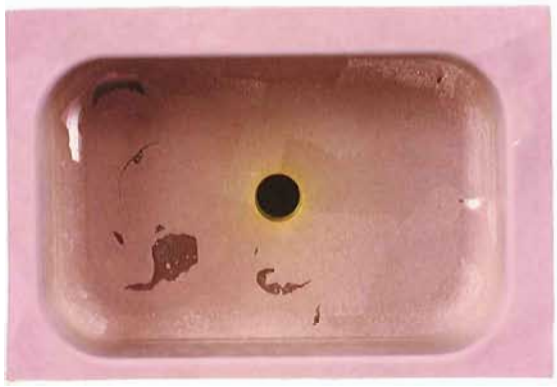

Figure 1. Interior of #2WG showing shiny spots

Figure IV-1

performance. With these cavities, the coaxial probe was adjusted to give critical coupling ($\beta = 1$, $P_r = 0$), and in the absence of Q-degradation, the waveform of Figure 2a resulted. At moderate field levels and long pulse durations, a heating lump was observed in the reflected power waveform as shown in Figure 2b. The appearance of this heating lump was found to correlate with the appearance of heat pulses on carbon resistance thermometers attached to the cavity cup exterior, and was therefore assumed to result from heating of the cavity interior walls.

By shortening the pulse duration, field levels could be increased further, as in Figure 2c. At still higher field levels, however, the heating occurred in a time less than the cavity time constant. Higher field levels could be achieved only by further shortening the pulse duration and increasing the coupling factor to allow the cavity to fill faster (Figure 2d). This process reached a practical limit for pulse durations of 10-30 μs. Although field levels slightly higher than the values quoted in the table could probably be achieved for very short pulse durations, these field levels could not be accurately nor consistently measured and would not in any case be useful for acceleration applications.

High-field performance of the two waveguide-coupled cavities appeared to be limited by breakdown at the coupling

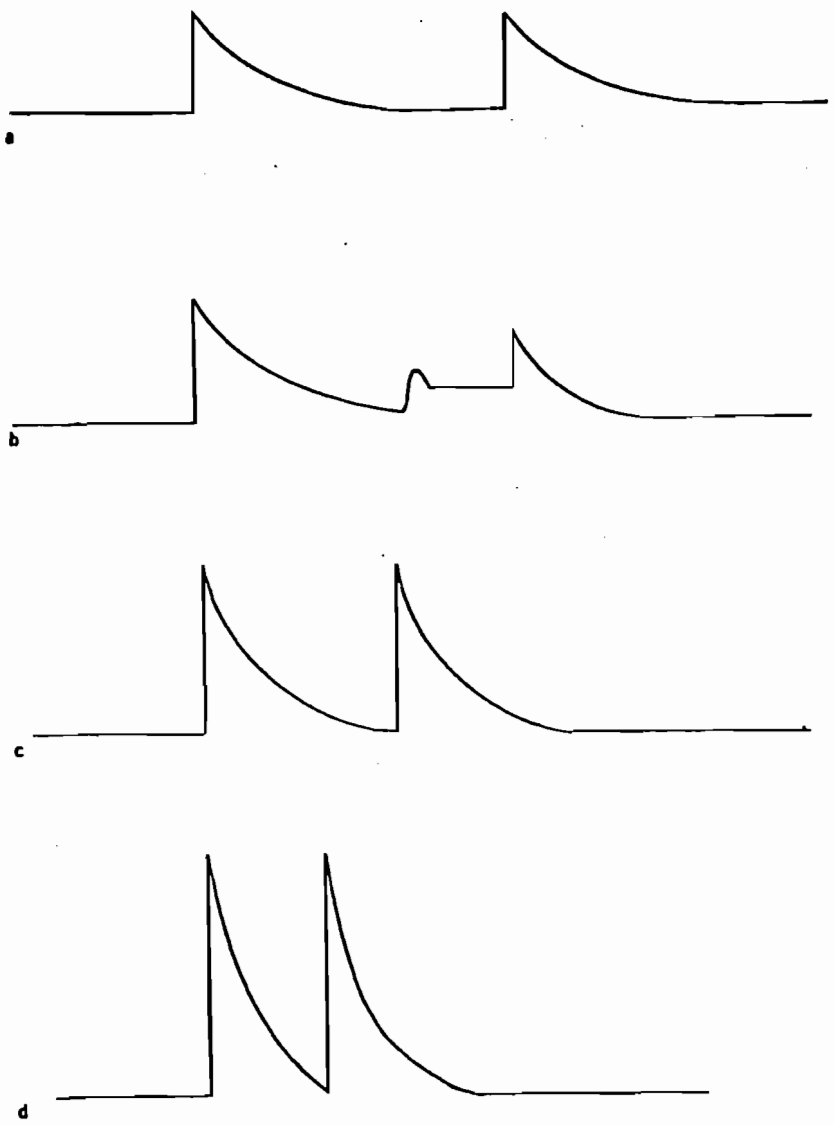

Figure IV-2. Reflected power waveforms indicating cavity heating

holes. Both cavities showed substantial Q-degradation before the coupling-hole limit was reached, however, and the difference in breakdown behavior between waveguide-coupled and probe-coupled cavities is probably due to their geometrical difference rather than to any difference in the Nb_3Sn coatings. Very little improvement in Q or breakdown field resulted from lowering operating temperature below 4.2°.

A slight difference appears between the tabulated low-field Q values of the Nb-sputtered cavities #2WG and SPC and those of cavities #1WG and #1SM, which were fired and tested a few months earlier. This difference is probably at least partially attributable to the experience with oxipolishing and very low field Q measurement techniques gained during this period. In any event the difference is not large, the two earlier cavities showing surface resistances of about 1.9 μΩ, and the latter two yielding 1.2-1.5 μΩ, all values measured at 4.2°.

$R_S(T)$ Results

Two $R_S(T)$ plots (Figures 3,4) are shown below for cavity #2WG (Nb sputtered) and cavity #1WG (not sputtered). Both cavities were oxipolished a total of approximately 500-600V (1.5-1.8 μm). As can be seen from the plots, the Nb-sputtered cavity shows no $R_S(T)$ structure, while the non-sputtered cavity shows a discontinuity of slope at 8.2°.

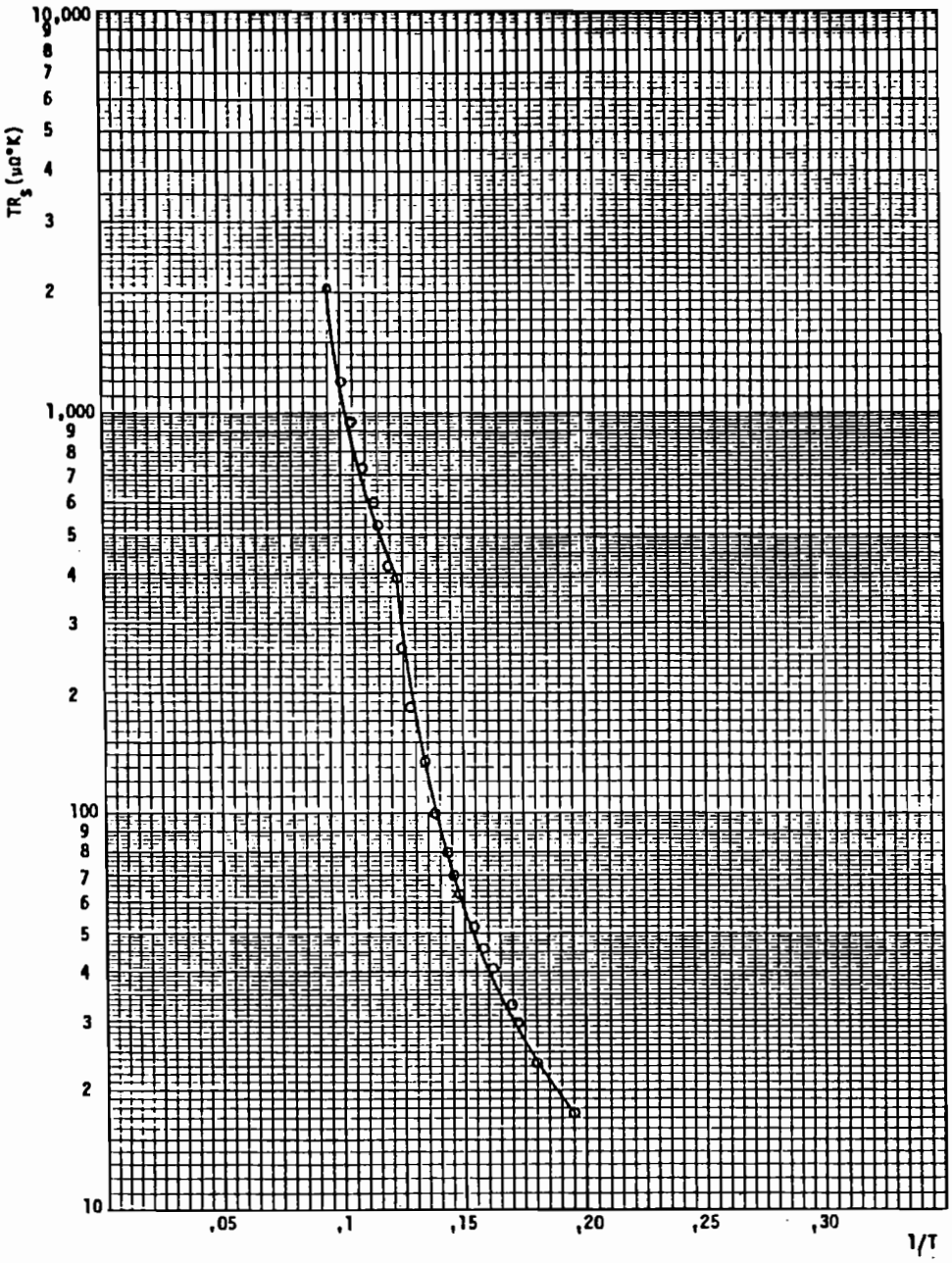

Figure IV-3. TR_S plot of cavity #1WG

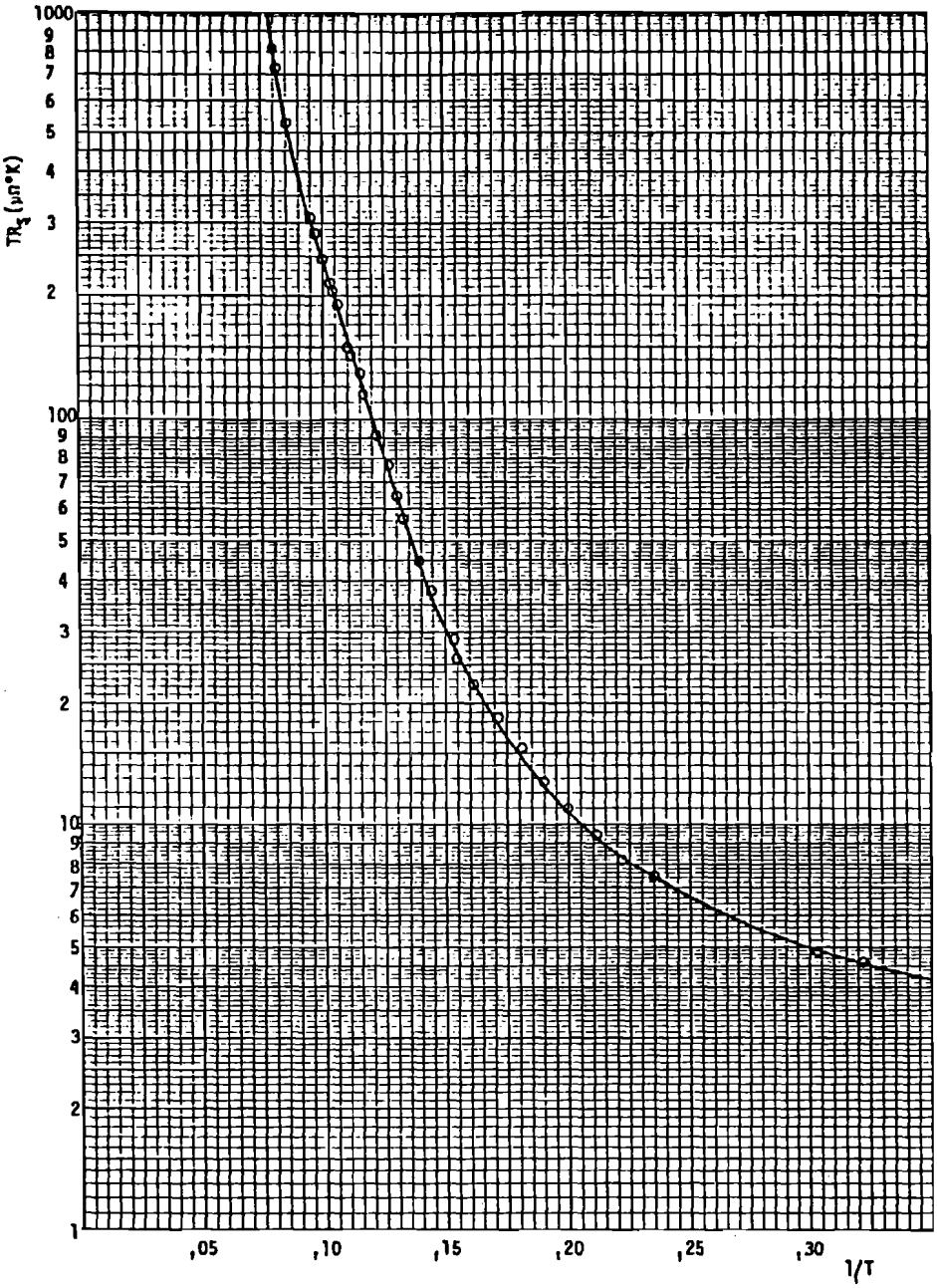

Figure IV-4. TR_S plot of cavity #2WG

Since both cavities were waveguide-coupled, the 8.2° structure cannot be attributed to the Nb belly band as discussed in Chapter III, and must therefore indicate a Nb_3Sn-depleted region in the non-sputtered cavity.

Surface Porosity

Two observations suggested that ionplated cavities might have significant surface porosity, leading to absorption of the methanol used during cavity preparation.

Following the second test of cavity #1WG, the cavity was warmed to room temperature, and kept at high vacuum while two resistance thermometers were attached to the cavity exterior with GE varnish. A hot air gun was used to cure the varnish and warmed the cavity to perhaps 50-70°C for several minutes. The cavity was then cooled and retested, and showed an improvement in Q(4.2°) from 8.6×10^7 to 1.2×10^8. It was thought that degassing of the cavity walls might account for this improvement, and a second test was made with cavity #1SM. Following the fifth test of this cavity, it was warmed to room temperature and immersed in boiling water for 3 hours. The cavity pressure increased from less than 10^{-8} mm to over 10^{-7} mm and decreased slowly as the boiling proceeded. The subsequent retest showed a Q-improvement from 6.1×10^7 to 1.6×10^8.

Annealing

One test was made to determine whether post-reaction

annealing would improve performance. Following the sixth test of cavity #1SM, both cavity halves were annealed 20 hours at 750°C, oxipolished 75V and retested. No improvement was observed.

Summary

The r.f. performance of the ionplated cavities was characterized by Q degradation as field levels were raised. This degradation begins at very low field levels.

Waveguide-coupled cavities show a repetitive breakdown behavior which probably results from field enhancement at the coupling ports. Breakdown fields obtained with these cavities are therefore rather low.

Probe-coupled cavities do not show a distinct breakdown field but are limited to fields of about 5 MV/m by thermal Q degradation. Only slight improvement in Q or breakdown field could be obtained by cooling from 4.2° to 1.5°.

Low field surface resistances below 1 μΩ were achieved at 1.5°, and evidence of surface porosity was found.

3. Vapor-Diffused Strips and Cavities

Production and testing of vapor-diffused cavities followed after completion of the ionplated cavity work. Four cavities, two waveguide-coupled and two probe-coupled, were tested. Preparation details and test results are shown in Tables IV-4 and IV-5.

The firing procedure evolved considerably as work with vapor-diffused cavities proceeded. Results were found to

Table IV-4. Vapor-Diffused Cavity Preparation Details

Cavity No.	Cavity Type	Prev. Nb Perform.		Control of Sn Flux		Reaction Parameters Time	Temp	Comments
#4AWG	WG, solid Nb	$1x10^9$	8.5		None	20 hrs	1000°	Large Sn deposits, rough crystals of Nb_3Sn after Sn
#4BWG	WG, solid Nb	$1x10^9$	8.5		None	20 hrs	1000°	removal. Not anodized before firing.
#6BWG	WG, solid Nb	--	--	11	#68 holes	15 hrs	1050°	Pre-nucleated 5 hrs at 700°
#6SWG	Same	--	--	10	#68 holes	5 hrs	1050°	Pre-nucleated ~30 min at 700° Both halves anodized 100 V before firing Small Sn spots on both halves
#4BSM	Probe coupled sheet metal cups			10	#68 holes	8 hrs	1050°	Anodized before firing Uniform pink Nb_3Sn, no Sn spots. No pre-nucleation
#4ASM	Same			10	#68 holes	8 hrs	1050°	Fired same as 4BSM. Incomplete Nb_3Sn coverage
#4ASM (refired)				10	#68 holes	8 hrs	1050°	Special "gradient" pre-nucleation (see text) Uniform pink Nb_3Sn
#3ASM #3BSM	Probe coupled sheet metal cups			10	#68 holes	10 hrs	1050°	Ion-plated with 0.5 μ Sn before firing. No pre-nucleation period during firing cycle.

Table IV-5. Vapor Diffused Cavity Results

Cavity No.	Pre-test Preparation	R.F. Results Q (4.2°)	Q (<2°)	E_{acc} (4.2°)	E_{acc} (<2°)	T_c (°K)	λ_o (Å)	Comments
#4WG	Oxipolish 2x100 V	$2x10^7$	$2x10^7$	--	--	--	--	
	O.P. 5x100 V	$9x10^7$	$1.2x10^8$	1.3	1.3	--	--	Fast, non-repetitive breakdown
	Mech. polish, O.P. 7x150 V	$<2x10^7$	--	--	--	--	--	Testing terminated
#6WG	O.P. 300 V total	--	--	--	--	--	--	Assembly difficulties. Test aborted
	O.P. 4x75 V	$1.7x10^8$	$>2x10^8$	4.4	--	--	--	±20% accuracy on Q (4.2°)
	Boiled 8 hrs	$1.7x10^8$	--	--	--	18.1°	2640	Magnetic breakdown
	Boiled 8 hrs	$1.7x10^8$	--	--	--	18.1°	2640	No $R_s(T)$ structure at 9.2°
#4SM	O.P. 2x75 V	$2.4x10^8$	$3.6x10^8$	6.0	6.0	--	--	Magnetic breakdown Q (E_{acc} = 6 MV/m = $1.2x10^8$ @ 4.2°K = $2.0x10^8$ @ 2°K
	O.P. 2x75 V	$6.5x10^7$	$1.74x10^8$	∿3.0	4.2	18°	8200	Suspected indium contamination "Heating lump" limits field Unexplained $R_s(T)$ structure at 6.1°
	Ultrasonic clean, O.P., 3x75 V	$9x10^6$	--	--	--	9.2°, 18.1°		Swept T_c measurement shows 9.2°+ 18.1° transitions. Cracks in Nb_3Sn observed after disassembly
#3SM	As fired	$5.8x10^7$	$6.3x10^7$	3.7	3.7	17.0°	2990	Magnetic breakdown
	O.P. 75 V	$2.3x10^8$	$2.7x10^8$	7.1	7.1	17.7°	2640	Magnetic breakdown Q (E_{acc} = 7 MV/m) = $1.2x10^8$
	O.P. 75 V	$4.7x10^7$	--	5.7	--	17.5°	3020	Considerable $R_s(T)$ structure of 9.1° suggests exposed Nb

depend critically upon details such as Sn source construction, position and orientation, substrate anodization, warming rate, and upon the temperature gradients within the furnace. Strip-samples and scrap cavity halves were fired, as required, to test changes in firing procedure.

Exposure of the Nb substrate to saturated Sn vapor was found to result in condensation of appreciable quantities of liquid Sn, resulting in shiny Sn deposits after cooling. The flux of Sn to the substrate therefore had to be reduced using the Nb foil screen described in Chapter III.

It was also necessary to provide for nucleation of a complete Nb_3Sn layer at the start of the firing cycle. Unless some nucleation-enhancing technique is employed, the reduced flux of Sn vapor necessary to prevent Sn condensation during the later stages of the firing cycle will result in incomplete coverage by the Nb_3Sn layer.

The pre-anodization technique advocated by the Siemens group[2] and described in Chapter III was used for all but the first vapor-diffused cavity. According to the Siemens group, the presence of an anodic oxide film on the Nb substrate prevents reaction of the substrate with condensing Sn vapor during the early stages of the firing cycle and allows a continuous Sn film to accumulate before diffusion into the Nb begins. As substrate temperature rises to about 700°C, the anodic oxide diffuses into the substrate, allowing

reaction to begin.

Even with the anodic oxide layer, it was necessary to modify the firing temperature cycle to include a "nucleation period" during warmup. Initially, this consisted of warming the cavity to 600-700° and maintaining this temperature for several hours before raising the temperature on up to 1000°, or, alternatively, slowly warming the cavity from room temperature to reaction temperature, thus allowing Sn to cover the anodically-protected cavity during the slow warmup. Since these cavities had no ionplated Sn, the poor results obtained with slow-fired ionplated strip-samples did not recur.

The most successful nucleation temperature cycle was discovered accidentally. During one furnace run the three upper heating elements of the furnace failed, leaving only the three lower elements and producing a thermal gradient across the Sn-source/substrate region. The Sn source was therefore considerably hotter than normal during the start of the temperature cycle, producing sufficient Sn to completely cover the cavity, while the substrate was cooler than normal, retarding dissolution of the anodic oxide layer. The result was a uniformly nucleated Nb_3Sn layer. This "gradient technique" was therefore used on several subsequent firings; the cavity was warmed to 800-900° using only the bottom heaters, then the upper heaters were energized

and cavity temperature was stabilized at 1050°C.

The final nucleation technique to be tried consisted of ionplating cavity #3SM with 0.5 μm of Sn and then firing, using the Sn source developed for cavity #4SM, but without anodization or any "nucleation" period during warmup.

Discussion of Vapor-Diffused Cavity Results

Cavity Appearance: Vapor-diffused cavities had, in general, smooth specular surface finishes as shown in Figure 5. The uniformity of the surface was broken in places by various defects. The most common surface defects, especially with the earlier cavities, were Sn deposits. These ranged in size from sub-millimeter (Figure 6) to large deposits 2-3 mm thick and several cm across.

Figure 7 shows the cavity (#4WG) which had the large deposits mentioned. The Sn, which was removed chemically, covered the entire circular area visible in the lower half of the cavity, and covered half of the rectangular cup region. The orientation of the cavity during firing was such that the Sn condensation occurred on the cavity region which was nearest the mouth of the furnace, and therefore was probably slightly cooler than the cavity regions on which condensation did not occur. Removal of the Sn revealed a colony of coarse Nb_3Sn crystals along the lower edge of the cup.

By reducing the Sn flux to the cavity surface, the size

Figure 5. Typical vapor diffused surface texture

Figure 6. Small Sn spots

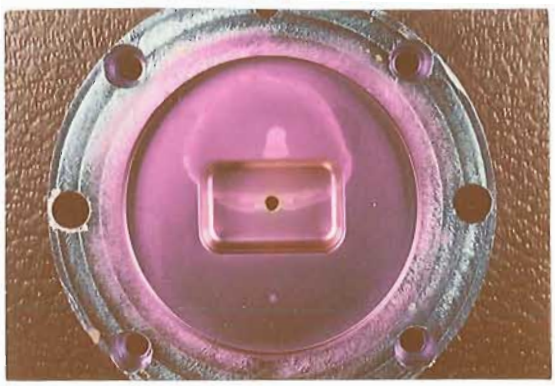

Figure 7. Remains of large Sn pool

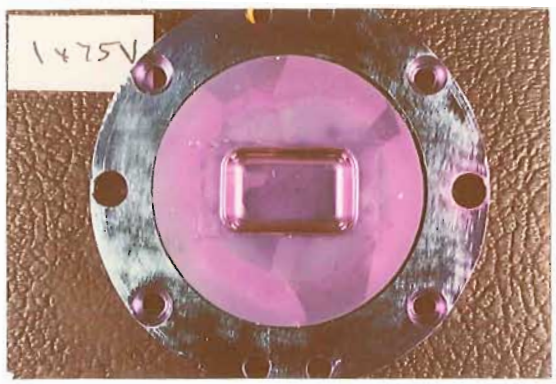

Figure 8. Cavity #4SM illustrating incomplete nucleation

Figures IV-5 through IV-8

and number of Sn deposits was reduced. Cavity #6WG had a number of very small Sn spots, and cavity #4SM, along with several scrap cavity halves which were fired with a reduced Sn vapor flux, showed no Sn deposits.

Considerable difficulty was experienced in trying to achieve complete coverage of cavity #4SM with Nb_3Sn. Figure 8 shows one half of #4SM after only one 75V oxipolishing cycle. A considerable portion of the surface shows the blue color of unreacted Nb, while other regions suggest a relatively thick Nb_3Sn layer. This cavity half, after refiring using the thermal gradient nucleation technique, performed very well.

Cavity #3SM, which was pre-nucleated with 0.5 μm of ionplated Sn, is shown in Figure 9. The difference between the two cavity halves may probably be attributed to different plated Sn thicknesses, 3ASM having had slightly more Sn and showing some agglomeration, while 3BSM shows no such agglomeration. The patterns visible on 3BSM are those of the underlying Nb grain boundaries.

R.F. Performance

R.F. performance of the vapor-diffused cavities was considerably better than that of the ionplated cavities, particularly with respect to Q values at high field. All of the vapor-diffused cavities could be run CW at their maximum field levels and were not restricted to pulsed

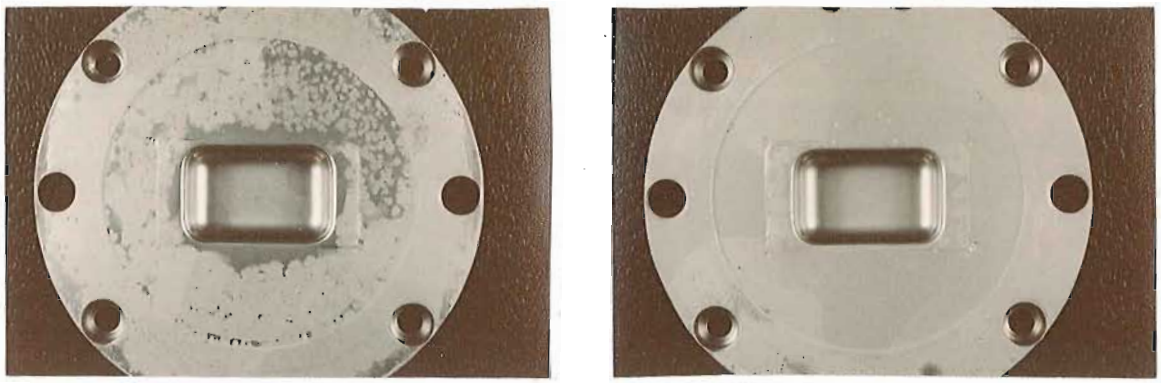

(a) (b)

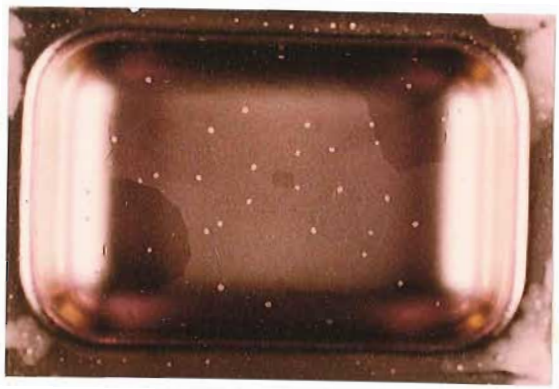

(c)

Figure 9. "Pre-nucleated" cavity #3SM

Figure IV-9

operation, as was the case with the ionplated cavities. Q(E) for both vapor-diffused and ionplated cavities is shown in Figure 10. The uncertainties in the low-field Q_o measurements of cavity #6WG resulted from overcoupling ($\beta_1 \sim 10$) at these field levels.

Accelerating fields were limited by a fast, non-repetitive breakdown, suggesting a magnetic or magneto-thermal breakdown mechanism. The lower breakdown field of the waveguide-coupled cavity #6WG is probably due at least in part to field enhancement at the coupling holes. Previous work with Nb cavities at Cornell has shown that the waveguide coupled "muffin-tin" cavities used here typically achieve breakdown fields only about 60% as large as the values obtainable with similar probe-coupled cavities. This difference is due to the non-optimum placement of the coupling holes.

Cavity #4WG showed a very low breakdown field which was attributed to field enhancement at the sharp edges of Nb_3Sn crystal clusters which were present inside the cup.

$R_s(T)$ measurements of the "restricted Sn vapor" cavities #3SM and #4SM suggested the presence of exposed Nb after only a few oxipolishing cycles. This, together with the rapid deterioration in Q(4.2°) and increase in λ_o after oxipolishing, suggests that the Nb_3Sn layer was quite thin. This fact was not appreciated during the testing of cavities #6WG and

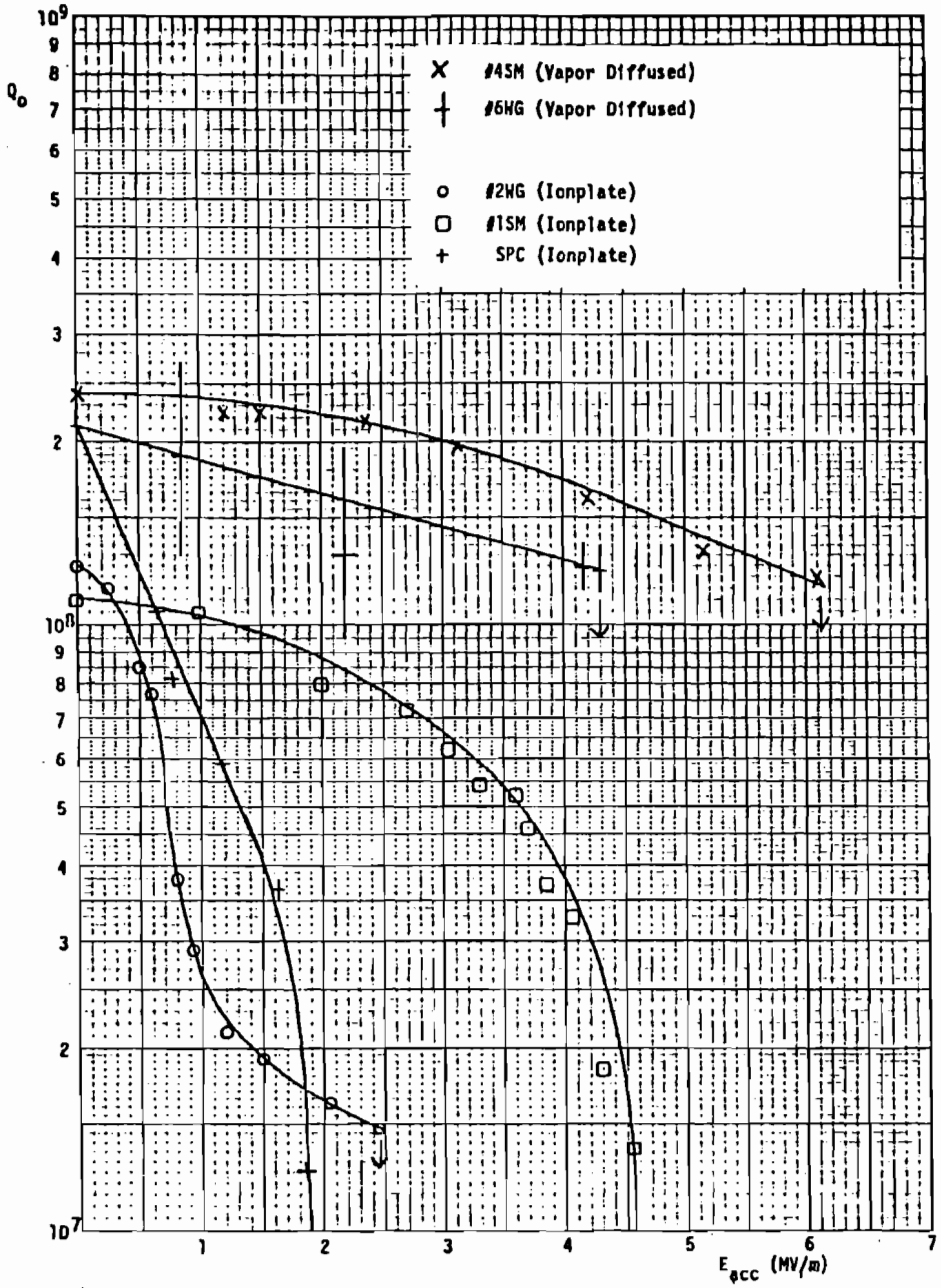

Figure IV-10. Q_o vs. accelerating field for vapor diffused and ionplated cavities

#4SM, both of which had quite a bit of material removed by oxipolishing before their first r.f. tests.

The very poor performance of cavity #4SM during its last test is believed to be partially attributable to cracking in the Nb_3Sn layer. During UHV degassing of this Nb cavity, one cavity half was lying over a flake of tungsten, and during the 1900°C firing, a terraced arrangement of Nb grains was formed on the cavity interior surface. Vigorous ultrasonic cleaning to remove indium flakes following the second r.f. test formed a network of hairline cracks, as shown in Figure 11, resulting in high r.f. losses. The observed Q of 9×10^6 cannot be explained solely by exposed Nb, since Nb cavities have Q-values greater than this at 4.2°K.

The presence of surface porosity was investigated with cavity #6WG. Boiling and retesting produced no improvement in Q, indicating less porosity than was observed with ionplated cavities.

Comparison of Ionplated and Vapor-Diffused Cavities

The r.f. performance of the vapor-diffused cavities was considerably better than that of the ionplated cavities, particularly with respect to high-field Q-values. This superiority is especially significant in light of the fact that the vapor-diffusion technique was not developed to its fullest potential due to time limitations. Further development of the "gradient" nucleation technique, with r.f.

Figure 11. Suspected cracking in cavity #4SM

Figure IV-11

testing performed before removing too much Nb_3Sn by oxi-polishing, would almost certainly result in better performance than was achieved with cavity #4SM. Similarly, better control of the ionplated Sn thickness on cavity #3SM would probably prevent the observed agglomeration and result in improved performance. The ionplated cavities showed no corresponding potential for improvement.

Results of Microscopic Examination

Microscopic examination of Nb_3Sn samples was done with an emphasis on correlating surface morphology with r.f. performance and reaction conditions.

Ionplated Surfaces

"Plain" ionplated surfaces, as discussed earlier, show an agglomeration of Sn into droplets during firing. If the firing time is sufficiently long, the excess Sn in these droplets evaporates. The morphology of these spots, however, remains quite different from that of the interspot regions which had during reaction a lower concentration of Sn.

Figures 12-14 shows the surface of #1WG cavity in a spot region, an interspot region, and a spot-interspot boundary, respectively. The difference in surface texture is striking, the spot region showing crystals up to about 10 μm in size, while the interspot region is much smoother. The spot-interspot boundary shows a line of particularly large crystals just inside the spot region. Picture #15

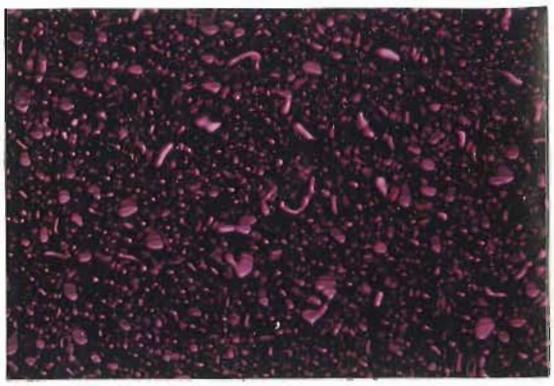

Figure 12. Spot region

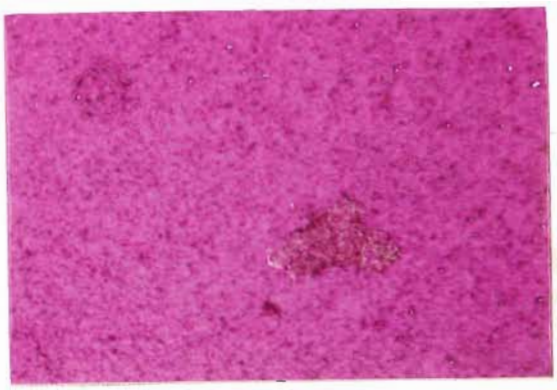

Figure 13. Interspot region

Figures IV-12 through IV-17

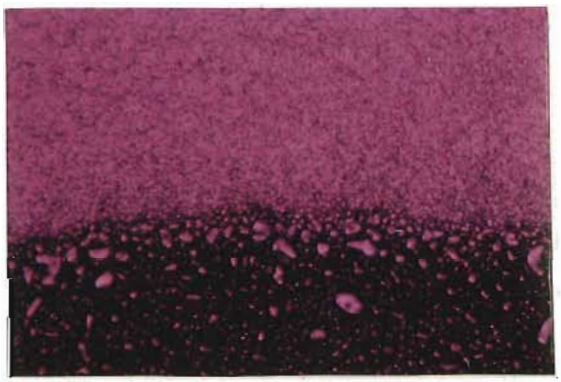

Figure 14. Spot-interspot boundary

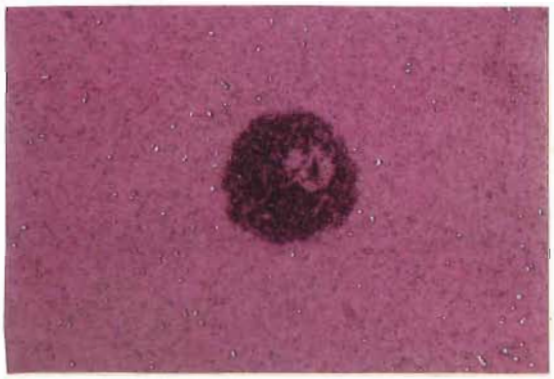

Figure 15. Small spot

Figure 16. Cavity #2WG

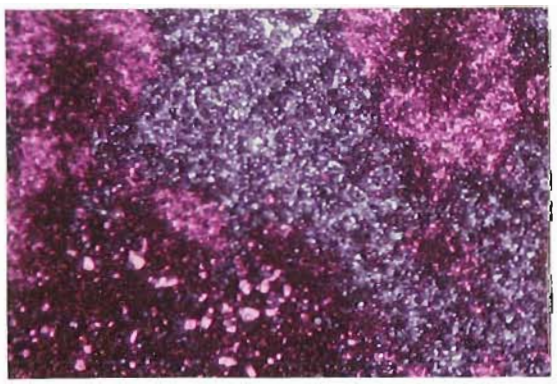

Figure 17. #2BWG after 4-5 μm of oxipolishing

shows a small spot surrounded by a smoother interspot region. This sample had been oxipolished to a considerable depth, and the interspot region shows a number of blue spots indicating pure Nb. The rougher spot region shows very few Nb incursions, suggesting a deeper Nb_3Sn layer.

The "special" ionplating process, in which a thin sputtered Nb coating is added to prevent Sn agglomeration, also produces rough surfaces. Cavity #2WG, produced by this process, shows uniform coloring over the entire cavity surface (Figure 16). Only at a depth of about 4-5 μm does multiphase structure appear, as shown in picture 17. Several very large grains can be seen, suggesting a growth process similar to that of the "plain" ionplated surfaces.

Vapor-Diffused Surfaces

Typical vapor-diffused surfaces are shown in Figures 18 and 19. Note that the crystal size is much smaller and the surface smoother than was the case with the ionplated surfaces. The sample shown here was produced with the "restricted Sn vapor" technique used to produce #4SM cavity. Figure 20 shows cavity 6BWG, which was produced using slightly more Sn vapor and shows a grain structure slightly coarser than #4SM but still much finer than the ionplated surfaces.

#6WG also had evidence of a few condensed Sn droplets, and Figure 21 shows a larger crystal size in this region,

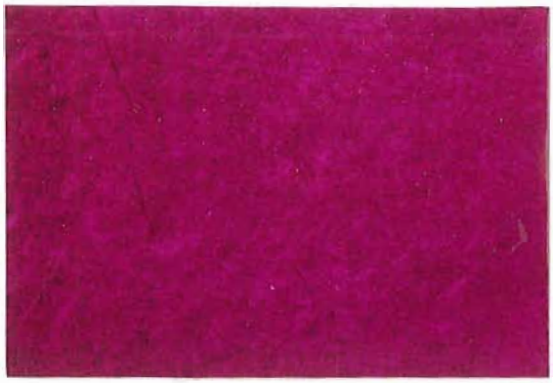

Figure 18. Typical vapor-diffused surface

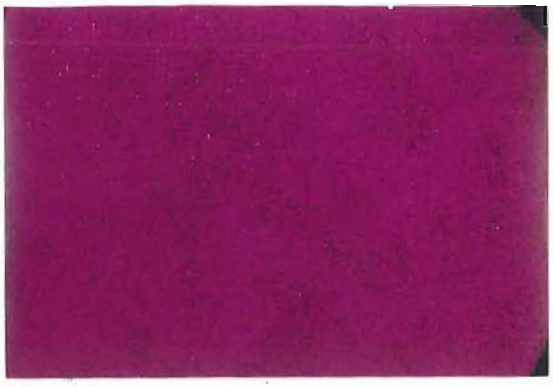

Figure 19. Typical vapor-diffused surface

Figures IV-18 through IV-23

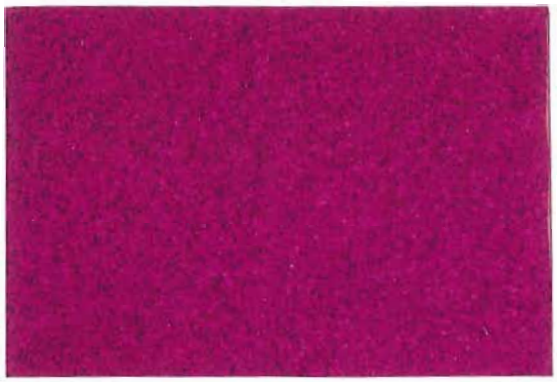

Figure 20. #6WG

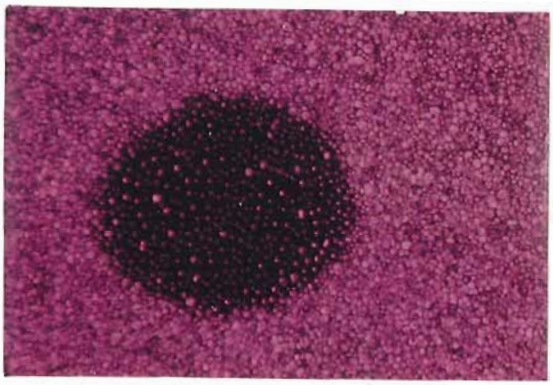

Figure 21. #6WG

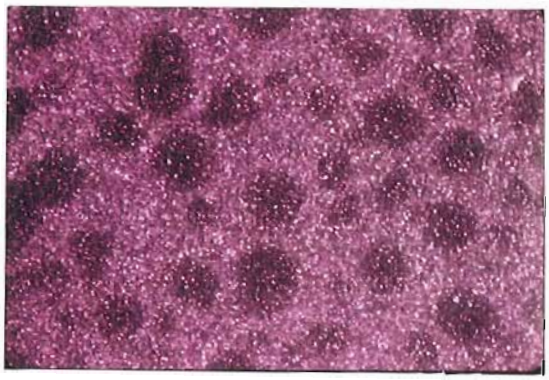

Figure 22. #3SM

Figure 23. #3SM

with a correspondingly coarser surface finish.

Cavity #3SM, which was given a thin ionplated layer and grown in restricted Sn vapor, is an intermediate case (Figures 22, 23). A grain structure slightly coarser than that of #6BWG is evident, as is some tendency towards Sn agglomeration.

Nb Inclusions

Vapor-diffused and ionplated surfaces also differed in the number and type of Nb inclusions observed, and in the depth at which these inclusions were found. These Nb inclusions were easily recognized by their blue color.

Ionplated samples show Nb inclusions only after several μm of oxipolishing, and the inclusions have no particular form (Figures 24, 25). The size and shape of the inclusions are similar to those of the surrounding Nb_3Sn grains.

Vapor-diffused samples often show Nb inclusions closer to the surface, and these inclusions often have elaborate and interesting shapes. The structure in Figure 26 is from cavity half "4BSM" (restricted Sn vapor) after 2.5 μm of oxipolishing. The blue Nb region is surrounded by a Nb_3Sn region of smoother texture than the surrounding Nb_3Sn. A number of parallel pink stripes cross through the Nb region indicating that a preferred direction existed during the diffusion process. A similar structure from the same cavity is shown in Figure 27. Yellow inclusions, indicating

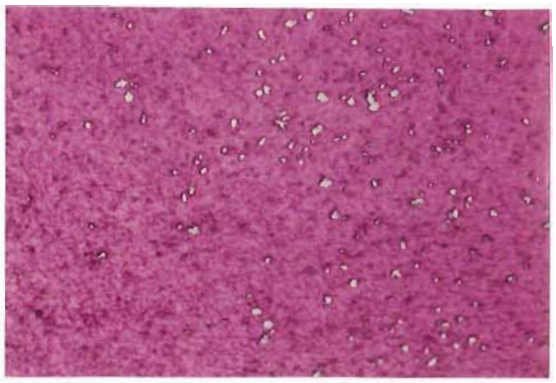

Figure 24. Nb inclusions in ion-plated sample

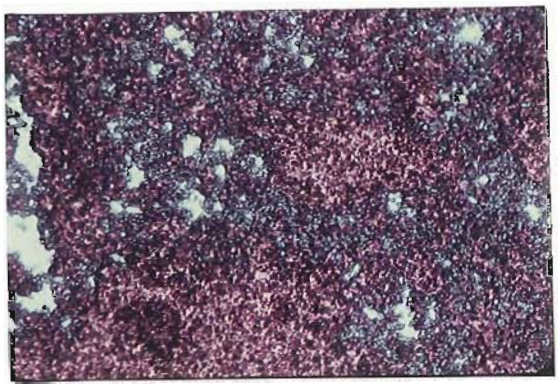

Figure 25. Nb inclusions in ion-plated sample

Figures IV-24 through IV-29

Figure 26. Nb inclusion in vapor-diffused sample

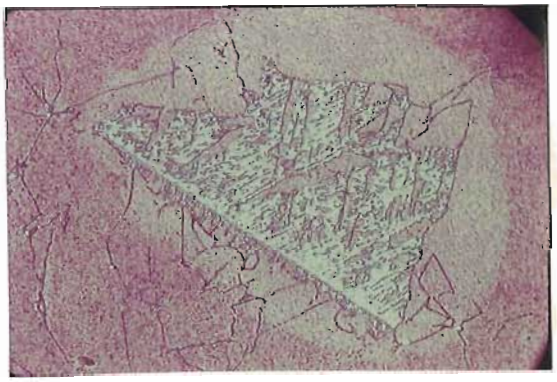

Figure 27. Nb inclusion in vapor-diffused sample

Figure 28. Nb inclusion from vapor diffused sample

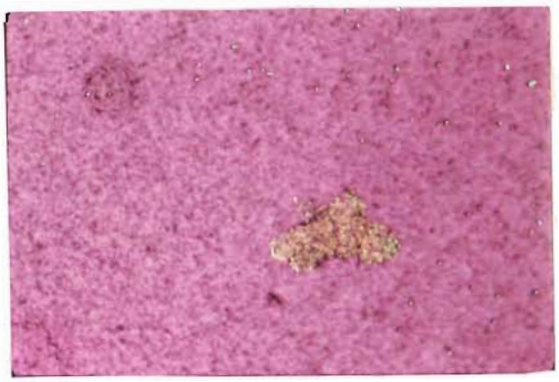

Figure 29. Sn inclusion from ion-plated interspot region

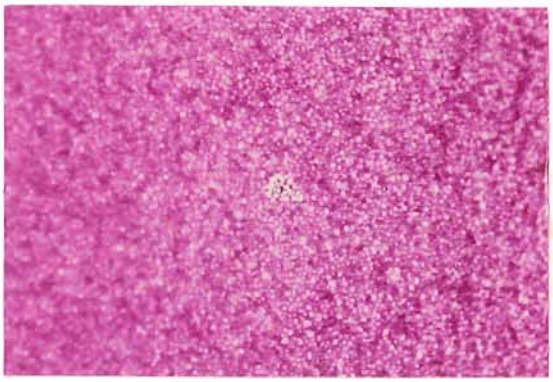

Figure 30. Sn inclusion in cavity #6WG

Figure 31. Sn inclusions in cavity #4SM

Figures IV-30 through IV-35

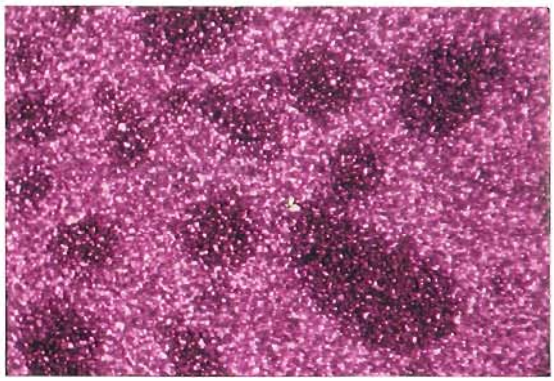

Figure 32. Small Sn inclusion in cavity #3SM

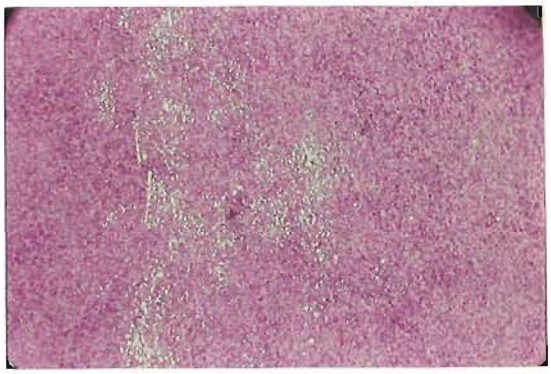

Figure 33. S21 oxipolished 0.2 μm

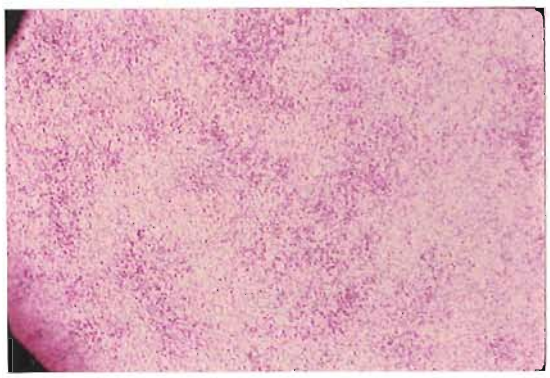

Figure 34. S21 oxipolished 1.5 μm

Figure 35. Multiphase inclusion

pre-nucleation). These yellow inclusions are most likely Sn or an Sn-rich solid solution. All of the samples above had been oxipolished to a depth of at least 1-2 μm.

Other, more complicated inclusions were observed in some of the vapor-diffused samples. The most interesting sample in this respect is S21, a flat strip reacted 21 hours under conditions identical to those which produced cavity #4SM. As will be discussed in the next chapter, diffusion reaction under these conditions for reaction times longer than about 10 hours is expected to result in a slight excess of Sn near the surface. Some evidence to support this was obtained from S21. Figure 33 shows a piece of S21 after 0.2 μm of anodization, with many yellow inclusions present. Figure 34 shows another piece of S21 after 1.5 μm of oxipolishing. No yellow inclusions are present, and examination of the entire surface of S21 before and after the additional oxipolishing showed a much smaller number of yellow inclusions at the greater depth.

Another inclusion observed in S21 is shown in Figure 35. The background is Nb_3Sn, which anodizes blue with the technique used for this sample. The orange and brown regions are probably Nb_6Sn_5 and $NbSn_2$ respectively.

Nucleation of Vapor-Diffused Layers

The problems encountered with incomplete nucleation of vapor-diffused surfaces were discussed in the last section.

It was also noted that cavity #3SM, while yielding very good r.f. performance, deteriorated rapidly after only 1 μm or less of oxipolishing, even though the average Nb_3Sn thickness was much greater than this.

Examination of the surface of cavity #4SM does in fact reveal thin spots in the Nb_3Sn coating and suggests a link between these thin spots and the grain boundary network of the underlying Nb.

The first firing of cavity half #4ASM resulted in incomplete coverage with Nb_3Sn, and it was observed that the Nb grain boundaries were often the dividing lines between nucleated and unnucleated regions. Although refinement of the firing procedure yielded complete coverage of the cavity with Nb_3Sn, the thickness of the Nb_3Sn layer still varied across the cavity, and the Nb grain boundaries still had a marked effect on Nb_3Sn distribution.

Figures 36-38 show cavity half #4ASM after a total of 1.8 μm of oxipolishing. Distinct color and texture changes occur at Nb grain boundaries. Figure 39 shows a much smaller region of #4ASM after 3.7 μm of oxipolishing. The "V" shaped line is an Nb grain boundary and clearly divides the upper, predominantly blue Nb region from the lower pink Nb_3Sn region. The blue "cracks" in the Nb_3Sn region were also observed elsewhere on #4ASM at this depth.

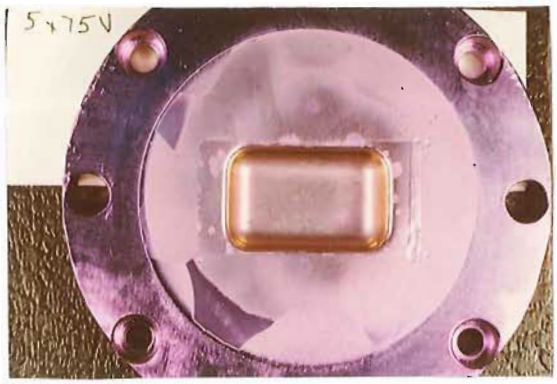

Figure 36. Cavity #4SM

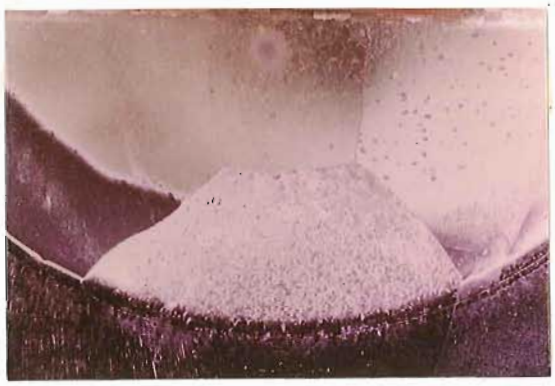

Figure 37. Cavity #4SM

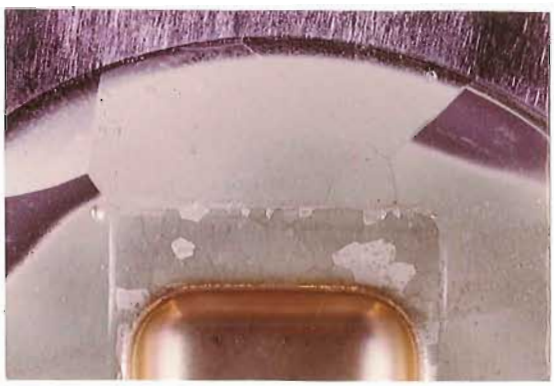

Figure 38. Cavity #4SM

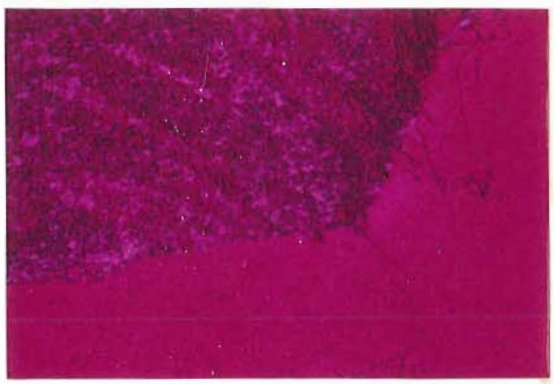

Figure 39. Detail of cavity #4SM

Figures IV-36 through IV-39

Sn Concentration Profiles

Sn concentration-versus-depth profiles were obtained using Secondary Ion Mass Spectroscopy (SIMS) as described in Chapter III.

The first sample to be SIMS analyzed was 3-4, an ion-plated sample strip which was fired 83 minutes at 1150°C. Two of the resulting "leopard spots" were analyzed, and one of the smoother interspot regions was analyzed as well.

The two spot regions (Figures 40 and 41) show very similar profiles, with Sn concentration decreasing almost linearly to a depth of about 5 μm. Within about 0.5 μm of the surface, the Sn concentrations rise suddenly to a level near the surface which is approximately double the concentration at the depth where the linear region begins.

The interspot region shows a distinctly different shape (Figure 42). The first 0.5 μm shows a steep, curving contour similar to that of the spot regions. Between 0.5 μ and 1.8 μ, however, a slightly sloping linear plateau is observed, followed by a relatively sharp "knee" and a diffusion "tail" which extends to a depth of about 3.5 μm. This plot greatly resembles the results of Cu-Pd diffusion studies[3] in which the flat plateau region is shown to correspond to the intermetallic phase CuPd, the surface region corresponds to pure diffusant material (Cu) and the knee marks the CuPd-Pd phase boundary. This suggests that the

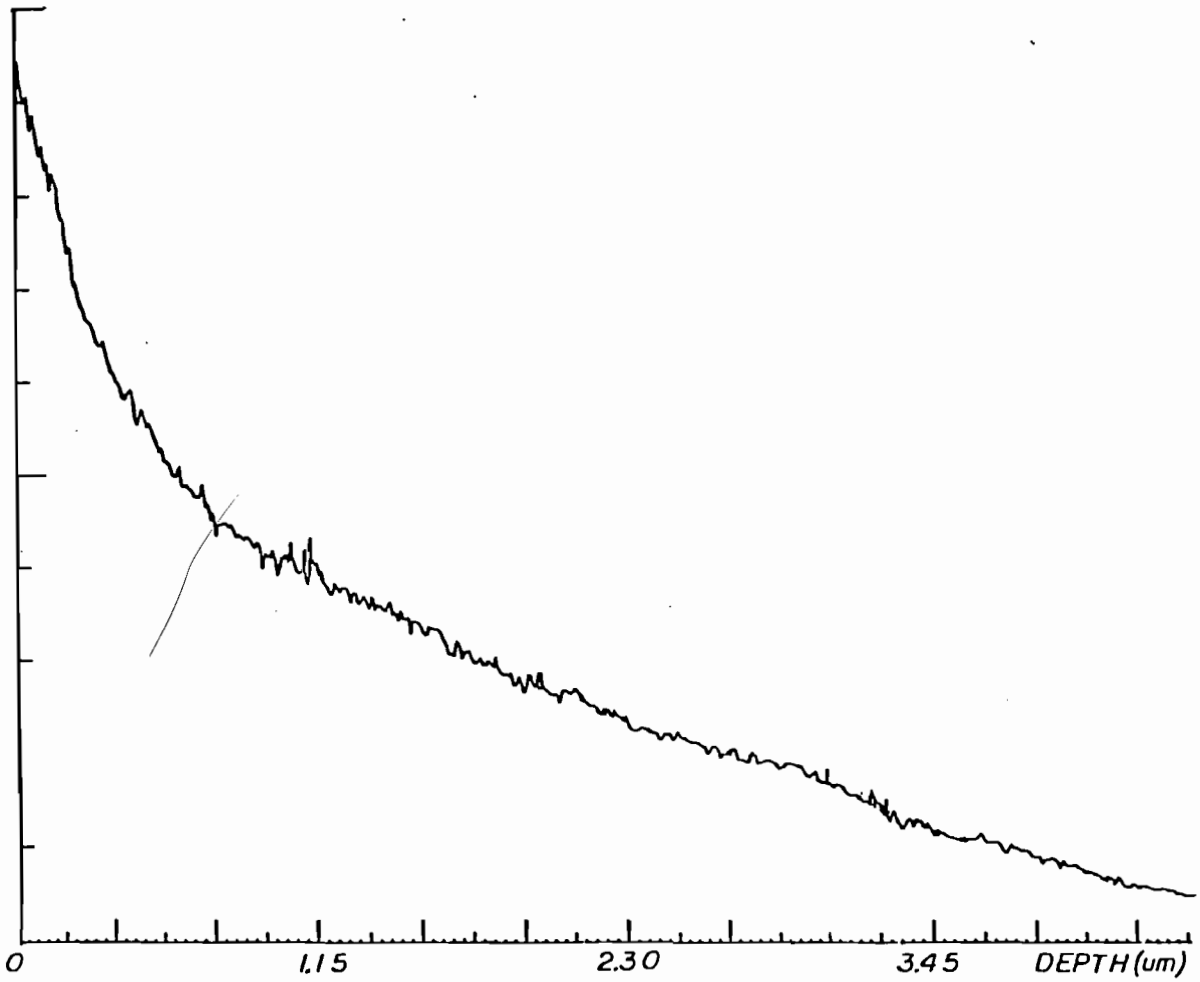

Figure IV-40. Sample 3-4: spot region

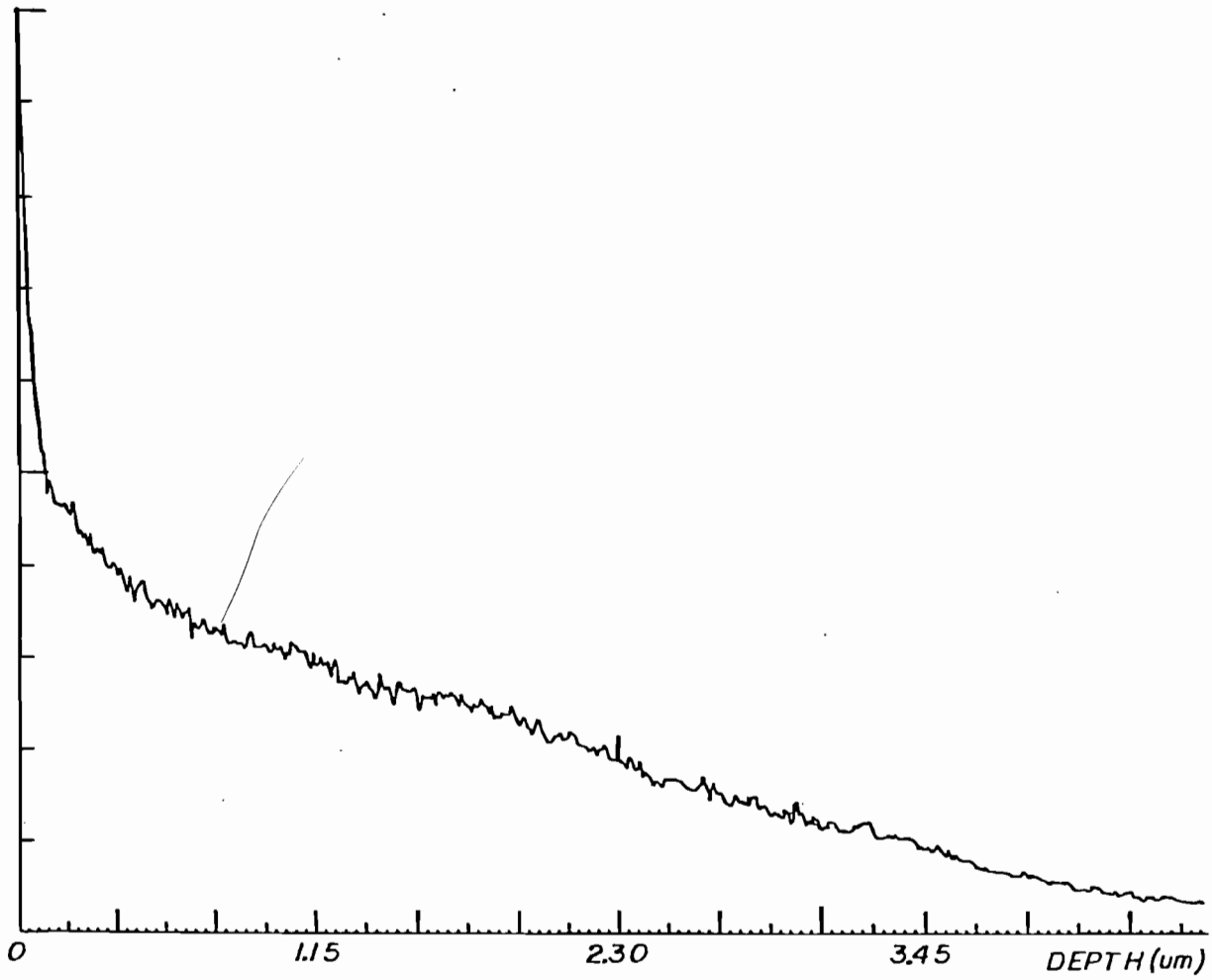

Figure IV-41. Sample 3-4: spot region

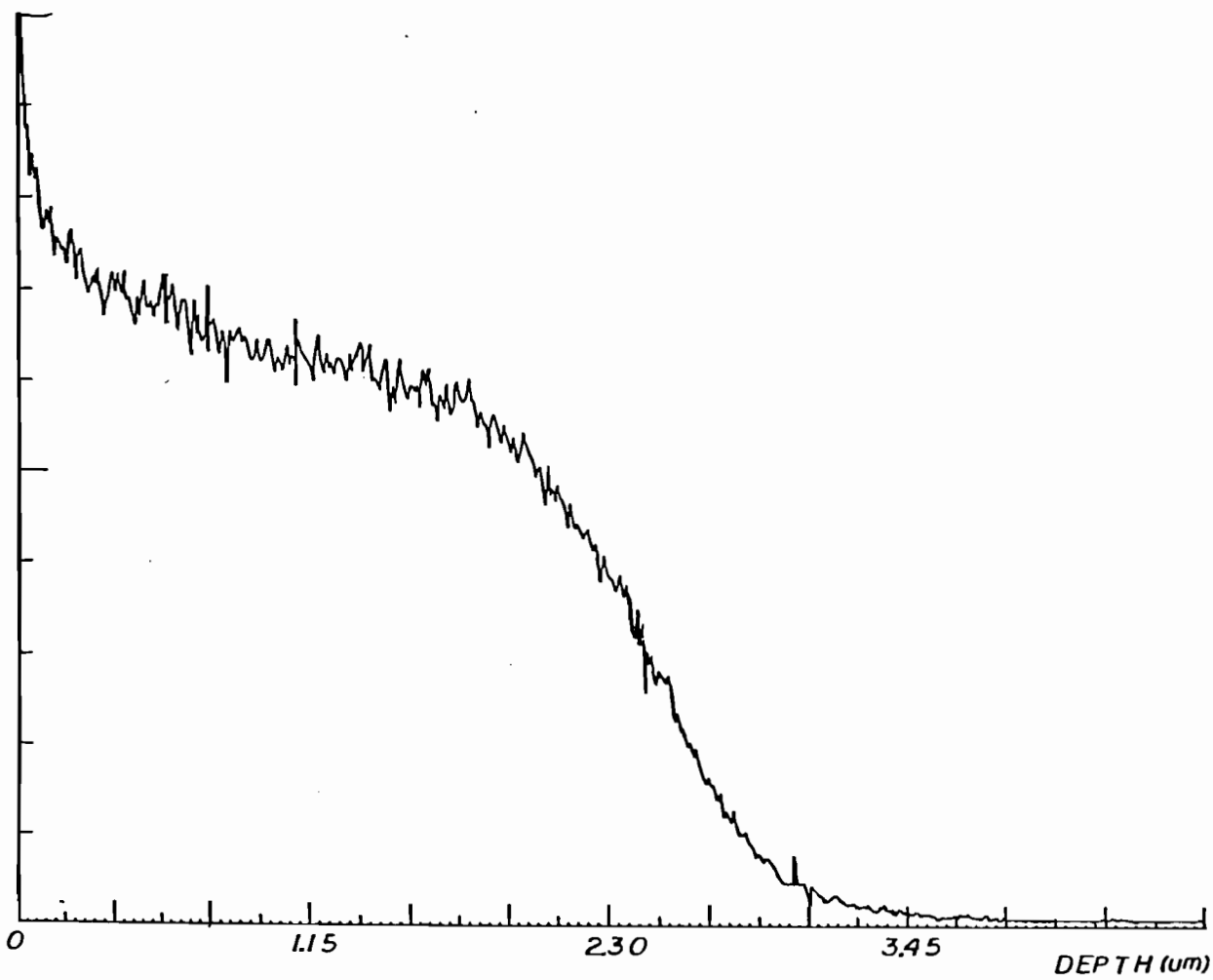

Figure IV-42. Sample 3-4; interspot region

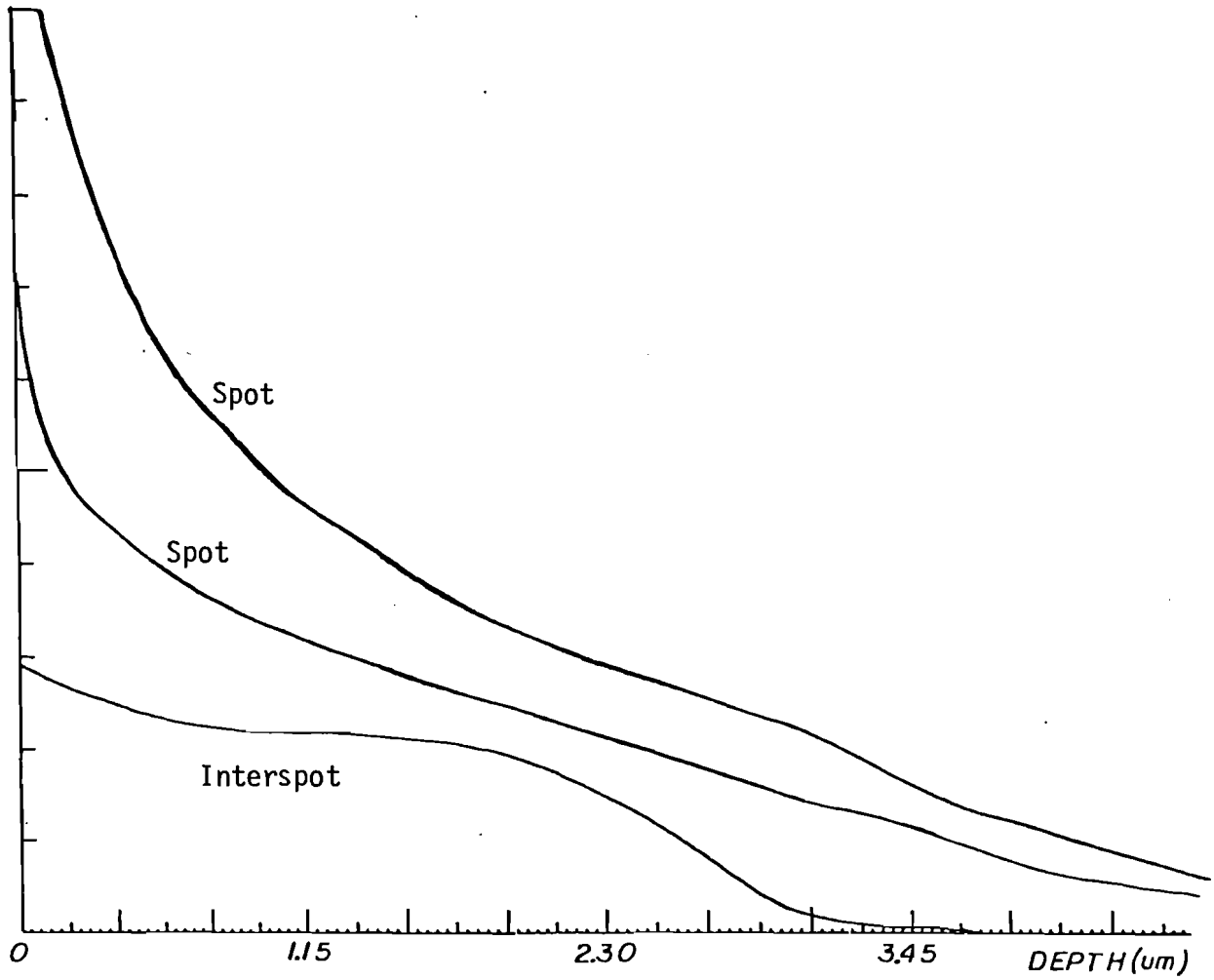

Figure IV-43. Sample 3-4: composite plot of spot and interspot regions

plateaus in our Sn concentration profiles correspond to the A15 phase Nb_3Sn. This interpretation is supported by two T_c versus depth measurements in which samples were repeatedly oxipolished and tested for transition temperature. In both cases T_c changed from about 18° to about 9° in the vicinity of the knee.

Since the Sn count rates in the two spot regions were higher than the rates in the interspot region, it seems likely that the Sn concentration is greater in the spot regions. This cannot be proven from SIMS data alone, however, since the coarser microstructure of the spot regions might result in a higher ion yield. A reasonable correction for such microstructural effects can be made by scaling the three plots so that the Nb count rates are the same, and Figure 43 shows the plots scaled in this manner. The rescaled plots show Sn concentrations in the spot regions which are higher, at any given depth, than the corresponding concentration in the interspot region, even after the differences in microstructure have been compensated for.

We consider next the profiles of two different strips which were ionplated with Sn, sputtered with 1000Å of Nb, and fired. The first sample, known for historical reasons as the "Addis" sample, was fired 120 minutes at 1050° and shows a relatively flat plateau out to approximately 1.7 μm, and then declines rather steadily, with a total depth of

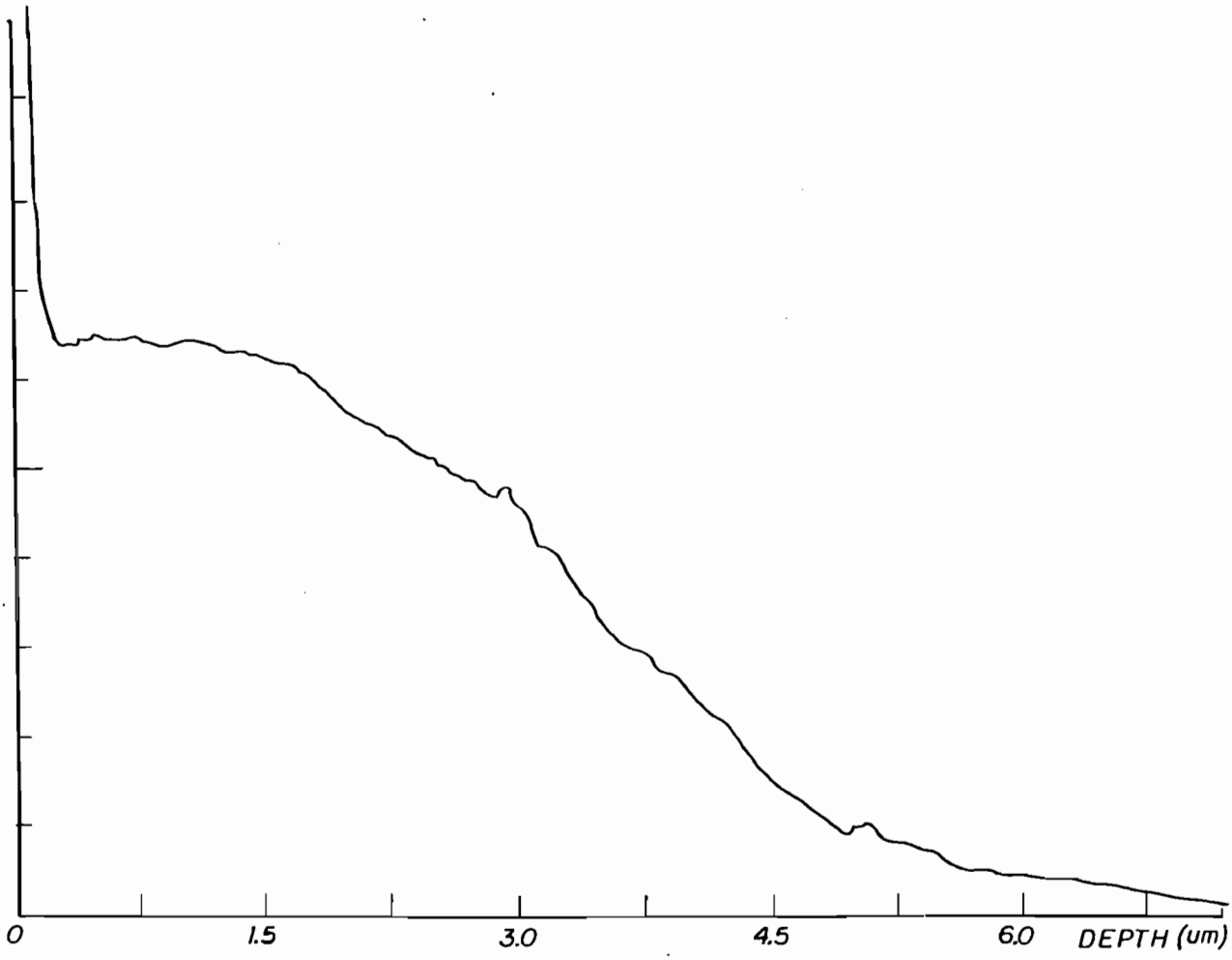

Figure IV-44. "Addis" sample with sputtered Nb overlayer

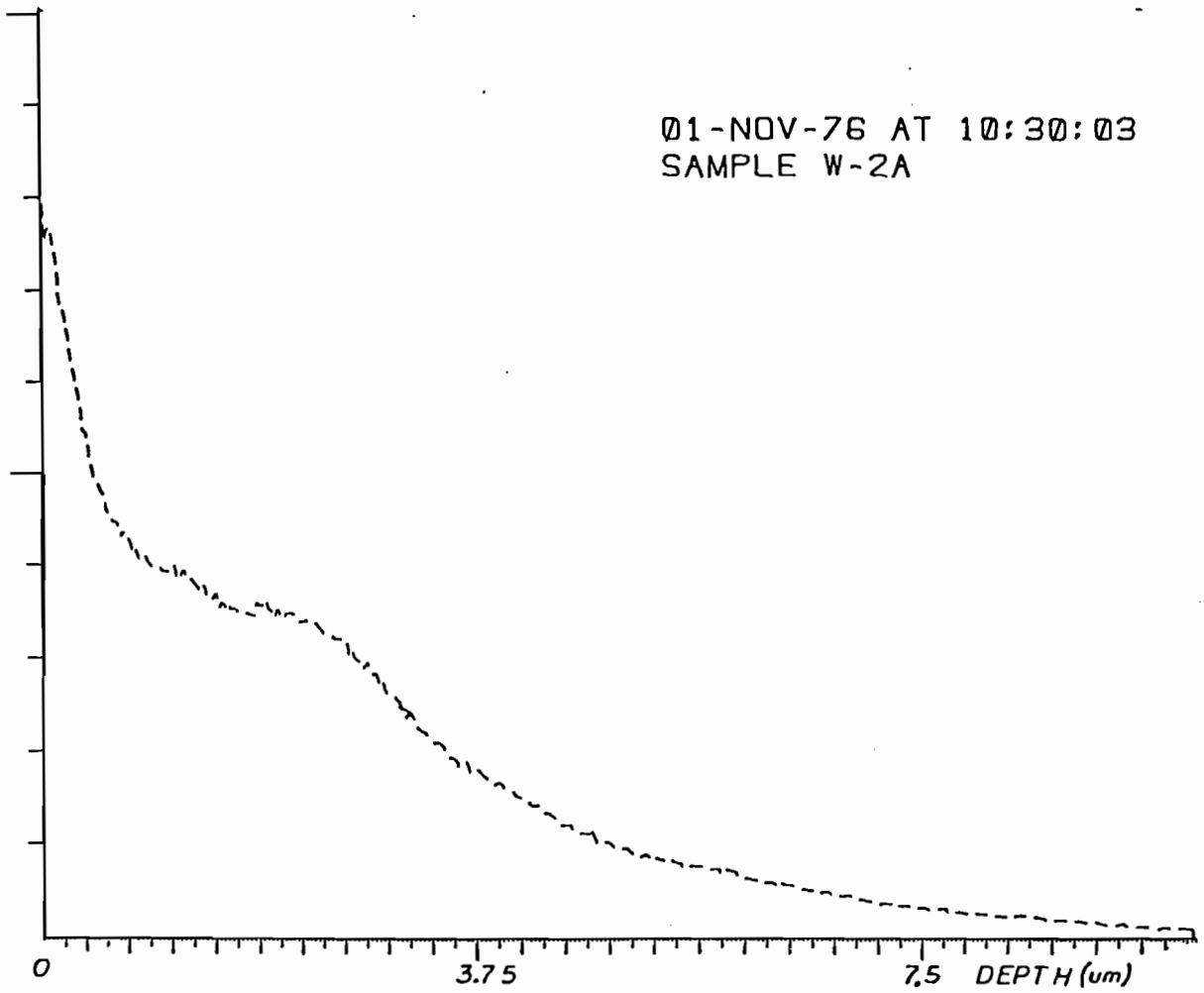

Figure IV-45. W-2A sample with sputtered Nb overlayer

perhaps 5 μm (Figure 44). The second sample, W2A (Figure 45), was fired 3 hours at 1050°C and shows a similar profile. Some difficulty was encountered measuring the sputtered depth of W2A due to the rough surface finish, and the depth calibration shown is taken from another sample run during the same session.

The shape of these two profiles is intermediate between the spot and interspot profiles of 3-2. This is perhaps to be expected, since the sputtered Nb resulted in an even distribution of Sn over the substrate, with a surface concentration less than that of the leopard spots but more than that of the tin-depleted interspot regions. Both profiles show plateaus, but the diffusion tails extending from the Nb-Nb_3Sn phase boundary into the underlying Nb are considerably longer than that of the "interspot" profile, and appear to be longer than the plateaus themselves.

Vapor-Diffused Profiles

The next series of profiles (Figures 46-49) show a set of strip-samples S3b, S6, S10 and S21, which were produced under conditions essentially identical to those which produced cavity #4SM. These strips were used to measure the Nb_3Sn growth rate and are discussed further in the next section. Firing times for these samples were 3, 6, 10 and 21 hours, respectively. Although the 3-hour sample is apparently just beginning to form a continuous Nb_3Sn layer,

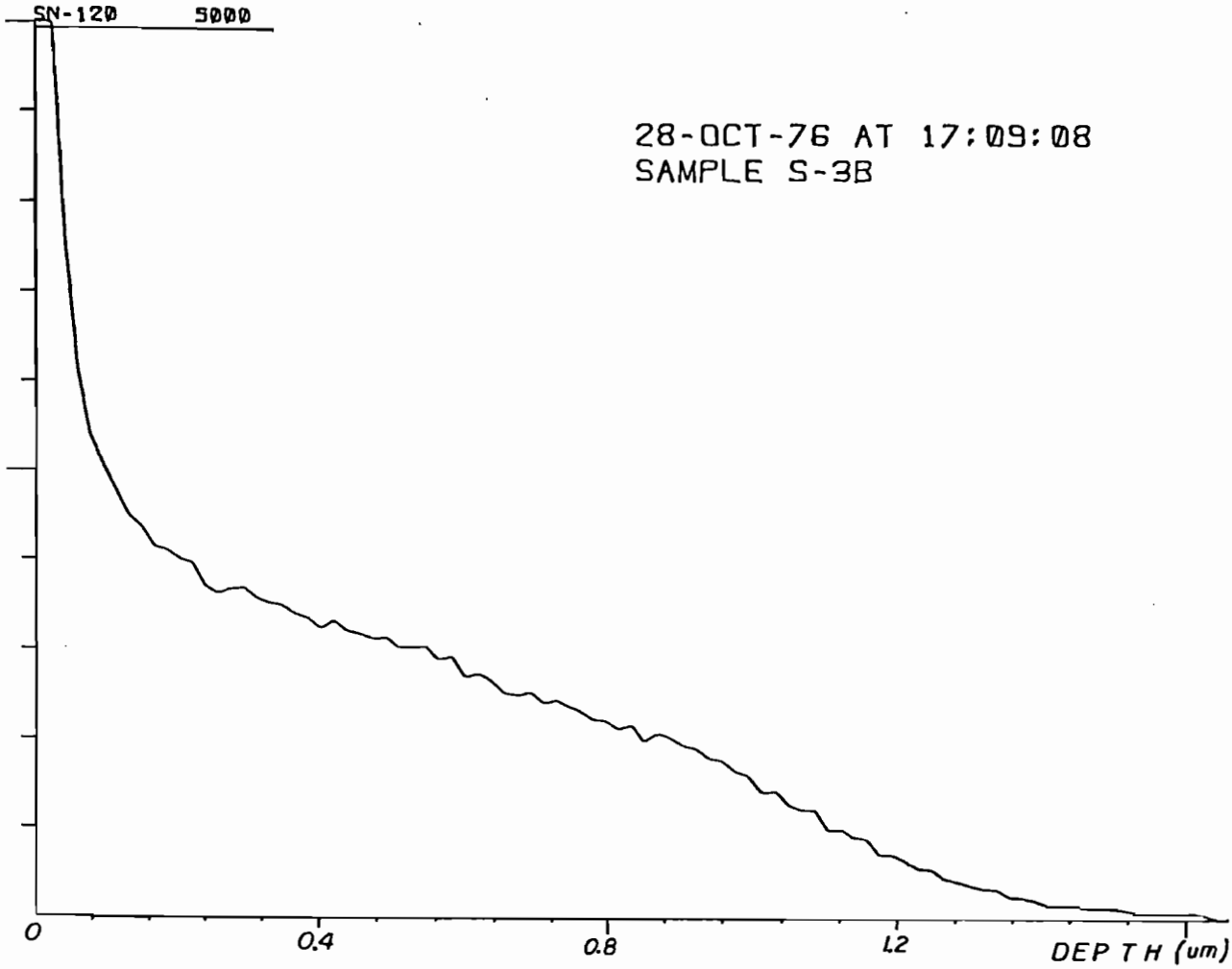

Figure IV-46. Sample S-3B

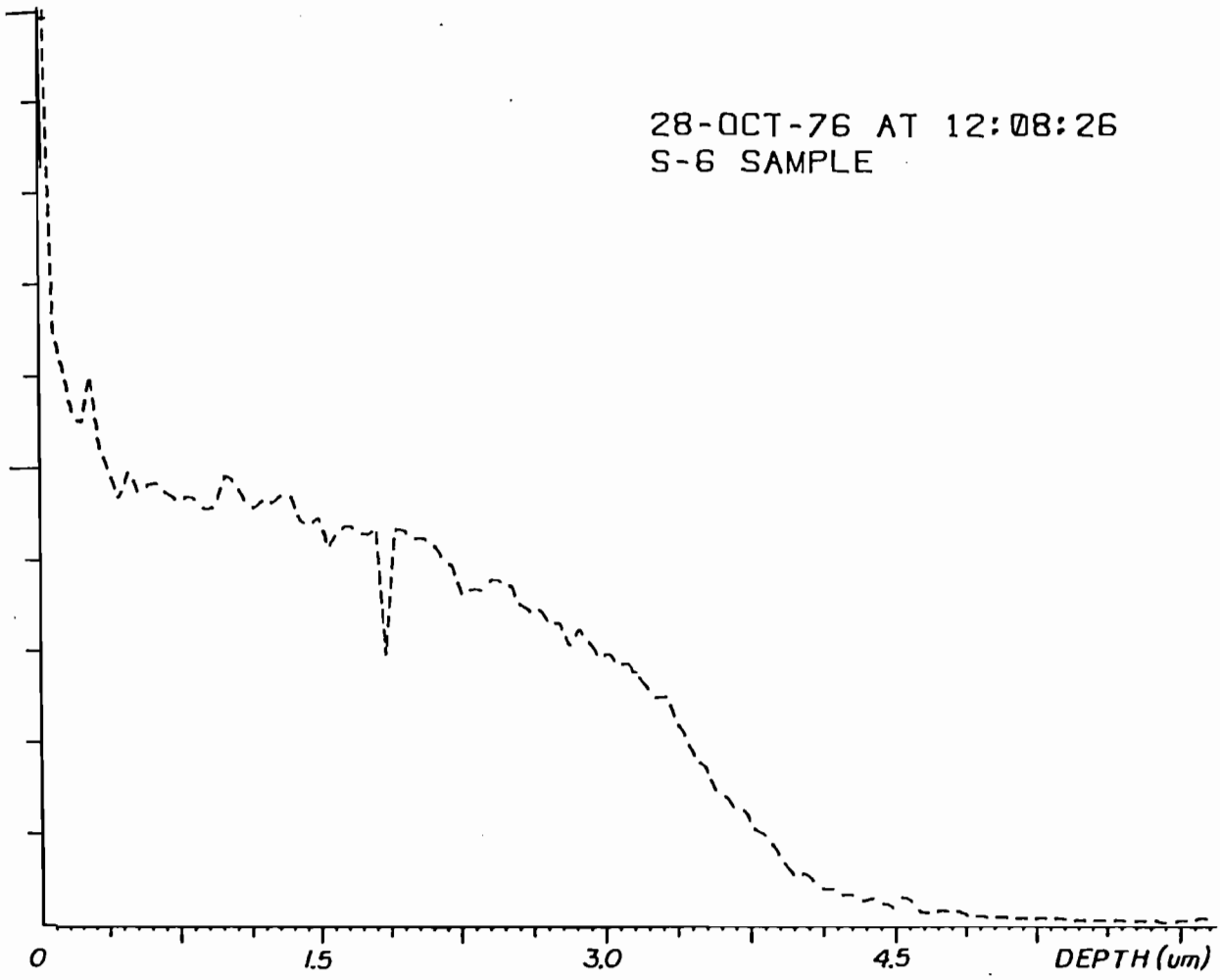

Figure IV-47. Sample S-6

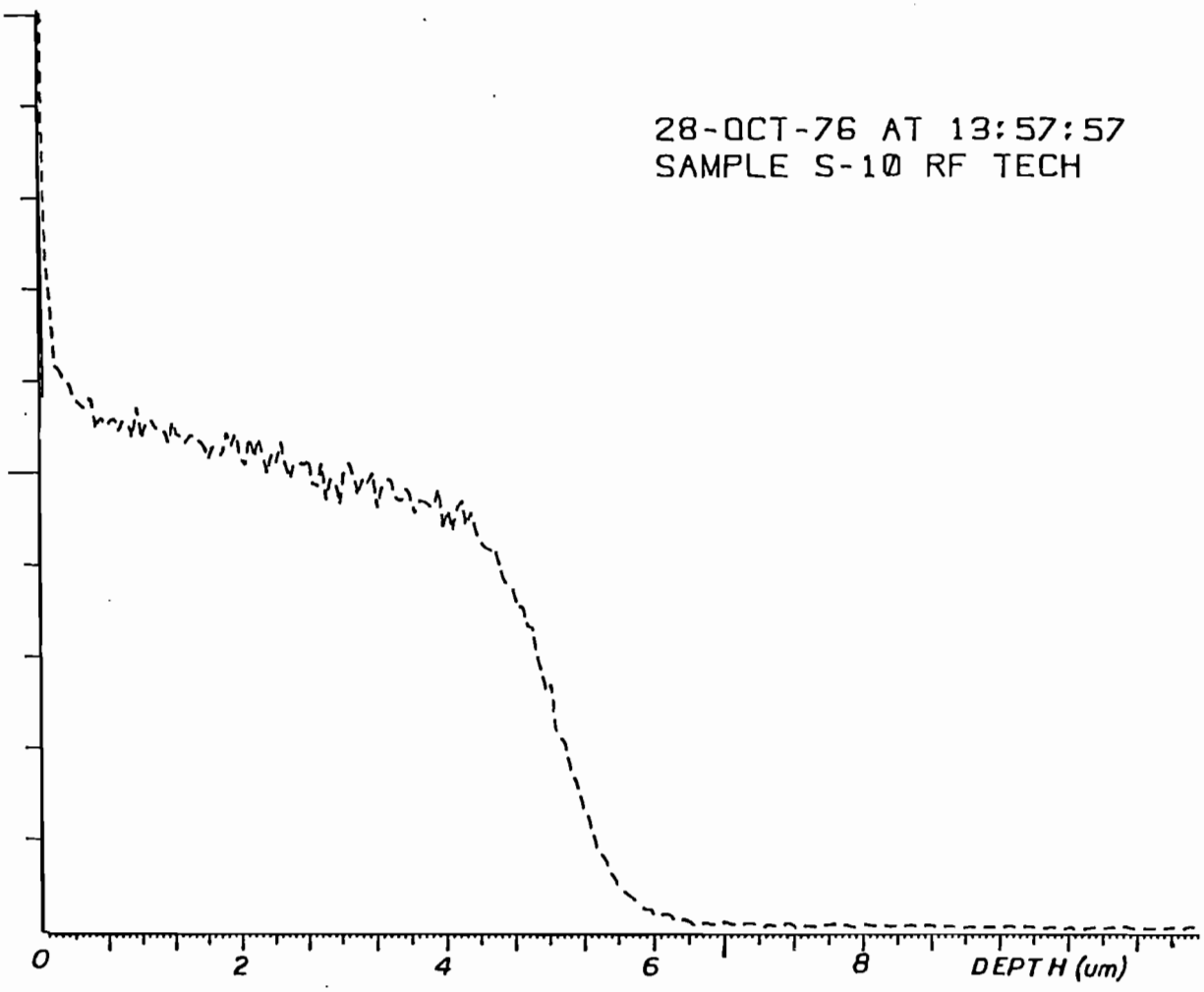

Figure IV-48. Sample S-10

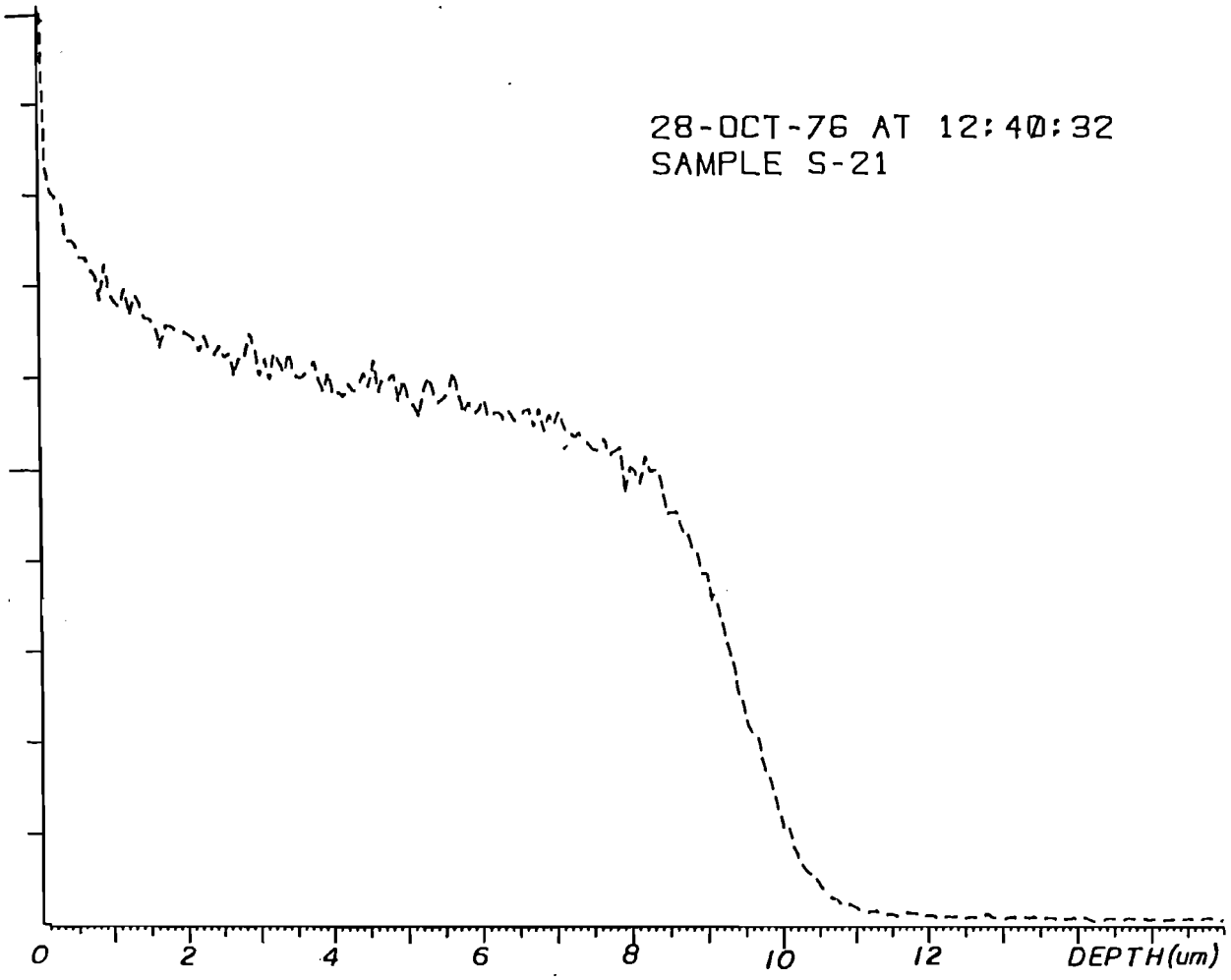

Figure IV-49. Sample S-21

some evidence of a plateau can be seen. The other three samples show well-developed plateaus, with a well-defined knee at the Nb-Nb_3Sn phase boundary. Two features are especially interesting. The first is the ratio of count rates at the beginning and end of the plateau. For S6, S10 and S21, these ratios are 1.37, 1.32, and 1.30. These values are all less than the allowed ratio of Sn concentrations at the Sn-rich and Nb-rich phase boundaries in the Nb-Sn phase diagram. This ratio is 1.61, according to the phase diagram of ref. 4. The entire plateau region is therefore apparently within the stoichiometric range inside which single phase Nb_3Sn may exist.

We also note that the diffusion tail at the Nb-Nb_3Sn phase boundary is sharper than was the case with the ionplated samples, extending only a micron or so into the Nb substrate.

Sn-Rich Vapor-Diffused Samples

The final two profiles (Figures 50 and 51) are samples U2 and U4, fired for two hours and four hours, respectively, in the same apparatus used for the "S" series just discussed, but with no restricting screen to limit the flux of Sn vapor into the sample surface. The surface Sn concentration was therefore greater with these samples than with the "S" series samples. It will be recalled that cavity #4WG and several strips fired in this manner showed condensed Sn spots,

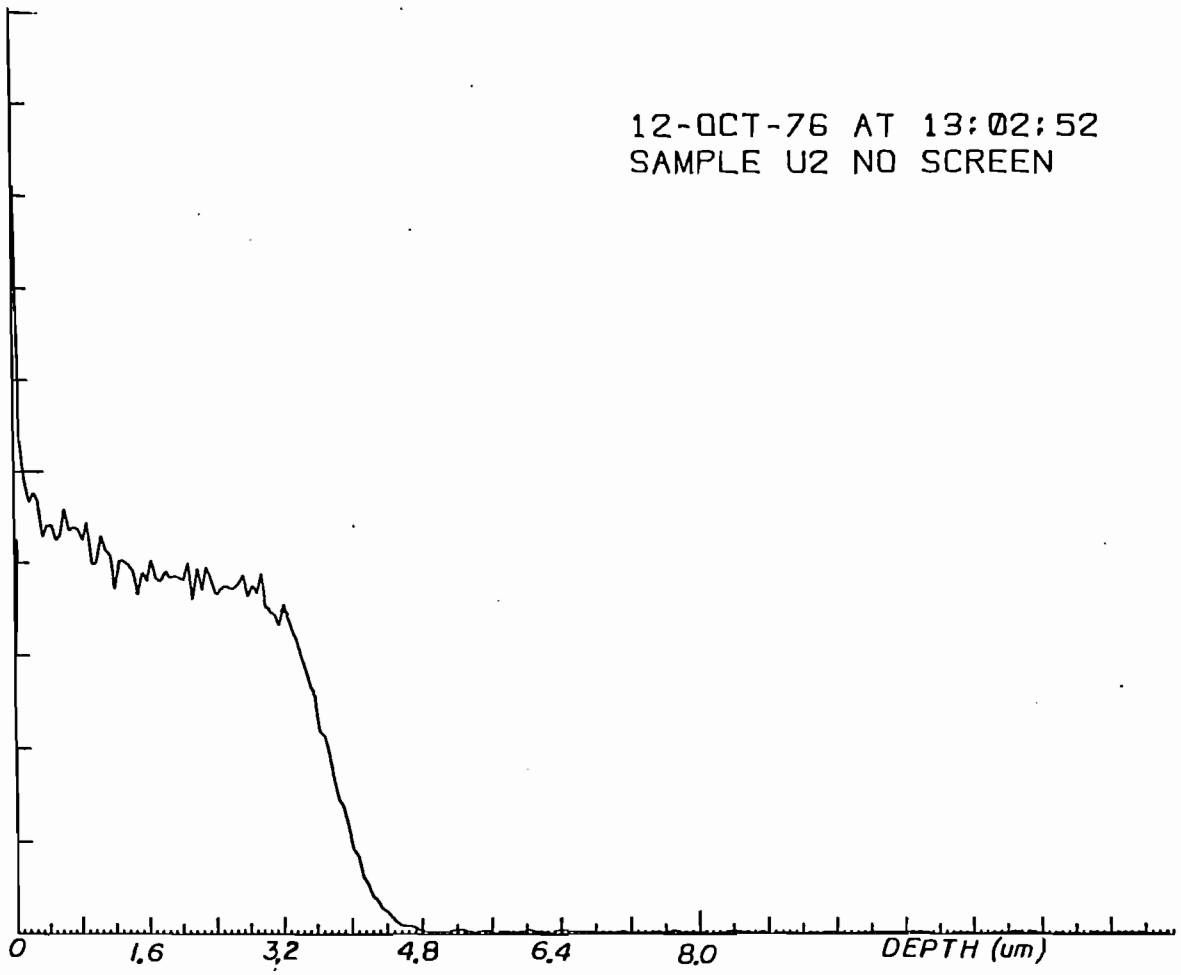

Figure IV-50. Sample U-2

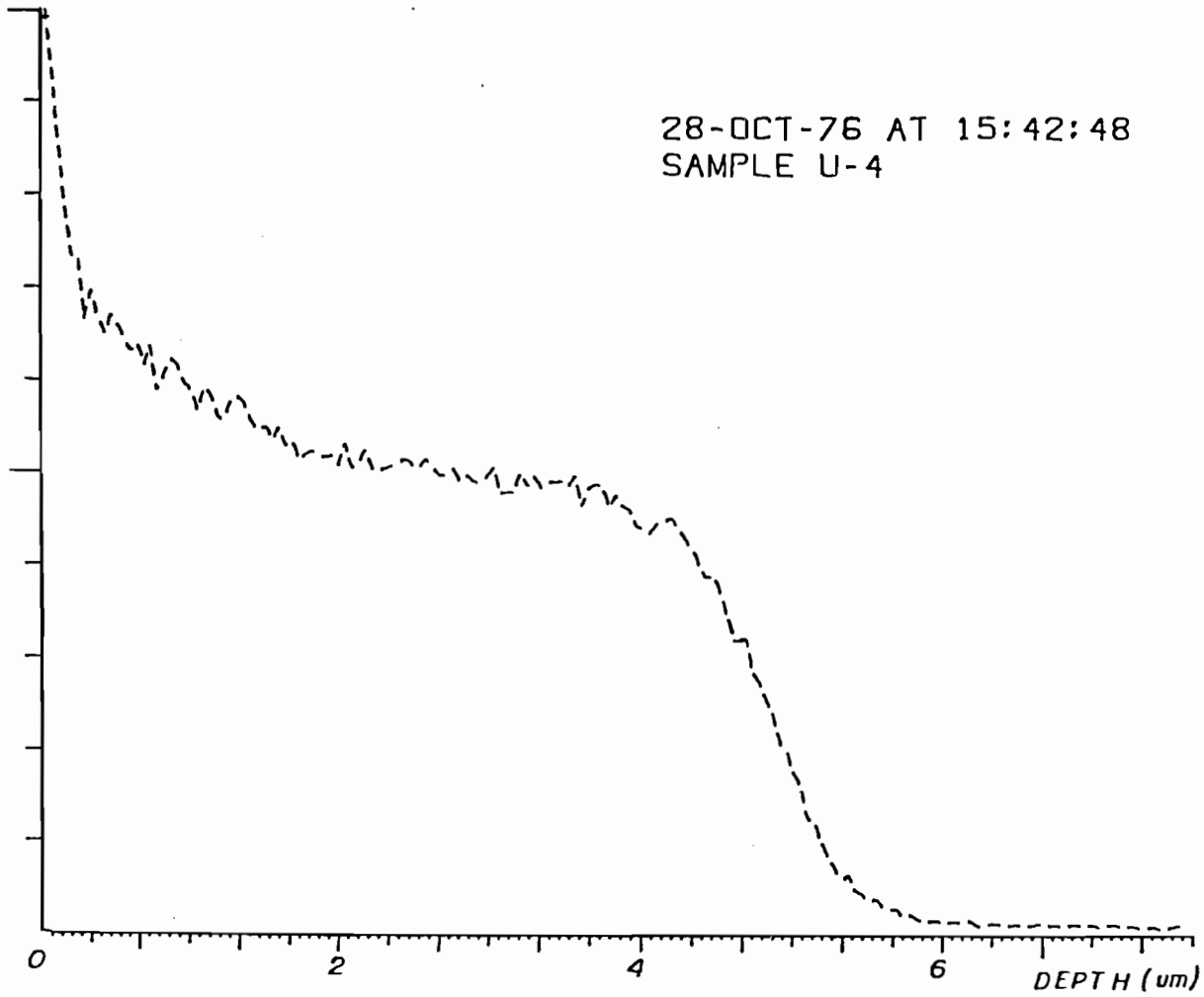

Figure IV-51. Sample U-4

indicating that Sn vapor was being supplied to the surface faster than it could diffuse away. No Sn droplets were observed on U2 or U4, probably because of the shorter firing times involved, but the profiles nonetheless show distinct differences from those of the "S" samples.

Both profiles show significant concave-upward curvature in the plateau region, contrasting with the straight plateaus of S6, S10, and S21. The ratio of knee concentration to surface concentration for U2 is 1.39 while for U4 it is 1.61, reaching the maximum allowable ratio for a single phase Nb_3Sn region. This suggests that the surface is just ready to precipitate either Sn or an Sn-rich phase after 4 hours reaction time, and explains why cavity #4WG, which was fired 20 hours, showed Sn condensation while U2 and U4 did not.

Referring again to Figure 49, we note that S21 also shows a small concave up region near the surface, and the stoichiometric ratio is 1.52 if this region is included. This suggests that, for a given flux of Sn vapor, there exists a certain maximum firing time beyond which surface Sn accumulation begins.

Growth Rates

As the final step in this study of Nb_3Sn layers, the growth rate of vapor-diffused layers was measured, using the method discussed in Chapter III.

Two series of strips were prepared. The "S" series samples S3b, S6, S10, and S21 were produced using a restrictive screen over the Sn source and duplicate as closely as possible the cup region of cavity #4SM. The "U" series samples U2 and U4 were produced without the restrictive screen and duplicate the cup region of cavity #4WG. An additional sample, reacted 21 hours in unrestricted Sn vapor, was already available and served to complete the "U" series. All samples were fired at a temperature of 1050°C.

The purpose of the "U" series was to determine whether the higher surface Sn concentration would result in a different growth rate.

Results

Nb_3Sn thicknesses versus reaction times for all samples are plotted in Figure 52.

The "S" samples show evidence of a nucleation time of approximately 1.8 hours, after which growth begins, with fairly rapid growth during the first 6-10 hours, and slower growth thereafter. The 1.8 hour figure for reaction time can be demonstrated in two independent ways. Linear extrapolation of the S3b and S6 thicknesses to zero thickness gives 1.8 hours as the zero thickness intercept. In addition, the measured thickness of sample IV3 can be used to support the 1.8 hour figure. IV3 was pre-nucleated by ionplating a thin layer of Sn; thus growth into the substrate should have

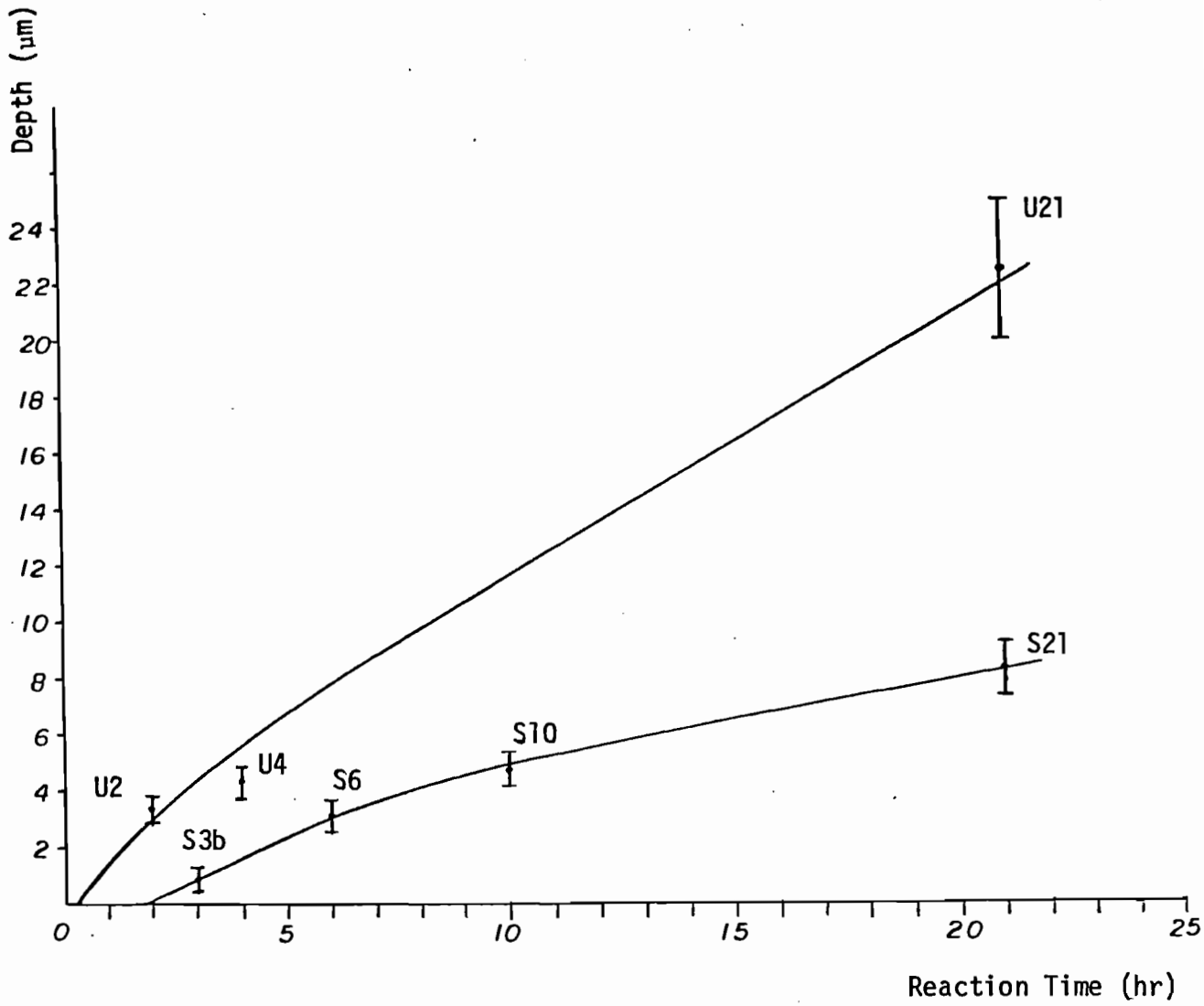

Figure IV-52. Growth rates of vapor diffused sample strips

started almost immediately. Since all other reaction parameters were identical to those of the "S" series, growth rate after nucleation should have been the same as for the S samples. If we move the IV3 point from 3 hours to 4.8 hours to allow for the absence of a nucleation period, the IV3 point fails on the growth curve of the "S" series.

The three "U" series samples show quite different behavior. Their growth rate is much faster than that of the "S" series, and shows no significant reduction for the 21 hour sample. The nucleation time is also apparently very short. Particularly remarkable is the 20-25 μ thickness achieved after 21 hours of reaction.

References for Chapter IV

1. The author is indebted to Mr. J. R. Salem, formerly of Stanford Univ., for his enlightening comments regarding $NbSn_2$ diffusion barriers.

2. Hillenbrand, B., Martens, H., Pfister, H., Schnitzke, K., and Uzel, Y., "Superconducting Nb_3Sn Cavities with High Microwave Qualities", 1976 Applied Superconductivity Conf., Stanford Univ., Stanford, Calif., Aug. 1976.

3. Horl, H. M., and Rieder, K. H., J. Vacuum Sci. & Tech. 276-278 (1971).

4. Charleswirth, J. P., Macphail, I., and Madsen, P. E., "Experimental Work on the Niobium-Tin Constitution Diagram and Related Studies", J. Materials Sci. 5, 580-603 (1970).

V. ANALYSES AND DISCUSSION OF RESULTS

1. Effects of Sn Concentration

Introduction

Throughout the experimental program, the Sn concentration present during reaction was observed to influence the appearance of the resulting Nb_3Sn surface, and this Sn concentration seemed to have a more significant effect than any other reaction parameter. With ionplated samples, the Sn concentration is established by the presence of a relatively thick layer of pure Sn at the substrate surface throughout the early stages of reaction, and no means exist to vary this concentration in a controlled manner. Despite this, the differences in surface texture between the "leopard spot" regions, which were covered with liquid Sn during most of the reaction period, and the interspot regions, which quickly became Sn-depleted, suggested that the reaction process was strongly influenced by Sn concentration.

Vapor-diffused cavities generally had lower Sn concentrations during reaction, and since the Sn concentration depended upon the design and location of the Sn source, some experimental control was possible. The evolution of the vapor-diffusion process consisted of progressively lowering the Sn concentration during reaction, with special adjustments made, as necessary, to provide for complete nucleation

during the initial stages of reaction.

The reduction in Sn concentration from ionplated levels to that of the "restricted" vapor-diffused cavities was accompanied by a considerable improvement in r.f. performance. It is natural to inquire whether this improved performance is directly attributable to lowered Sn concentration, and to this end we will discuss the microscopic and compositional studies described in Chapter IV, their correlation with Sn concentration and r.f. performance, and possible reasons for these correlations.

Relation Between Sn Concentration and Surface Texture

The correlation between Sn concentration and surface texture is apparent in the photomicrographs of Chapter IV. Considering first the ionplated surfaces, we find a consistently larger grain size and rougher surface finish in the spot regions, which were covered with liquid Sn throughout most of the reaction period, than in the interspot regions, which were depleted of excess Sn fairly early. Since the entire cavity half received the same treatment during fabrication and firing, this difference between different regions of the same cavity half must be attributable to the different Sn concentrations during reaction.

Comparing ionplated samples with vapor-diffused samples, which generally had lower Sn concentrations during reaction, we find that the vapor-diffused samples had smaller grain

size and smoother surface finishes. An exception is observed for those vapor-diffused samples onto which liquid Sn condensed; the grain size and surface finish in these regions resembled that of the ionplated samples.

Relation Between Sn Concentration and Sn Concentration Profiles

A correlation can also be found between Sn concentrations during reaction and the shape of the resulting SIMS Sn concentration profile.

As discussed in Chapter II, a good Nb_3Sn layer for r.f. applications should have uniform crystal structure and stoichiometry to a depth of at least 2-3 μm. Since SIMS Sn counting rates are determined by the Sn concentration and structure of the sample, a SIMS Sn profile of such a layer should show a flat, or nearly flat, plateau, representing stoichiometric Nb_3Sn, with a distinct "knee" at the Nb_3Sn-Nb phase boundary.

Referring back to Chapter IV (Figures 40-42) we note that the "leopard spot" regions of the ionplated surfaces show no such plateau. Only in the Sn-depleted "interspot" regions is a plateau observed. Ionplated surfaces with a sputtered Nb overlayer (Figures 44-45) likewise show a steeply sloping plateau.

Only with vapor-diffused samples is a flat plateau and sharp "knee" observed. The samples showing the flattest plateaus (Figures 48-49) are the "restricted" vapor-diffused

samples, in which the flux of Sn vapor was reduced using a restrictive screen over the Sn source. Samples reacted in saturated Sn vapor (Figures 50, 51) show steeper plateaus, and also show some concave-up curvature in the plateau region.

Reducing the Sn concentration from the large value existing in the ionplated samples to the lower value provided by saturated Sn vapor and then to a still lower value by restricting the vapor source thus results in a progressively flatter Sn concentration plateau, indicating more uniform crystal structure and stoichiometry.

Growth Rates

It should also be noted that the growth rates of Nb_3Sn layers depend upon Sn concentration. Ionplated samples fired for 80-120 minutes have Nb_3Sn layers typically 3 μm thick, as shown in Figures 43 and 44 of Chapter IV. Saturated vapor-diffused samples show similar growth rates, while "restricted" vapor-diffused samples grow considerably more slowly.

2. A Model for Nb_3Sn Growth

We can explain the observed growth rates and Sn concentration profiles of vapor-diffused Nb_3Sn layers by developing a simple model for Nb_3Sn growth. The differences between samples grown in saturated Sn vapor and those grown in

unsaturated vapor can be understood using this model, and these differences, together with a study of the Nb-Sn phase diagram, suggest an explanation for the differing morphology of the ionplated samples.

The model assumes that the formation of Nb_3Sn occurs at the Nb_3Sn-Nb interface, beneath the growing Nb_3Sn layer. This assumption has been verified by Old and Macphail[1] in their study of Nb_3Sn growth. The growth rate is therefore limited by the rate at which Sn is transported through the growing Nb_3Sn layer to the Nb_3Sn-Nb interface. Depending upon the reaction conditions, the growth rate may also be limited by the rate at which Sn vapor condenses onto the sample surface. This was the case with the unsaturated vapor-diffused samples S3b, S6, S10, S21, and cavities #4SM and #3SM, and we consider these samples first.

Unsaturated Vapor Diffusion

We assume that Sn atoms condense onto the sample surface with a flux J_o (atoms/cm^2-hr), and that this flux remains constant throughout the reaction period. These Sn atoms diffuse through the growing Nb_3Sn layer, with a diffusivity K_1 (cm^2/hr) and a thickness $X_o(t)$. At the Nb_3Sn-Nb interface, the Sn concentration corresponds to the lower stoichiometric limit for the Nb_3Sn phase; we label this concentration ρ_{min}. To extend the Nb_3Sn layer a distance dX_o further, we must supply enough Sn atoms to bring the region between X_o and X_o+dX_o up to the concentration ρ_{min}.

We assume that the amount of Sn arriving at the depth X_o is equal to the condensation flux J_o. This neglects the loss of some Sn flux which goes into raising the regions $X < X_o$ from ρ_{min} to their final concentrations. We also assume that the reaction time necessary to convert the region between X_o and X_o+dX_o into Nb_3Sn, once the necessary amount of Sn is pesent, is small compared to the time in which the Nb_3Sn layer advances the distance dX_o.

Given these conditions, the growth rate is

$$\frac{dX_o}{dt} = J_o/\rho_{min} \tag{1}$$

The corresponding concentration profile follows from the diffusion equation

$$J_o = -K_1 \text{ grad } \rho \tag{2}$$

and we have

$$\rho(X) = \rho_o + \frac{J_o}{K_1} (X_o - X) \tag{3}$$

At depths greater than X_o, Sn atoms are diffusing into the Nb substrate with diffusivity K_2, which is assumed to be much smaller than K_1 due to the smaller lattice parameter and higher melting point of Nb. Assuming again that the Nb_3Sn layer advances slowly, the appropriate diffusion problem is that of a semi-infinite slab with the concentration at $X=X_o$ maintained at $\rho(X_o) = \rho_{min}$. The concentration for $X > X_o$ is then

$$\rho(X) = \rho_{min}\left|1 - \text{erf}\left(\frac{X_o}{\sqrt{4K_2\Delta t}}\right)\right| \qquad (4)$$

where Δt is roughly the time required for the Nb_3Sn to advance from X_o to X and overtake the advancing Sn.

Within the admittedly coarse limits of our approximations, Equations (1), (3), and (4) describe the concentration profiles of samples S6 and S10 very well. We predict a linear plateau whose slope increases as the Sn flux J_o is increased, followed by a diffusion "tail". We also get a growth rate which is constant, i.e., the Nb_3Sn thickness increases linearly with time.

For thicker layers of Nb_3Sn, the condensation flux J_o is not the only growth-rate limiting factor, since the diffusion-limited flux of Sn through a thick Nb_3Sn layer might be less than J_o. If $\rho(0)$ is the Sn concentration at the surface of the Nb_3Sn layer, then the diffusion flux is at most

$$J_{diff} = K_1 \frac{\rho(0) - \rho(X_o)}{X_o} = K_1 \frac{\rho(0) - \rho_{min}}{X_o} \qquad (5)$$

If the thickness of the Nb_3Sn layer exceeds a critical value

$$X_{crit} = \frac{K_1}{J_o}[\rho(0) - \rho_{min}] \qquad (6)$$

then the condensing Sn will not all be carried into the interior, and $\rho(0)$ will rise as Sn accumulates near the surface. This behavior can be seen in sample S21, which had

a longer reaction time than the "flat" samples S6 and S10, and in samples S2 and S4, which were reacted in saturated Sn vapor and thus had larger values for J_o.

Growth Rate for Unsaturated Vapor Diffusion

The observed growth rates for unsaturated vapor-diffused samples may also be fit using the simple model just derived. We assume

$$\frac{dX_o}{dt} = \text{minimum} \quad \begin{matrix} J_o/\rho_{min} \\ \frac{K_1}{\rho_{min}} \frac{\rho(0) - \rho_{min}}{X_o} \end{matrix} \qquad (7)$$

We take a value for ρ_{min} corresponding to the lower stoichiometric limit for Nb_3Sn (17 Atomic % Sn according to reference 2), and take the ratio $\rho(0)/\rho_{min}$ to be about 1.33, based upon the SIMS data of Chapter IV.

The Sn flux J_o is derived from Equation (1) and the measured growth rates of samples S3b and S6. The SIMS profiles of these two samples indicate that they are both in the linear growth region, and their measured thicknesses yield a value

$$\left.\frac{dX_o}{dt}\right|_{linear} = 0.75\ \mu/hr \qquad (8)$$

The Sn flux is therefore

$$J_o = \rho_{min} \left.\frac{dX_o}{dt}\right|_{linear} \cong 10^{18}\ \frac{atom}{cm^2\ hr} \qquad (9)$$

The value of the diffusivity K_1 is chosen to give the

best agreement between Equation (7) and the measured thicknesses of samples S10 and S21. A value

$$K_1 = 5.5 \times 10^{-8} \text{ cm}^{-2} \text{ hr}^{-1} \qquad (10)$$

gives the smooth curve of Chapter IV and fits the data rather well.

Accumulation of Surface Sn

It is apparent from Equation (3) that if growth continues with a constant condensation flux J_o, the surface Sn concentration $\rho(0)$ will rise continuously as the thickness X_o of the Nb_3Sn layer increases. Two possibilities exist:

(1) If the diffusivity K_1 increases sufficiently quickly with increasing Sn concentration, the additional Sn flux can be accommodated at a value of $\rho(0)$ which is still within the stoichiometric range of the Nb_3Sn phase.

(2) If the diffusivity K_1 cannot rise sufficiently, or if reaction times are long enough, $\rho(0)$ will exceed the upper stoichiometric limit for Nb_3Sn, and the surface layer will undergo a phase transition.

According to the phase diagram of reference 2, the equilibrium composition at 1050° for Sn concentrations exceeding 27% is a two phase composite of Nb_3Sn and a liquid (presumably Sn with dissolved Nb).

Extended reaction times at a fixed condensation rate or shorter reaction times at high condensation rates will

therefore result in accumulation of liquid Sn as was observed in several of the samples. Since the transport of Sn through this two-phase region will differ considerably from transport through solid Nb_3Sn, changes in concentration profiles and growth rates should be expected.

Saturated Vapor-Diffusion Growth Rates

It is apparent from the growth rate data of Chapter IV that the growth rate of the unscreened "U" series samples cannot be explained by the model above unless a considerably larger diffusion constant is assumed. Even if one assumes a value $K_1 = 36\ \mu^2\ hr^{-1}$, which is about the minimum value required to fit the U21 result, the essentially parabolic plot which results cannot be made to fit the U4 depth, and a better fit can be obtained by assuming a linear time-thickness relation.

One must suspect, then, that the transport mechanism responsible for the U series growth rates differs from that of the S series. Such a mechanism has been proposed by Old and Macphail[1] to explain anomalous growth rates of Nb_3Sn layers produced by immersing Nb in liquid Sn.

Old and Macphail assume the existence of an additional Nb_3Sn formation mechanism, in which Nb, dissolved in the liquid Sn surrounding the substrate, deposits as crystalline Nb_3Sn, with a rate constant K_c, thus supplementing the usual diffusion growth, and yielding a growth rate

$$\frac{dX_o}{dt} = \frac{K_1}{\rho} \frac{\rho(0) - \rho(X_o)}{X_o} + K_c \quad \text{(deposition region)} \quad (11)$$

This augmented deposition occurs in the cooler parts of the substrate, and is balanced by a loss of Nb in the hotter regions

$$\frac{dX_o}{dt} = \frac{K_1}{\rho_{min}} \frac{\rho(0) - \rho(X_o)}{X_o} - K_c \quad \text{(depletion region)} \quad (12)$$

The average growth rate is then found to be, at 1050°C,

$$\bar{x}_o(\mu) = 8.15(t(hr))^{0.36} \quad (13)$$

and this relation predicts a thickness of 24.4 μ for a 21 hour reaction time. The agremeent between this figure and the 20-25 μ thickness of U21 is, however, a suspicious coincidence, since the reaction conditions do not exactly duplicate those of Old and Macphail.

The location of the S and U samples was probably slightly cooler than the surrounding regions, since the samples were in the center of a vacuum vessel which was heated by radiation through its side walls. The appropriate rate expression should therefore be Eq. (11).

In addition, we should account for the fact that Sn is now supplied from a thin liquid layer, which must be replenished by condensing Sn vapor, rather than from an "infinite" pool. The rate is therefore limited by the Sn vapor flux, as in the previous model, and we have

$$\frac{dX_o}{dt} = \text{minimum} \quad \frac{J_o^{sat}/\rho_{min}}{\frac{K_1}{\rho_{min}} \frac{\rho(0) - \rho(X_o)}{X_o} + K_c} \tag{14}$$

Using the value $K_c = 1.1\ \mu/hr$, we get the solid line in Figure 52 of Chapter IV. This value for K_c agrees well with the value $K_c = 1.4\ \mu/hr$ which can be derived from the discussion of Old and Macphail.

Effects of Sn Concentration upon R.F. Performance

Thus far we have established a fairly convincing correlation between the Sn concentration present during the formation of a Nb_3Sn layer and the surface texture, Sn concentration profile and growth rate of the layer. We also saw from the r.f. performance data of Chapter IV that reduction of the Sn concentration resulted in improved r.f. performance. In this section we consider why the structure and composition of layers grown at low Sn concentrations yield better r.f. performance.

As discussed in Chapter II, r.f. performance of a superconducting compound is expected to be best for layers having smooth surface finish, uniform stoichiometry, and microstructural uniformity.

The microscopic and SIMS investigations described in Chapter IV establish directly the fact that lower Sn concentrations resulted in smoother surface finish and more uniform

stoichiometry, the latter property being indicated by the existence of a nearly flat SIMS plateau.

The relationship between Sn concentration, microstructure and r.f. performance is perhaps not as obvious, and we therefore consider some previous work on Nb_3Sn which sheds some light on this relationship.

Old and Macphail[1], in their study of Nb_3Sn layers grown by immersing Nb in liquid Sn, report that rough, irregular growth occurs when the liquid phase is present during growth, in agreement with the results reported here for ionplated surfaces. They attribute this irregular growth, as mentioned in the discussion of saturated vapor diffusion growth rates, to dissolution of Nb in the liquid Sn, followed by precipitation of Nb_3Sn crystals from solution. A layer formed in this manner has no way of preserving the crystallographic order and surface contour of the original substrate, since the growth of each new Nb_3Sn crystal is independent of that of the surrounding Nb_3Sn crystals, and of the crystallographic orientation of the original substrate material. The resulting microstructure thus consists of randomly oriented crystals, with dislocation planes or even microscopic void spaces between crystals. These irregular grain boundaries would almost certainly result in poor r.f. performance, and might also explain the increased porosity observed with ionplated surfaces.

Old and Macphail also reported the precipitation of $NbSn_2$ crystals during specimen cooling. This type of precipitation was not generally observed in this work, possibly because samples were usually fired until all excess Sn had evaporated. Such $NbSn_2$ formation might, however, have occurred at grain boundaries, with dimensions too small to be detected using the anodization technique. Such precipitation would degrade r.f. performance still further.

We conclude, then, that the poor performance of the ion-plated cavities could be attributable to the presence of the liquid phase during the formation of the Nb_3Sn layer.

Since formation of a liquid phase may also be allowed to occur with vapor-diffused samples, either by providing an excessive flux of Sn vapor, or by extending reaction times too long, care must be taken when using the vapor-diffusion process to limit the amount of Sn vapor to a value which, for a given Nb_3Sn thickness, will keep the surface Sn concentration below the upper stoichiometric limit of the Nb_3Sn phase. Specific methods for doing this will be discussed in the next chapter.

Nucleation of Nb_3Sn Layers

Thus far our discussion of Nb_3Sn growth has been limited to the evolution of already formed Nb_3Sn layers, and we concluded that low Sn vapor concentrations are necessary for the growth of good Nb_3Sn layers.

In practice, considerable difficulty was experienced in achieving nucleation of a continuous Nb_3Sn layer when Sn vapor concentrations were restricted to such low values. We therefore discuss the nucleation of continuous Nb_3Sn films, and some of the means employed to enhance nucleation.

Perhaps the most important parameter in determining whether or not a continuous surface layer will be formed is the lateral or surface mobility of the Sn atoms during the initial stages of growth.[3,4] It is this parameter which determines whether condensing Sn atoms will diffuse into the substrate at the initial condensation site or spread laterally before diffusing into the interior. High lateral mobility encourages formation of a continuous film, and any surface structure which inhibits lateral mobility is likely to cause bare spots.

Prominent substrate grain boundaries are apparently especially effective barriers, as indicated by the experience with cavity #3SM (Figures 36-38, Chapter IV). Since the diffusivity of Sn along grain boundaries is high, surface Sn reaching a substrate grain boundary is carried along the grain boundary into the substrate interior and does not cross the boundary.

The nucleation problem is aggravated by the fact that, during reaction, Sn atoms condense preferentially onto regions which are already Sn-rich. There is almost certainly

preferential condensation onto existing liquid Sn droplets, if any are present. This is the only reasonable way to account for the massive accumulation of Sn on cavity #4WG (Figure 7, Chapter IV). Preferential condensation also seems to occur onto already nucleated Nb_3Sn regions, as suggested by Figure 8 of Chapter IV. The cavity half illustrated was used during development of nucleation enhancement techniques and, although it did not have prominent substrate grain boundaries, shows incomplete nucleation. The alternating patches of dense, matte finish Nb_3Sn and thin, specular Nb_3Sn, similar to the two surface finishes observed on cavity #4BSM, suggest that most of the Sn condensation occurs on already nucleated Nb_3Sn regions, thus "starving" the other regions of Sn and inhibiting nucleation there. The already nucleated regions can then coalesce, forming a connected network, while the unnucleated voids persist until the condensed layer is quite thick. Such behavior in evaporated metal films is discussed in reference 3.

It appears, then, that unless some means is provided to ensure nucleation of a continuous Nb_3Sn layer at the start of the reaction period, bare spots existing during the start of the reaction period will persist for a considerable time at the Sn vapor concentrations necessary for good steady-state growth.

Two nucleation-enhancing techniques were employed in

this study, and both are capable of nucleating continuous layers.

The first is the "Siemens" technique, which utilizes a thermal gradient to provide extra Sn vapor during the start of the reaction period, and a protective anodic oxide film on the substrate to allow condensation of a continuous Sn film before the Nb:Nb_3Sn reaction begins. This technique is quite satisfactory, provided some means is available for elevating the Sn source temperature above the substrate temperature during the start of the reaction period.

The second technique is that of "prenucleating" the substrate by depositing a thin layer of Sn before reacting in Sn vapor. Although ionplating was used to deposit this prenucleating layer, sputtering or thermal evaporation could also have been used. Both would provide more precise control of Sn thickness than is possible with ionplating. The thickness of the prenucleating layer should probably be held to less than about 2000 Å to prevent formation of the liquid phase.

Nb Inclusions in Nb_3Sn Layers

A problem analogous to that of nucleating a continuous Nb_3Sn layer is that of preventing the inclusion of unreacted Nb in the growing Nb_3Sn layer. It was observed that the r.f. performance of the unsaturated vapor diffused cavities #3SM and #4SM deteriorated seriously after removal by oxipolishing

of only 1-2 μm of the surface. $R_s(T)$ plots of these cavities, made after oxipolishing, also showed extensive structure near 9.2°, suggesting the presence of exposed Nb. Since the average thickness of these Nb_3Sn layers was about 5 μm, it appears that unreacted Nb exists at a depth considerably less than the average Nb_3Sn thickness.

The microscopic examinations of cavity #4SM, described in Chapter IV, suggest an explanation for this behavior. Although the surface of this cavity was completely covered with Nb_3Sn, oxipolishing to a depth of about 2.5 μm revealed the structures shown in Figures 26 and 27 of Chapter IV. Both structures show regular rows of pink Nb_3Sn penetrating a blue Nb region, with spacings of about 10 μm between rows, suggesting structure in the Nb_3Sn with characteristic dimensions of a few microns.

Barbee et al., in their extensive study of co-evaporated Nb_3Sn layers[5], report columnar growth, with appreciable intercolumnar void space, for co-evaporated layers deposited at substrate temperatures between 450° and 750°C. The amount of intercolumnar void space is greatest at the lower substrate temperatures studied, and characteristic void dimensions at these temperatures are 2-4 μm. They also report that the lateral mobility of the condensing atoms is the parameter controlling the morphology of the deposited layers, and characterize their results in terms of the ratio T_s/T_m of

substrate temperature to melting temperature, in agreement with the earlier work of Movchen and Demchisin.[6]

The growth mechanism of vapor-diffused layers differs from that of co-evaporated layers, in that growth occurs beneath the surface for vapor-diffused layers. The structure determining mobility is therefore limited by bulk diffusion at the Nb-Nb_3Sn interface, rather than by surface diffusion at the Nb_3Sn-vapor interface. Since bulk diffusion is the slower process, we expect vapor-diffused layers to be characterized by a lower effective substrate temperature, and intercolumnar voids of the type reported by Barbee et al., can be expected even at substrate temperatures as high as 1050°C.

Such intercolumnar voids, consisting in this case of unreacted Nb, explain both the observed r.f. performance and the microscopic structures of the unsaturated vapor-diffused cavities. These voids would be smaller in size and number near the original Nb_3Sn surface, since this region was formed first, and the subsequent flux of Sn through the surface region would eventually eliminate voids near the surface. Deeper regions of the Nb_3Sn layer would have progressively more void space, explaining the degradation in r.f. performance as this void space is exposed by oxipolishing.

Development of a satisfactory technique for preventing Nb inclusions of the type discussed here would require a more

complete understanding of the reaction kinetics of the vapor diffusion process. Suggestions for further work in this direction are made in the next chapter.

Multiphase Inclusions

In addition to Nb inclusions, some inclusions of Sn-rich phases were observed. These inclusions represent local excesses of Sn concentration, rather than local scarcities, as was the case with the Nb inclusions.

While multiphase inclusions seem more common in samples with higher Sn concentrations and regions of samples expected to have higher Sn concentrations than other regions of the same sample, their occurrence cannot be entirely attributed to an overall Sn excess. Even in fairly Sn-poor samples, yellow Sn inclusions were observed. This suggests that some mechanism exists, most likely during cooling, whereby the excess Sn in a fairly large region is transported to a location favorable for nucleation and forms a Sn-rich precipitate. Precipitation probably occurs at grain boundaries because of the more favorable energetics there and also because diffusion along grain boundaries, which is much faster than bulk diffusion, is morely likely to allow the rapid transport of enough Sn during the relatively quick cooldown.

References for Chapter V

1. Old, C. F., and Macphail, I., "The Mechanism and Kinetics of Growth of the Superconducting Compound Nb_3Sn", J. Materials Sci. 4, 202-207 (1969).

2. Charlesworth, J. P., Macphail, I., and Madsen, P. E., "Experimental Work on the Niobium-Tin Constitution Diagram and Related Studies", J. Materials Sci. 5, 580-603 (1970).

3. Maissel and Glaing, Handbook of Thin Films (McGraw-Hill, 1970).

4. Chopra, K. L., Thin Film Phenomena (McGraw Hill, 1969).

5. Howard, R. E., King, C. N., Norton, R. H., Zubeck, R. B., Barbee, T. W., and Hammond, R. H., "Critical Current and AC Loss of Coevaporated Nb_3Sn Superconductors", Stanford Univ.

6. Movchen, B. A., and Demchisin, A. V., Fiz. Met. Metalloved 28, 653 (1969).

VI. FURTHER POTENTIAL OF Nb_3Sn

We have seen that vapor diffused Nb_3Sn cavities are capable of surfaces resistances below 1 μΩ and accelerating fields of over 7 MV/m at 8.6 GHz. These results are sufficiently encouraging that one could expect to achieve values acceptable for accelerator applications given a little more experience. Historically, however, the transition from single cavities to multi-cavity accelerator structures has been a difficult one. We discuss, therefore, those problems which might arise when trying to extend these results to more complex cavity geometries. We then discuss possible reasons for the still relatively high surface resistances observed in this study, and point out potential means for achieving lower surface resistances. Finally, we discuss the potential for achieving higher breakdown fields.

Application of Nb_3Sn to Complex Accelerator Structures

Two difficulties repeatedly encountered with Nb structures have been regenerative electron phenomena (multipactor) and localized contamination ("dust"). Both difficulties may also be expected with Nb_3Sn structures. The possibility exists that Nb_3Sn surfaces, because of lower secondary emissions, might allow higher breakdown fields in multipactor-prone structures. No multipactor was observed in any of the cavities tested, but the field levels were low enough

that multipactor would not have been expected with Nb structures at this frequency. No conclusion can be reached, therefore, concerning multipactor behavior of Nb_3Sn.

The "dust" problem seems to scale with cavity size, since even one localized bad spot can limit the accelerating field to a low value. Nb_3Sn seems to be no more sensitive to localized contamination than does Nb. Because of the limited thickness of the Nb_3Sn coating, the use of electropolishing to remove contaminated regions is of limited usefulness, but it is not particularly difficult to recoat a cavity with Nb_3Sn after electropolishing or other "repairs". Nb_3Sn did show, in the course of the experimental program, resistance to formation of the insoluble oxide NbO, and this resistance to NbO formation seems to exceed that of Nb.

Since the residual resistances achieved to date with Nb_3Sn are considerably higher than those achieved with Nb, the resistance of Nb_3Sn cavities to gradual Q-degradation cannot be directly compared with that of Nb cavities. On the whole, however, the sensitivity of Nb_3Sn to contamination seems no worse than that of Nb.

Coating Uniformity

The most significant difficulty with large Nb_3Sn structures is likely to be that of uniformly coating a structure having complicated geometry. So far the best Nb_3Sn r.f. results have been obtained only with cavities of

very simple geometry.[1] With more complicated structures, special care must be taken to insure uniform growth on all interior surfaces, or at least to confine the non-optimum growth to regions which are not exposed to high surface fields.

Since the microstructure and r.f. performance of the Nb_3Sn layers studied here show correlations with the Sn concentration during reaction, one should expect that structures of complex geometry will show a variation of properties from place to place, depending upon local reaction conditions. One must therefore not only coat all interior surfaces with at least a minimum thickness, but also insure that throughout the reaction period and over the entire structure, the reaction conditions do not exceed the range within which high quality Nb_3Sn layers are produced. An analogous situation exists with electroplating, where the term "plating range" is used for the range of current densities over which deposits having specified properties (e.g. grain size, hardness, purity) are produced. If a complex shape is to be plated, care must be taken to insure that the current densities over the entire surface are within this plating range.

Multiple anodes are commonly used in electroplating to provide uniform current distributions and, by analogy, the use of multiple Sn sources should allow uniform distribution

of Sn vapor over complex structure geometries. This technique was used to a limited extent in cavities 6WG, 4SM and 3SM, where the distribution of holes in the Sn source cover was made asymmetrical to withhold Sn from one side of the cup. With the open geometry of the cavities used here, no further elaboration seems necessary. Multicell structures such as the Cornell "muffin tin" structure[6], the Wuppertal structure[2], or the HEPL structure[3] could be treated with the Sn source shown in Figure 1. Here the source consists of a thin-wall Nb tube, perhaps 1 cm in diameter and closed at both ends. It would be suspended at the centerline of the accelerator structure, as illustrated. Small holes drilled along the tube circumference at appropriate heights permit the escaping Sn vapor to be aimed as necessary. The closed bottom end could easily hold enough Sn for several firings.

Attainment of Lower Surface Resistances

We discuss in this section some possible explanations for the still relatively high surface resistances obtained for Nb_3Sn, and possible means of achieving lower resistances.

The first question to be asked is whether the temperature dependent BCS surface resistance or the temperature independent residual resistance is responsible for the Q-limitation at 4.2°. To date the lowest Nb_3Sn surface resistances have been achieved by the Siemens group who report a value $R_{BCS}(9.5\ GHz) = 0.25\ \mu\Omega$ at 4.2°. This should

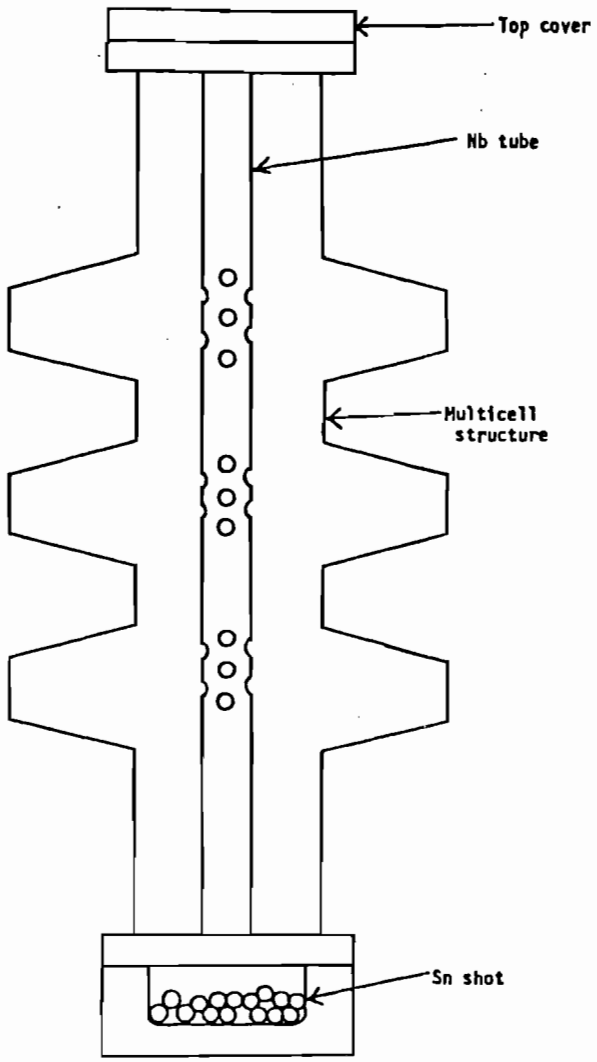

Figure VI-1. Proposed Sn source for multicell structures

correspond to a value $R_{BCS}(8.6\ GHz) = 0.20\ \mu\Omega$ at our lower operating frequency. Residual resistance subtraction for the data of cavities #3SM and #4SM gives RBCS values between 0.1 μΩ and 0.3 μΩ, and suggests that we are approaching BCS values for the temperature dependent surface resistance. This conclusion is also supported by the high T_c values observed, which indicate good stoichiometry and ordering, and by the fairly low λ_o values. The latter, at about 2000-3000 Å, compare favorably with the values reported by Kneisel *et al.*[3] for 30 kHz measurements of polished Nb_3Sn samples, and indicate that the mean free path in our layers is not excessively short.

It appears, then, that the superconducting properties of our Nb_3Sn layers are quite satisfactory, and that it is the residual resistance which, so far as is known, is unrelated to the superconducting properties, which is responsible for the high surface resistances obtained.

We next inquire as to the length scale of the defects responsible for the high residual resistance. We are aided here by two "yardsticks": the coherence length ξ_o and penetration depth λ_o of the superconductor. Since structural defects with a length scale smaller than ξ_o would degrade all of the superconducting properties, including T_c, we can conclude that defects with a length scale less than about 400 Å are not responsible for our high surface resistances.

A similar argument applies to the values obtained for the penetration depth λ_o. Surface defects with a length scale comparable to the penetration depth would interrupt the flow of shielding currents which prevent field from entering the superconductor, and would by definition result in large values for the penetration depth λ_o.

Both observations together suggest that the defects have a characteristic size of 1 μm or more. Since the grain size of vapor-diffused Nb_3Sn layers has been reported to be between one and a few μm[4], r.f. losses at these grain boundaries are a likely cause of the high residual resistance and should be the object of further study.

Anomalous high frequency resistances have been reported for thin Ta films[5] which were explained by oxidation at grain boundaries. Analogous effects seem possible for Nb_3Sn layers because of the chemical similarity of Nb and Ta, and because of the evidence of chemical activity at grain boundaries revealed by the microscopic observations of Chapter IV.

In order to reduce grain boundary losses, one desires a reaction environment which produces a minimum amount of structural disruption at the Nb-Nb_3Sn interface during formation of the Nb_3Sn layer. Such disruption, it would seem, must inevitably lead to Nb_3Sn layers with porous grain boundary structures, with correspondingly high r.f. losses.

An extreme example of such structural disruption is the Macphail solution-deposition mechanism, in which the Nb substrate is transformed into a third phase (a liquid Sn-Nb solution) which then precipitates Nb_3Sn crystals. Since no orientation with the original Nb lattice is preserved, the growing Nb-Nb_3Sn interface is highly discontinuous. Reduction of the Sn concentration prevents formation of the liquid phase and results in a direct transformation from alpha-phase Nb to Nb_3Sn. In order to predict the conditions under which this solid-solid transformation will produce the least amount of structural disruption, we should attempt to visualize the phase transition on an atomic scale.

In order to transform a unit cell of Nb into a unit cell of Nb_3Sn, three things must happen, not necessarily in the following order:

1) The lattice must expand.
2) Sn atoms must replace Nb atoms on the corner and body center lattice sites.
3) The displaced Nb atoms must move into their new positions on the cube faces.

If Sn diffusion occurs very slowly, then the lattice expands uniformly over rather large regions, since the lattice constants of solid solutions show a linear, or nearly linear, relation between lattice constant and solute concentration. The very slow change in Sn (solute) concentration

resulting from the low diffusion flux therefore produces a gradual change in lattice constant which can be accommodated elastically, without producing discontinuous boundaries.

As the lattice expands, it becomes much easier for Nb atoms to move into the "interstitial" positions on the unit cell faces, and the A15 structure begins to form. The high Nb mobility afforded by the increased lattice constant allows easy redistribution of Nb atoms over significant distances, thus allowing uniform stoichiometry to be attained.

The Nb-Nb_3Sn transformation, if in fact it proceeds as suggested here, results in a continuous structural change. This should result in a low density of grain boundaries. If the growth rate is increased beyond a certain point, the change in lattice constant becomes too abrupt to be accommodated by the elastic properties of the lattice. This results in discontinuous changes in structure, with void, or at least highly dislocated, regions separating "expanded" and "unexpanded" domains. These domains then undergo the Nb-Nb_3Sn transformation individually, some early, some late, depending upon when each domain reaches critical stoichiometry. The void regions separating these domains then become grain boundaries. Since diffusion of either Nb or Sn across these boundaries is difficult, variations in stoichiometry can exist from grain to grain.

Based upon the above considerations, the ideal reaction

environment would be one which provides for a very low Sn diffusion rate. Two other considerations, however, might set a lower limit on the diffusion rates which may be used.

The first consideration is that of nucleating a continuous surface layer. This problem can be solved either by providing a higher Sn flux at the start of the reaction period, or by providing a plated pre-nucleation layer, as was done with cavity #3SM.

A second, more fundamental consideration involves the formation of Nb inclusions. While we can only speculate on the formation kinetics which result in these inclusions, there are reasons for suspecting that very low Sn diffusion fluxes might result in a large density of Nb inclusions, thus setting a lower limit on Sn diffusion flux.

It seems likely that the diffusion rate of Sn through Nb_3Sn is greater than that of Sn through Nb. This follows from the higher melting point of Nb and from the fact that the SIMS profiles of vapor-diffused samples showed relatively short Sn "tails" following the Nb-Nb_3Sn phase boundary: a higher Sn diffusivity in Nb would have resulted ina longer Sn "tail". It also appears that the sticking coefficient of Sn vapor is greater on Nb_3Sn than on Nb. At very low growth rates, therefore, the available Sn vapor might preferentially condense onto already reacted Nb_3Sn regions and preferentially diffuse through Nb_3Sn regions, bypassing

unreacted Nb regions.

Very low Sn diffusion rates would also result in high sensitivity of the Nb_3Sn layer to defects in the Nb substrate. This arises because of the ability of Nb grain boundaries, which are quite pronounced in UHV degassed material, to function as diffusion barriers, thus preventing uniform Nb_3Sn growth at low Sn diffusion fluxes. This difficulty might be partially overcome by using fine grained Nb for the substrate material. Cavity #6WG, for example, whcih was not UHV degassed, had smaller Nb grains than cavities #3SM and #4SM and showed fewer Nb inclusions.

Another possibility for eliminating Nb inclusions arising from low Sn vapor fluxes is the introduction of a post-reaction annealing period as the final step in the firing cycle. By supplying a very low partial pressure of Sn vapor during this period, sufficient to prevent Sn depletion of the Nb_3Sn surface but insufficient to permit continued vertical growth into the substrate, lateral diffusion of Sn might be encouraged sufficiently to result in elimination of the Nb inclusions formed during growth of the Nb_3Sn layer.

Although the 20 hr., 750°C anneal given the ion plated cavity #1SM did not result in any improvement in performance, the ion plated cavities as a group did not show the same type of Nb inclusions as the vapor diffused cavities,

and the possibility exists that vapor diffused cavities might respond more favorably to annealing.

Proposed Process Modifications

The most promising process modification would be the inclusion of some means of varying the Sn vapor flux during the firing cycle. This could be accomplished by providing a separate heater for the Sn source, so that the source temperature and the substrate temperature could be varied independently.

By raising the Sn source temperature substantially higher than the substrate temperature at the start of the firing cycle, the high vapor flux necessary to ensure nucleation of a continuous Nb_3Sn layer could be provided. The source temperature could then be lowered to provide a vapor flux suitable to sustain steady state Nb_3Sn growth, and could be reduced gradually as the thickness of the Nb_3Sn layer increased, thus ensuring that the surface Sn concentration stayed below the Nb_3Sn stoichiometric limit. After the desired thickness had been obtained, the source temperature could then be lowered still further to provide for the annealing step described above.

An alternate technique which has been proposed by Pfister *et al.*[1], provides for nucleation enhancement by the inclusion of a small amount of the stannous salts SnF_2 or $SnCl_2$. These salts are more volatile than pure Sn and could

provide a higher Sn vapor flux during the start of the firing cycle. This technique would not, by itself, allow tailoring of the vapor flux during the rest of the firing cycle, however.

Another possibility that should be investigated is the use of substrate temperatures below 930°C. The decision to use temperatures above 950°C in this study was based upon the desire to preclude formation of the Sn-rich phases Nb_6Sn_5 and $NbSn_2$. Reliable control of the Sn source temperature would, however, allow sufficient control of Sn concentration to prevent formation of these undesirable phases.

The sequence undergone by a volume element of substrate material during the reaction cycle is indicated by the line A-E on the phase diagram shown in Figure 2. At the start of the cycle, the volume element consists of pure Nb and lies at point A on the phase diagram. After reaching reaction temperature (point B), Sn diffusion begins, and the composition changes until the Nb_3Sn phase boundary is reached (point C). At this point the entire volume element has the A-15 structure. Further Sn diffusion enriches the Sn-concentration of the A-15 phase and, provided cooldown begins within the Nb_3Sn stoichiometric limits, (point D), a single-phase sample results.

It can be seen from the alternate sequence AB'C'D'E that choice of a reaction temperature below 930°C results in

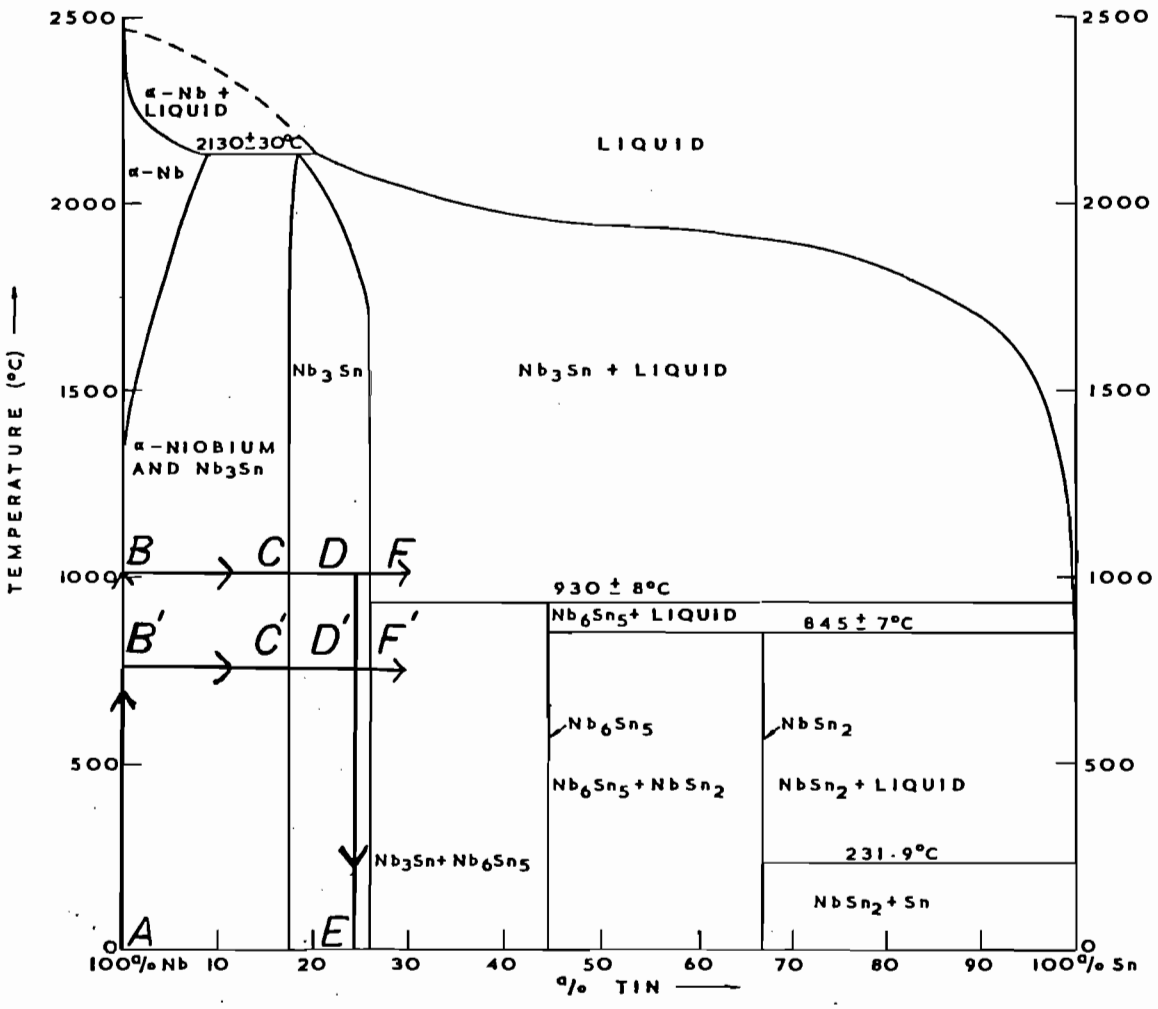

Figure VI-2. Two possible reaction paths indicating alternate choice of reaction temperature

essentially the same sequence, although the Sn diffusion rates will be lower. Should the reaction period be too long, the composition of the volume element will exceed the Nb_3Sn stoichiometric limit, and Nb_6Sn_5 precipitation will begin (point F'). It is not clear, however, that the effects of Nb_6Sn_5 precipitation would be as serious as those of liquid phase formation and the "Macphail mechanism" which would occur at higher reaction temperatures (point F). In addition, the Nb_3Sn-Nb_6Sn_5 transformation, since it is a solid-solid transformation, would occur less rapidly than the solid-liquid transformation at point F, and should therefore be easier to control.

Attainment of Higher Breakdown Fields

The origins of the breakdown field and means of increasing it have formed for several years the subject of lively debate and will doubtless continue to do so. Three factors, however, are usually agreed upon:

1. The energy gap of the superconductor should be large, and the surface should be free of non-stoichiometric or disordered regions having locally reduced energy gaps.
2. The surface should be smooth and dense, providing no rough projections or holes which could allow flux entry at low field levels or encourage field emission.
3. The thermal conductance to the helium bath should be as high as possible.

In practice, the precautions necessary to satisfy these three criteria for a given material are the same as those necessary to produce low surface resistances. The large energy gap dictated by 1 and the long mean free path and low grain boundary density necessary for good thermal conductivity also contribute to low R_{BCS}, for example. The second condition, while not originally thought to influence R_s directly, does apparently have some relation to R_s, since the reaction conditions resulting in highest cavity Q's also produced smooth, specular and non-porous finishes.

The only obvious parameter remaining is the thickness of the Nb_3Sn layer then. Since the better vapor-diffused cavities showed little or no improvement in breakdown field upon lowering the operating temperature from 4.2° to below 2°, and did not show the thermal "breakdown" behavior exhibited by the ionplated cavities, it seems unlikely that the thermal conductance to the helium bath was a field-limiting factor. It would therefore appear that the Nb_3Sn thickness could be increased somewhat, allowing more extensive use of oxipolishing to produce a smoother and more uniform surface.

The present vapor-diffusion technique cannot produce layers thicker than about 8 μm without producing excessively high surface Sn concentrations, and seems likely to produce a high density of Nb inclusions if the Sn vapor flux is

reduced in an attempt to produce thicker layers. Use of a separate Sn source heater would eliminate these limitations and, coupled with more experience in pre-test surface preparation, should result in higher breakdown fields.

So What Does It Mean?

The potential of Nb_3Sn for accelerator structures can be appreciated if the performance of the Nb_3Sn layers produced to date is translated into the performance expected of a multicell accelerator structure incorporating such layers.

Taking as an example the Cornell 11-cell "muffin-tin" structure, which has a geometry factor

$$\Gamma = 233 \text{ ohms}$$

and a ratio of peak magnetic field to accelerating field

$$H_{max}/E_{acc} = 64 \quad \text{Gauss/MV m}^{-1}$$

and taking as obtainable values for vapor-diffused Nb_3Sn surfaces the values

$$R_s(4.2°) = 1\times10^{-6} \text{ ohm}$$

$$H_{max} = 400 \text{ Gauss}$$

we predict a quality factor

$$Q_o = 2\times10^8$$

and an accelerating field

$$E_{acc} = 6 \text{ MV/m}$$

which compares favorably with the Q_o of 1×10^9 and the accelerating field of 4 MV/m which were obtained with the Nb 11-cell structure at 1.5°K.

The comparison is even more favorable if allowance is made for the fact that the optimum performance obtainable from Nb_3Sn layers has clearly not been achieved in this study. If one takes the performance reported by Siemens[1] as an obtainable value ($R_s = 0.3 \times 10^{-6}$ ohm, $H_{max} = 1000$ Gauss), then the comparison is even more favorable.

Although the performance of single-cell Nb cavities still exceeds that of Nb_3Sn cavities, it appears that the performance of actual accelerating structures is limited by factors, such as regenerative multipactor, which do not depend strongly upon the local properties of the superconductor. It therefore appears that Nb_3Sn could be used for such structures with no loss of accelerating field, and with a slight increase in r.f. power requirements. This slight advantage would be amply compensated by the higher operating temperature of the Nb_3Sn structure.

References for Chapter VI

1. Hillenbrand, B., Martens, H., Pfister, H., Schnitzke, K., and Uzel, Y., "Superconducting Nb_3Sn Cavities with High Microwave Qualities", 1976 Applied Superconductivity Conf., Stanford Univ.

2. Arnolds, G., "Measurements on a Nb_3Sn Structure for Linear Accelerator Application", 1976 Applied Superconductivity Conference.

3. Kneisel, P., Stoltz, O., and Halbritter, J., "Nb_3Sn for Superconducting Cavities', Intnl. Cryogenic Materials Conf., Queens Univ., Kingston, Ontario, Canada (July 1975).

4. Halbritter, J., 1976 Applied Superconductivity Conference.

5. Maissel, L. I., "Electrical Properties of Sputtered Tantalum Films", Trans. 9th Natl. Vac. Symp. (1962).

6. Padamsee, H., et al., 1976 Applied Superconductivity Conf.

Appendix A

FURNACE CONSTRUCTION

Two furnaces were used during the course of this work. Most of the strip samples were fired in a 1" (25 mm) tube furnace, while the last few strip samples and all of the cavities were fired in a 3.5" (90 mm) tube furnace. Since the two furnaces were similar except for size, only the larger one will be described fully, and specific differences between it and the smaller furnace will be noted, as appropriate.

Both furnaces consisted of inner and outer tubular vacuum systems, which were inserted into an electric resistance furnace with a hot zone approximately 14" (35 cm) long. The inner vacuum system of the large furnace consisted of a 3.5" Nb tube, 20" (51 cm) long, rolled from 1/16" (1.6 mm) Nb sheet, with electron-beam (EB) welded seams and a 1/16" Nb end cap. The open end of the Nb tube was EB welded to a 1" long, 3.5" diameter OFHC copper transition tube, which was then EB welded to a 3.5" diameter stainless tube approximately 60" (152 cm) long. The copper transition was necessary because Nb cannot be welded directly to stainless. The open end of the stainless tube was TIG (Tungsten-inert gas) welded to a 6" Varian vacuum flange, and connected with 1.5" stainless and copper gaskets to a 220 l/sec. Vac-Ion pump. Access to the interior for sample insertion is provided by a

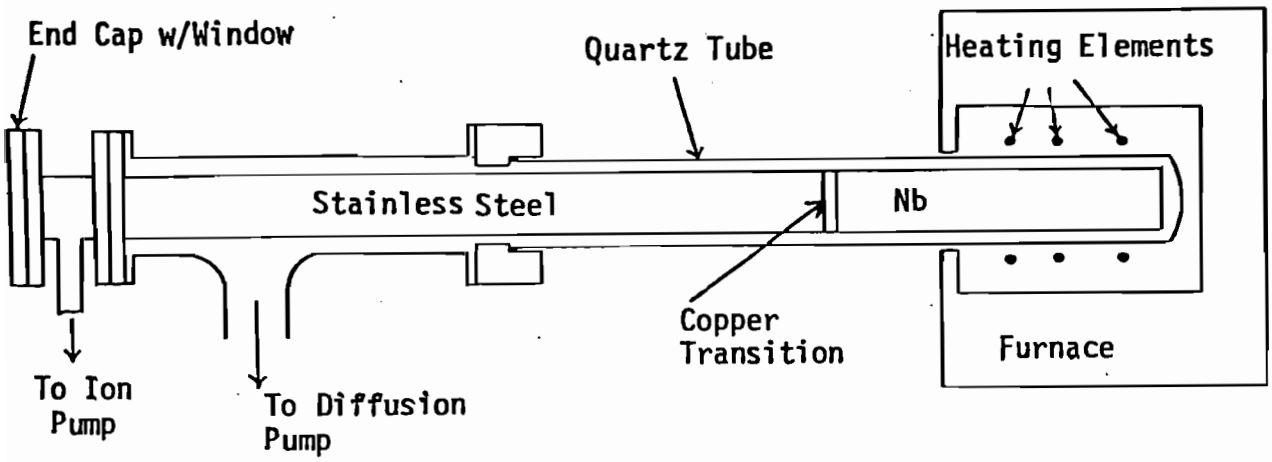

Figure A-1. Furnace Construction

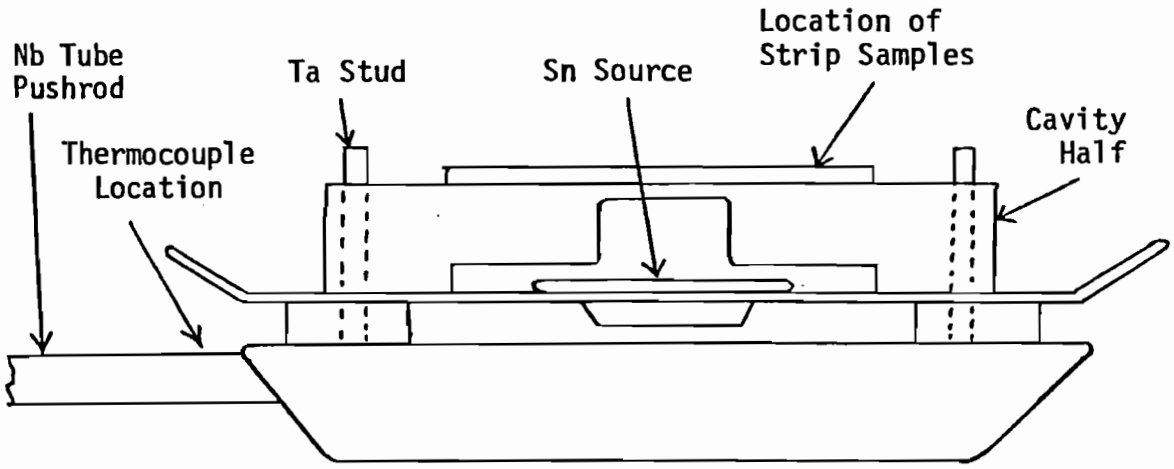

Figure A-2. Details of "sled" sample holder

removable 6" Varian end flange, which is fitted with a 1.5" glass window. No special baffling was provided to prevent migration of Sn vapor towards the cold end of the furnace.

Samples to be fired were placed on a "sled" (Figure 2) made from 1/16" Nb sheet, and secured with tungsten or tantalum bolts or, in the case of some strip samples, with Nb wire. The sled was attached to a Nb pushrod which passed through a 36" (91 cm) stainless bellows attached to the removable end flange. Samples could thus be inserted into or withdrawn from the hot region under vacuum.

All of the hot regions of the furnace are constructed of Nb to avoid contaminationof the samples. This is important because samples are not sealed in ampullas, but are pumped continuously during firing. Pressure, measured with an ionization gauge at the cold end of the furance, is a few times 10^{-6} mm during firing, and $2\text{-}4\times10^{-6}$ after cooldown.

Temperature is measured with a Chromel-Alumel thermocouple inside the Nb pushrod and attached physically to the sample sled. All readings were referenced to an ice bath.

The outer vacuum system consisted of a 96 mm I.D. x 100 mm O.D. fused quartz tube, fitted to a brass manifold with a viton O-ring seal and evacuated with a small oil diffusion pump. Pressure in the outer vacuum system was kept below about 10^{-5} mm during firing to prevent deterioration of the inner Nb tube.

Maximum continuous operating temperature for the large furnace was 1050°C and was limited by the close proximity of the quartz tube to the furnace heating elements. The smaller furnace, which had a 1" diameter Nb inner vacuum system inside a 75 mm quartz tube, could be continuously operated at 1150°-1250°C.

Appendix B

DERIVATION OF SELECTED MICROWAVE CIRCUIT RELATIONS

We derive here the relations between the coupling factors (β_1, β_2) and the measured power levels (p_i, p_r, p_e, p_T) for a 2-port resonant cavity. From these relations is derived a relation between cavity Q_o and insertion loss which is useful for determination of Q_o at high temperatures.

Equivalent Circuit of 2-port Cavity

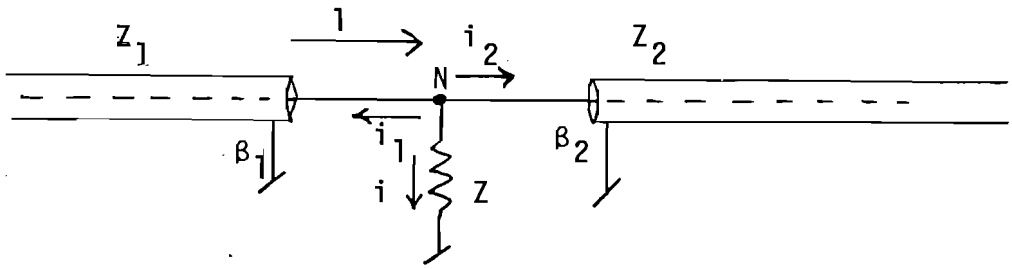

We represent the cavity at resonance as a resistive load Z when viewed from a reference plane coincident with the input coupling port. The input and output feeds are represented as transmission lines with impedance Z_1 and Z_2, respectively, and the coupling factors are

$$\beta_1 = Z/Z_1 \qquad \beta_2 = Z/Z_2 \qquad (1)$$

We assume an incident current of unit magnitude, which is divided into a reflected current i_1, a transmitted current

i_1, a transmitted current i_2 and an absorbed current i. Current conservation at point N then requires that

$$1 = i + i_1 + i_2 \tag{2}$$

The voltage drops across the feed lines are:

$$v_c = iZ = v_2 = i_2 Z_2 = v_1 = (1 + i_1)Z_1 \tag{3}$$

where the factor $(1 + i_1)$ results from in-phase current reflection at the cavity input aperture.

Putting (3) and (1) into (2) gives

$$1 = \frac{(1+i_1)}{\beta_1} + i_1 + (1+i_1)\cdot\beta_2/\beta_1$$

or

$$i_1 = \frac{\beta_1 - 1 - \beta_2}{1 + \beta_1 + \beta_2} \tag{4}$$

$$i_2 = (1 + i_1)\cdot\beta_2/\beta_1 \tag{5}$$

$$i = \frac{1 + i_1}{\beta_1} = \frac{2}{1 + \beta_1 + \beta_2} \tag{6}$$

Now since the power flow in each branch is $p_j = i_j^2 Z_{j_1}$ we have:

$$p_i = Z/\beta_1 \tag{7}$$

$$p_r = \left(\frac{\beta_1 - 1 - \beta_2}{1 + \beta_1 + \beta_2}\right)^2 Z/\beta_1 \tag{8}$$

$$p_T = \left(\frac{2\beta_2}{1 + \beta_1 + \beta_1}\right)^2 Z/\beta_2 \tag{9}$$

$$p_{abs} = \left(\frac{2}{1 + \beta_1 + \beta_2}\right)^2 Z \tag{10}$$

and the "emitted power" resulting from a sudden shutoff of incident current, is

$$p_e = [i_1 - (-1)]^2 \, Z/\beta_1 = \left(\frac{2\beta_1}{1 + \beta_1 + \beta_2}\right)^2 Z/\beta_1 \qquad (11)$$

It is convenient now to normalize to unit incident power by dividing Equations (8)-(11) by p_i. All subsequent equations will refer to normalized power levels.

$$p_r = \left(\frac{\beta_1 - 1 - \beta_2}{1 + \beta_1 + \beta_2}\right)^2 \qquad (12)$$

$$p_T = \left(\frac{2}{1 + \beta_1 + \beta_2}\right)^2 \beta_1\beta_2 \qquad (13)$$

$$p_{abs} = \left(\frac{2}{1 + \beta_1 + \beta_2}\right)^2 \beta_1 \qquad (14)$$

$$p_e = \left(\frac{2\beta_1}{1 + \beta_1 + \beta_2}\right)^2 \qquad (15)$$

We now derive (β_1, β_2) from $\{p_j\}$. We note that

$$p_T/p_e = \beta_2/\beta_1 \rightarrow \beta_2 = p_T/p_e \, \beta_1 \qquad (16)$$

and inserting (16) into (15), we get

$$\beta_1 = \frac{\sqrt{p_e}}{2 - \sqrt{p_e}\,(1 + p_T/p_e)} \qquad (17)$$

Thus (16) and (17) can be used to determine (β_1, β_2) if p_T and p_e can be measured accurately.

If p_e cannot be measured accurately but p_r and p_T are known, we proceed from (12)

$$\sqrt{p_r} = \frac{1 - \beta_1 + \beta_2}{1 + \beta_1 + \beta_2} \qquad (\beta_1 - \beta_2 < 1) \qquad (18)$$

$$1 - \sqrt{p_r} = \frac{2\beta_1}{1 + \beta_1 + \beta_2}$$

$$\frac{(1 - \sqrt{p_r})^2}{p_T} = \frac{\beta_1}{\beta_2} \rightarrow \beta_1 = \frac{(1 - \sqrt{p_r})^2}{p_T}\,\beta_2 \qquad (19)$$

and since

$$1 - p_T - p_r = \frac{4\beta_1}{(1 + \beta_1 + \beta_2)^2} = p_T/\beta_{2_1} \text{ we have}$$

$$\beta_2 = \frac{p_T}{1 - p_T - p_r} \qquad (20)$$

Thus (19) and (20) may be used if p_T and p_r are known.

An additional case which may arise is that of extreme overcoupling ($\beta_1 >> 1$). In this case, Eq. (18) is incorrect, and Eq. (17) may introduce large errors unless p_e is measured very accurately. In this case, we take

$$\sqrt{p_r} = \frac{\beta_1 - \beta_2 - 1}{1 + \beta_1 + \beta_2} \qquad (\beta_1 - \beta_2 > 1) \qquad (21)$$

$$1 + \sqrt{p_r} = \frac{2\beta_1}{1 + \beta_1 + \beta_2} = \frac{2\beta_1}{1 + \beta_1(1 + p_T/p_e)}$$

whence

$$\beta_1 = \frac{1 + \sqrt{p_r}}{2 - (1 + \sqrt{p_r})(1 + p_T/p_e)} \qquad (22)$$

and (16) and (22) may be used to determine (β_1, β_2)

Relation Between Cavity Q and Insertion Loss

Pulsed cavity measurements are very difficult to make at

high cavity temperatures because of the difficulty of phase-locking the cavity electronics. In this case the insertion loss p_T/p_i may be used to determine Q_o, provided accurate measurements of Q_o, β_1 and β_2 have been made at some lower temperature.

For fixed coupling apertures, the coupling factor β_1, β_2 are proportional to cavity Q_o, and we define the "Sundelin B-factors"

$$B_1 = \beta_1/Q, \qquad B_2 = \beta_2/Q \tag{23}$$

B_1, B_2 are independent of temperature and depend only upon the aperture site.

Taking Eq. (13) and inserting $\beta_j = B_j Q_o$, we have

$$p_T = \left(\frac{2}{Q_o^{-2} + B_1 + B_2}\right)^2 B_1 B_2$$

$$Q_o = \left[2\sqrt{\frac{B_1 B_2}{p_T}} - B_1 - B_2\right]^{-2} \tag{24}$$

and this relation may be used to determine Q_o from CW measurements of p_T, once (B_1, B_2) have been determined from measurements at lower temperatures.

Appendix C

ANODIZATION AS A TECHNIQUE FOR PHASE IDENTIFICATION

Introduction

As discussed earlier, r.f. applications of superconducting Nb_3Sn require the production of single phase coatings, since the presence of even small amounts of unreacted Nb or Sn, or of the Sn-rich phases Nb_6Sn_5 and $NbSn_2$, would degrade r.f. performance considerably. It is therefore helpful to have some means of identifying the undesirable phases.

Accurate quantitative compositional information can be obtained using electron microprobe techniques, and this is a preferred method for identification of unknown intermetallic phases. For an intermetallic system in which the composition of the phases is known, however, simpler identification techniques can be used. A technique particularly suitable for Nb based systems involves formation of a thin anodic oxide film over the sample surface. Given suitable control of the anodization process, these films will form distinct interference colors for each intermetallic phase. Since anodization is routinely performed during the pre-test preparation of Nb and Nb_3Sn cavities, this is a very convenient technique for r.f. applications.

A variety of anodization techniques have been reported for the Nb-Sn system.[1-4] These techniques vary considerably

from author to author, and in some cases contradictions between the various authors exist. In an attempt to clarify the situation, a brief discussion is presented here of the mechanism of anodic film formation. Results obtained by application of the techniques of references 1-4 to a common set of Nb-Sn strip-samples are then discussed, along with the requirements which are apparently necessary to achieve reproducible interference colors for the various phases. Finally, a description is given of the technique used to measure the oxipolishing thickness-voltage relationship for Nb_3Sn.

I. Formation of Anodic Oxide Films

When a metal is made the anode of an electrolytic cell, anodic oxidation is one of several reactions which may occur, in competition with other reactions such as anodic dissolution and oxygen evolution. If the metal in question is Tantalum or Niobium, anodic oxidation occurs, to the exclusion of other reactions, in almost any electrolyte except hydrofluoric acid, which attacks the oxide film itself. In addition, the oxide forms a tenacious, impermeable film which protects the underlying metal from further reaction. Other valve metals, such as Zr, W, Al and Ti, also show this behavior, but with a more limited range of electrolytes than is the case for Ta and Nb.

Anodic Oxide Growth Kinetics

Since the anodic film prevents direct interaction between the electrolyte and the anode, the oxide growth rate is limited by the rate at which ions move through the growing oxide layer (we assume here that the oxide is not attacked by the electrolyte). At the electric field strengths typically reached during anodization (3-5 MV/cm for Nb and Ta) the primary conduction mechanism is not due to ohmic conduction by free electrons, but results instead from repeated tunneling of ions through the potential barriers separating the equilibrium positions of these ions in the oxide.[5] The transport kinetics are similar to those of solid state diffusion, and the ionic current shows temperature and field dependence of the form[5]:

$$I = I_o \exp\left(\frac{qaE - W}{kT}\right) \qquad (1)$$

where E = applied field

q = effective ionic charge

a = equilibrium ionic spacing

W = height of inter-ion potential barrier

The applied field E is equal to the applied voltage V divided by the oxide thickness d, with small corrections for the metal-oxide and oxide-electrolyte interface potentials.

Voltage-Thickness Relations

The anodization schemes reported in references 1-4 fall

into two categories: anodization at constant voltage, and anodization at constant current to a specified terminating voltage. Both techniques yield a voltage-thickness relation as a result of the exponential current-voltage relation (1).

Anodization at Constant Voltage: An initially unanodized sample placed in an electrolyte at a fixed voltage V_o will initially pass a very large current, since the thinness of the oxide layer during this initial results in a very high field within the oxide. As the film thickness increases, the current falls rapidly until, at a thickness

$$d_o \gtrsim V_o qa/W$$

growth may be said, for practical purposes, to have stopped, and the film thickness is characterized by the applied voltage V_o. Most of the published anodization techniques for Nb-Sn are of this type. Two points should be noted:

1) Since the field and current density change throughout the growth of the film, the properties of the oxide may be expected to vary with depth. In particular, the layer of oxide formed during the initial high current period may be quite different from the rest of the film, and the characteristics and thickness of this layer may depend upon the quality of the electrical connection made to the substrate. Repeatable high-current connections to valve-metal substrates are often difficult to make.

2) Even if film growth kinetics are uniform from sample,

thethickness is not fully specified unless some cutoff time or cutoff current is specified.

Anodization at Constant Current

If an initially unanodized sample is anodized at a constant current, the field within the oxide remains constant throughout the growth of the resulting film, as may be seen from the current-field relation Eq. (1). The film thickness, and the applied voltage necessary to maintain the constant current level, increase linearly with time. Since the field and growth rate are constant, the structure of the oxide is more uniform throughout the film thickness than is the case with films formed at constant voltage, and the relationship between thickness and terminating voltage is more reproducible than the constant-voltage relationship. For a given sample, in fact, specification of the electrolyte, current density, terminating voltage and temperature completely characterizes the anodic film.[5]

Formation of Interference Colors

The colors formed by anodic oxide films result in most cases from constructive interference between light reflected at the oxide-air interface and light transmitted through the oxide-air interface and undergoing multiple reflections within the oxide. The color of the film therefore depends upon the thickness of the film, the refractive index of the oxide, and

the phase shifts which occur upon the reflections at the interfaces. For normally incident light of wavelength λ, reflection minima occur at oxide thicknesses d given by[5]

$$d + X = (2r+1)\lambda/4n \qquad (2)$$

where n = oxide refractive index

r = 1,2,3 ... (order of interference minimum)

X = length equivalent to interface reflection phase shifts

Variations in color between different phases can therefore result from variations in n, X or d, while the thickness d depends upon the oxide properties (effective ionic charge, ionic spacing and barrier height) through the current-voltage relation (Eq. 1). It should be noted that, because of the reflection phase shifts, which are independent of oxide thickness, the characteristic reflected wavelength does not vary linearly with film thickness, i.e. second order interference colors do not occur at twice the oxide thickness at which first order colors occur.

In some cases the color of an oxide film does not result from interference, but stems from intrinsic coloration of the oxide itself. In these cases the color does not vary with thickness, except perhaps for very thin films, but the color can still be used in some cases to identify the underlying phase.

II. Investigation of Published Anodization Techniques

Four previously published anodization techniques were investigated during the course of this work. All were developed specifically for Nb-Sn samples, and most are based on the earlier work of Picklesimer[6], who applied the technique to zirconium alloys. The salient features of these techniques are listed in Table C-I.

Table C-I. Reported Anodization Techniques

Author	Type	Electrolyte	Temp.	Voltage	Comments
Pfister[1]	Const. current	50% NH_4OH	Room	75V	10 mA/cm^2
Enstrom[2]	Const. current	Alcohol, glycerine, organic acids	Room	27V	6 min limit
Wyman[3]	Const. current	same	Room	33.5V	Voltage adj. to std. Nb color
Macphail[4]	Const. current	10% citric acid	5°C	22.5V	Low impedance voltage source necess.

The colors reported by the authors for the various phases are shown in Table C-II. In the case of the Wyman and Enstrom techniques the formulas claimed by the authors for some phases do not match currently accepted formulas; reported formulas are indicated in these cases.

Table C-II. Reported Colors for Nb-Sn Phases

Author	Nb	Nb_3Sn	Nb_6Sn_5	$NbSn_2$	Sn
Pfister	Blue	Pink	---	---	---
Enstrom	Blue	Violet	Red ("Nb_3Sn_2")	Brown ("Nb_2Sn_3")	Yellow
Wyman	Light blue	Darker blue (Nb_3Sn & Nb_4Sn)	Purple aster ("Nb_2Sn")	Burnt sienna ("Nb_2Sn_3)	Yellow
Macphail	Dark blue	Mauve	Brown	Fawn	Pink-white

Note: Since different voltages are used by the various authors, color differences are expected for the four phases containing Nb (see text).

All four techniques were applied to ionplated and vapor-diffused samples over a period of several months, and the following observations were made:

1) With the Macphail technique, the reported Nb and Nb_3Sn colors could not be reliably obtained unless a very low impedance sample connection and power supply were used, as recommended by Macphail.
2) The Nb, Nb_3Sn and Nb_6Sn_5 colors reported for the Wyman and Enstrom techniques could be obtained without difficulty.
3) All three constant-voltage techniques showed variations from the colors reported for the $NbSn_2$ and Sn phases. In particular, the Wyman and Macphail techniques showed distinct brown and green colors, in addition to the colors

reported. The green color was observed at the edges of yellow-colored regions, while the brown color was observed either in conjunction with the orange regions, or in separate patches which were usually larger than the yellow regions.

4) The pink-white color reported by Macphail for Sn inclusions was not observed. Inclusions in samples anodized using the Macphail technique showed the same yellow color reported by Wyman and Enstrom for Sn inclusions.
5) The Pfister technique, which was the only constant-current technique, gave very consistent results for the Nb and Nb_3Sn phases. Small inclusions, thought to be Sn, had the same yellow color observed with the Enstrom and Macphail techniques. In some cases, flat, semi-transparent yellow patches were also observed, similar in shape to the brown patches observed with the Enstrom and Wyman techniques. No colors other than blue, pink and yellow were observed.

An additional experiment was then performed: a set of samples was anodized in each of the four electrolytes, at the temperatures recommended by the authors, using a constant current of 10 mA/cm^2, and stopping at each of the recommended terminating voltages. It was found that, under these conditions, all the electrolytes produced the same colors for the

Nb, Nb_3Sn and Sn phases, when anodized to the same terminating voltage. Since the samples used contained very small amounts of Nb_6Sn_5 and $NbSn_2$, no conclusions could be reached concerning the colors for these phases.

Discussion

Coloring of Anodized Sn:

The most troubling discrepancy observed with the reported anodization techniques is the disagreement over the correct color for Sn, with Macphail reporting a pink-white color, while the results reported for the Enstrom and Wyman techniques, and the work done here with all four techniques, indicate a lemon-yellow color. In additon, the observation here of distinct sienna and brown colors with the Wyman and Enstrom techniques, and of a green color in addition to the yellow color, does not agree with the previously reported results.

It appears that these discrepancies can be attributed to the presence of pure, or nearly pure, Sn in the samples involved. According to Young[6], pure Sn upon anodization can form two distinct types of oxide: a blue-gray or brown stannite film, and a yellow or yellow-green stannate film. For a given electrolyte and temperature, a critical anodizing current exists, below which the brown stannite film forms, and above which the yellow stannate film forms.

Neither film color appears to result from interference effects, thus film color is independent of terminating voltage, except perhaps for very thin films.

Assuming that the possible presence of some dissolved Nb does not substantially alter the anodizing properties of Sn, we can conlcude that the brown and fawn colors reported by Macphail were probably Sn or Sn-rich solid solutions, anodized at current densities below the critical current density for the electrolyte used by Macphail.

It is not clear what the pink-white color reported by Macphail was, although it could have been SnO_2, which is reported to be white.[6]

Similarly, the brown color observed with the Wyman and Enstrom techniques was probably the stannite film.

It is interesting to note that both brown and yellow colors were observed with the Wyman and Enstrom techniques for what were both apparently Sn inclusions.

The alcohol-glycerine based electrolyte used by these authors was also observed to be much less sensitive to variations in source impedance than the aqueous citric acid solution used by Macphail. Both phenomena might result from a current-limiting action of the alcohol-glycerine electrolyte.

Because this electrolyte is only weakly ionized and is also rather viscous, the peak current densities reached during constant-voltage anodization are not especially high,

thus minimizing the effects of source impedance variations.

The same combination of low conductivity and short diffusion length could also explain the fact that small, pointlike Sn inclusions had the yellow stannate film, while slightly larger Sn regions had a brown color. It is known from electroplating experience[7] that the electrochemical reactions in processes like electroplating and anodizing result in the formation of anodic and cathodic "polarizations", or thin regions of chemical interaction between electrode and electrolyte, in which the electrolyte composition differs substantially from that of the rest of the bath. As the reaction proceeds, new reagents diffuse into the polarization region to replenish those consumed in the reaction. As current densities increase, the reaction rate can become limited by the rate at which this replenishment occurs.

Tin anodized in a sufficiently viscous electrolyte should thus form a brown stannite film. Very small Sn regions might, however, still achieve high enough current densities to form the yellow stannate film, provided these regions are less than a few electrolyte diffusion lengths in extent and are therefore never very far away from fresh electrolyte.

A non-viscous, highly ionized electrolyte such as that used by Pfister would not undergo anodic depletion of the sort

just described, and in fact no brown regions were observed with the Pfister technique.

Nb_6Sn_5 and $NbSn_2$ Colors:

Good agreement on Nb_6Sn_5 colors was obtained between the results reported by Wyman and Enstrom and the work done here. Although no quantitative compositional analysis was done here, regions of several test cavities which were nearest the Sn vapor source and thus likely to have a high Sn concentration showed the red Nb_6Sn_5 color when anodized using the Enstrom technique.

Similarly, the sienna color reported for Wyman for $NbSn_2$ agrees with the work done here, but some difficulty still exists in distinguishing the brown stannite film from the sienna film. It may be the case that $NbSn_2$ can form both types of film, in a manner similar to that of Sn. More work would be required to clarify this possibility.

As mentioned earlier, no colors other than those reported for Nb, Nb_3Sn and Sn were observed with the Pfister technique. Since most of the samples anodized with this technique were cavity-grade material and probably had little, if any, Nb_6Sn_5 or $NbSn_2$ present, no definite conclusion can be reached concerning the correct colors for these phases with this technique. The 75V terminating voltage was apparently chosen to optimize the visual contrast between the Nb and Nb_3Sn phases, at the expense of the other phases. Use of Wyman's 33.5V

terminating voltage should permit identification of Nb_6Sn_5 and $NbSn_2$, but the visual distinction between Nb and Nb_3Sn is much more subtle at this voltage.

Although the possibility exists that the two Sn-rich phases cannot be identified with the Pfister electrolyte, this possibility seems very unlikely, since the terminal phases Nb and Sn both anodize satisfactorily.

III. Recommended Technique for Microwave Applications

For microwave applications, the Pfister anodization technique has an overwhelming advantage, since it is part of the oxipolishing process which has been extensively used for pre-test cavity preparation, and it is known to produce good r.f. properties. The glycerine and organic acids contained in the Wyman and Enstrom electrolytes, on the other hand, might prove difficult to remove completely, and any residual electrolyte present during testing would probably degrade r.f. performance considerably.

The only possible objection to the Pfister technique arises if it proves impossible to identify the Nb_6Sn_5 and $NbSn_2$ phases with this technique. In this event, the Wyman technique could be used with test samples during process development to detect these two phases, and the Pfister technique could then be used for actual cavities.

Details of the anodization technique used in this work and recommended for future work follow. This technique differs slightly from that of Pfister by the inclusion of a short constant-voltage anodization period following the constant-current anodization. This constant-voltage period is included to minimize variations in color across the cavity surface resulting from variations in anode-cathode separation.

Description of Technique:

1) Contact is made to the cavity half to be anodized with a .010" Nb wire, inserted through one of the holes in the cavity perimeter and twisted tightly.
2) The cavity is then placed in an open-topped teflon container.
3) A 1/16" sheet Nb cathode, with shape and area approximately equal to those of the cavity half, is placed directly over the cavity half, with approximately 1" of space between the cathode and the top of the cavity half.
4) Freshly mixed 50% NH_4OH is poured into the container to a height of about 1" above the cathode.
5) An adjustable current-limiting power supply is set to a voltage of 75V, and the current limit is set to 10 mA per cm^2 of cavity area. This area includes only the top surface of the cavity half.
6) The preset current is applied to the cavity until the

supply voltage reaches 75V, then left at this voltage until the current falls to 2 mA/cm^2. The current is then turned off, and the cavity half is immediately removed from the electrolyte, rinsed in distilled water and methanol, and dried.

This technique is also recommended for use with the Wyman and Enstrom voltages, with terminating voltages of 33.5V and 27V, respectively.

Determination of Oxipolishing Thickness-Voltage Relation

The "Pfister" anodization technique has been used for several years as part of the "oxipolishing" technique developed by Siemens AG for preparation of Nb cavities.[8] The oxipolishing technique consists of alternately anodizing the surface and stripping the oxide in HF. In this manner, thin layers of material may be removed, leaving a clean, smooth and stress-free surface.

With Nb_3Sn layers it is very useful to know how much material is removed during each oxipolishing cycle, so that the properties of the layer may be correlated with depth. For Nb, the thickness-voltage relationship of 8 Å/V had been established.[9] Since the corresponding relationship for Nb_3Sn was unknown, the procedure outlined below was used to determine this relationship.

A flat, vapor-diffused Nb_3Sn strip-sample was polished

using abrasive grit, and a fine line pattern was masked onto the sample surface with photoresist. The sample was then anodized to a terminating voltage of 75V, the resist was removed, and the oxide was stripped in 48% HF. Because the 50% NH_4OH electrolyte normally used for anodization attacked the photo resits, a 3% H_2SO_4 electrolyte was substituted.

The step formed by selective anodization and oxide removal was then measured with a Numarski interferometer, and was found to be 2070Å±200Å high. This gives a voltage-thickness relationship of 27.6 Å/V ± 2 Å/V, in good agreement with the indirect measurements of Arnolds et al.[10]

It should be noted that this procedure measures the thickness of the metal removed by one 75V oxipolishing cycle, rather than the thickness of the anodic film at the 75V terminating voltage.

References for Appendix C

1. Hillenbrand, B., Martens, H., Pfister, H., Schnitzke, K., and Uzel, Y., "Superconducting Nb_3Sn Cavities with High Microwave Qualities", 1976 Applied Superconductivity Conference, Stanford Univ., August 1976.

2. Enstrom, R., Courtney, T., Pearsall, G., and Wulff, J., "Current and Field Dependence of Superconductivity on Microstructure in the Niobium-Tin System", Metallurgy of Advanced Electronic Materials, G. E. Brock, ed. (Wiley, New York, 1963).

3. Wyman, L. I., Cuthill, J. R., Moore, G. A., Park, J. J., and Yakowitz, H., "Intermediate Phases in Superconducting Niobium-Tin Alloys", J. Res. of the NBS--A. Physics and Chemistry 66A, No. 4 (July-August 1962).

4. Macphail, I., "A Metallographic Technique for Niobium-Tin Alloys", U.K. Atomic Energy Authority Research Group Report AERE-R5421, Harwell, Berkshire, 1967.

5. Picklesimer, M. L., "Anodizing as a Metallographic Technique for Zirconium Base Alloys", ORNL-2296, Metallurgy and Ceramics TID-4500 (13th Ed.), Oak Ridge National Laboratory.

6. Young, L., Anodic Oxide Films (Academic Press, New York, 1961).

7. Blum, W., and Hogaboom, G. B., Principles of Electroplating and Electroforming (McGraw-Hill, New York, 1949).

8. Martens, H., Diepers, H., and Sun, R. K., "Improvement of Superconducting Cavities by Anodic Oxide Films", Phys. Lett. 34A, 439-440 (1971).

9. Halbritter, J., personal communication, August 1976.

10. Arnolds, G., and Halbritter, J., personal communication, August 1976.

Appendix D

TEMPERATURE AND FREQUENCY DEPENDENCE OF SUPERCONDUCTING SURFACE RESISTANCE

Although a complete calculation of the BCS surface resistance is a formidable task, the empirically observed frequency and temperature dependence of the surface resistance can be satisfactorily explained with simpler models. We present here a "plausibility argument" using a modified "two-fluid" model.

We assume photon energies well below the band gap energy, and temperatures and field strengths sufficiently low that the shielding currents are dominated by supercurrents. Under these conditions, the electromagnetic field distribution inside the superconductor is determined only by the superconducting electrons, and the losses resulting from this field distribution are determined only by the normal-state electrons (superconducting electrons carry no entropy and hence dissipate no heat).

The field distribution inside the superconductor is obtained from the London equations, and we have

$$H_{int} = H_o \exp(-z/\lambda_L) \qquad (1)$$

where H_o = surface magnetic field strength

λ_L = London penetration depth.

The corresponding electric field is obtained from Maxwell's equations:

$$E_{int}(z) = \omega u_o \lambda_L H_{int}(z) \tag{2}$$

and the ohmic losses resulting from the response of the normal-conducting electrons to this field are

$$P = 1/2\ n_N \sigma \int_0^\infty E_{int}^2(z)dz = 1/2\ n_N \sigma \omega^2 u_o^2 \lambda_L^3 H_o^2 \tag{3}$$

where σ is the normal state conductivity

ω is the radian frequency

n_N is the volume density of normal-conducting electrons.

We can obtain an expression for the density of normal-conducting electrons by integrating over all energies above the energy gap:

$$n_N = \int_\Delta^\infty D(E)P(E)dE \tag{4}$$

where $D(E)$ is the density of states

$P(E)$ is the probability of occupancy

E is the electron energy measured from the Fermi energy.

Inserting the Fermi-Dirac distribution function:

$$P(E) = (\exp(E/kT) - 1)^{-1} \tag{5}$$

and the BCS density of states:

$$D(E) = N_o\ E/(E^2 + \Delta^2)^{-1/2}$$

where N_o is the density of states in the absence of the BCS interaction, we get

$$n_N = N_o \int_\Delta^\infty \frac{|E|}{\sqrt{E^2 + \Delta^2}} \frac{1}{e^{E/kT} + 1}\, dE \tag{6}$$

Since we integrate only over values $E > \Delta$, and since $\Delta \sim 1.75\ kT$, $E/kT \geq 7$ for $T \leq T_c/4$, $\frac{1}{e^{E/kT}+1} \sim e^{-E/kT}$ and

$$n_N = N_o \int_{\Delta}^{\infty} \frac{E}{\sqrt{E^2+\Delta^2}} e^{-E/kT} dE \qquad (7)$$

Since the exponential damps the integrand at large energies, but is relatively constant near the singularity in the density of states at $E = \Delta$, we restrict the upper limit of integration to $E \simeq 2\Delta$ and assume the constant value $\exp(-\Delta/kT)$ for the distribution function, and

$$n_N = N_o e^{-\Delta/kT} \int_{\Delta}^{\Delta} \frac{E}{\sqrt{E^2+\Delta^2}} dE$$

$$= 5^{1/2}\ N_o \Delta e^{-\Delta/kT}\ H_o^2 \qquad (8)$$

Using this expression for n_N in (3), we get

$$P \propto N_o \sigma \omega^2 \lambda_L^3\ ^2 e^{-\Delta/kT}\ H_o^2 \qquad (9)$$

and a surface resistance

$$R_s \propto N_o \sigma \omega^2 \lambda_L^3 e^{-\Delta/kT}$$

We therefore predict an ω^2 frequency dependence, which agrees with experiment, and an $\exp(-\Delta/kT)$ temperature dependence, which agrees favorably with the $1/T\ \exp(-\Delta/kT)$ dependence observed experimentally. More complete derivations can be found in references 1 and 2.

References for Appendix D

1. J. Halbritter, Z. Physik 266, 209-217 (1974).

2. S. B. Nam, Phys. Rev. 156, 470-487 (1967).